Project:	**nanoCOPS** **nanoelectronic COupled Problems Solutions**
Project Number:	**FP7-ICT-2013-11/619166**
Work Package:	**WP2 Uncertainty Quantification**
Deliverable:	**D2.8 – Final Report (a) on Uncertainty Quantification**
Scheduled:	**M33 (July 2016)**

Title:	**Public Report (b) on Uncertainty Quantification** **The report is based on Version 2 of the Final Report (a)**
Authors:	**Roland Pulch, Piotr Putek, Jan ter Maten,** **David Duque, Sebastian Schöps,** **Ulrich Römer, Thorben Casper,** **Yao Yue, Lihong Feng, Peter Benner,** **Wim Schoenmaker**
Affiliations:	**UGW, BUW, TUD, MPG, MAG**
Contact:	`Roland.Pulch@uni-greifswald.de`
Date:	**September 7, 2016 (M35)**

D2.8 Public Report (b) on Uncertainty Quantification

Roland Pulch (UGW)

Piotr Putek, Jan ter Maten (BUW)

David Duque, Sebastian Schöps, Ulrich Römer, Thorben Casper (TUD)

Yao Yue, Lihong Feng, Peter Benner (MPG)

Wim Schoenmaker (MAG)

September 7, 2016

Contents

1 Introduction

In the nanoCOPS project, there are three scientific work packages: WP1 on time-domain simulation of coupled problems, WP2 on uncertainty quantification and WP3 on validation, demonstration and measurements. This final report summarizes the achievements within the second work package on uncertainty quantification (UQ). The scientific word is organized within seven tasks. In WP2, the deliverables [1, 2, 3, 4, 5, 6, 7] and the milestones [8, 9, 10] provided intermediate results about the development. Moreover, deliverable D2.7 [7] also represents a final reporting on the implementations of algorithms for the tasks in WP2. The validation is still ongoing. Overviews of the progress within the whole project are published in [40, 41, 46, 47], where parts were dedicated to UQ.

In the previous years, more attention has been devoted to the field of UQ in scientific computing and engineering. In procedures of an industrial production, undesired variations typically appear due to imperfections. Thus a mathematical model and an associated numerical simulation shall quantify the variations to confirm or disprove the reliability of produced devices. Now the aim of WP2 is to employ the concepts of UQ to problems in nanoelectronics and applications relevant for electronics industry in Europe.

In nanoelectronics, multiphysics problems occur, where different effects like electromagnetics, heat transport, mechanical stress and complex semiconductor behavior, for example, are coupled. Here the multiphysics problems include differential algebraic equations and partial differential equations. Often the numerical simulation of the coupled system consists of a transient analysis, where either a monolithic integration or a dynamic iteration is used in the time domain. In WP2, uncertainties are considers by the introduction of random variables into the multiphysics problems, which represents the most common approach in UQ, see [84]. Consequently, stochastic models have to be solved. Both intrusive and non-intrusive methods exist for a numerical simulation. However, the complexity of the coupled problems often requires to adapt the general numerical approaches to the specific structure of the nanoelectronic applications. Figure 1 sketches our concepts for the numerical simulations in UQ.

The work package on UQ tackles several challenges in the general field of scientific computing as well as the particular field of nanoelectronics. The multiphysics nature of the nanoelectronic problems yields coupled systems, where the different type of the subsystems causes multiscale and multirate effects. The achievement of an efficient numerical simulation represents a sophisticated task already in the case of deterministic parameters. Now WP2 even considers the multiphysics problems including random variables and random processes. Furthermore, WP2 investigates the determination of small failure probabilities to confirm the reliability of an industrial production in the case of tiny defect ratios. Since the variations of a manufacturing procedure may not obey traditional random distributions, the fitting of probability distributions functions or, equivalently, probability density function is performed with respect to measurement data from the industrial partners.

The following seven sections are dedicated to the tasks T2.1-T2.7 of Work Package 2.

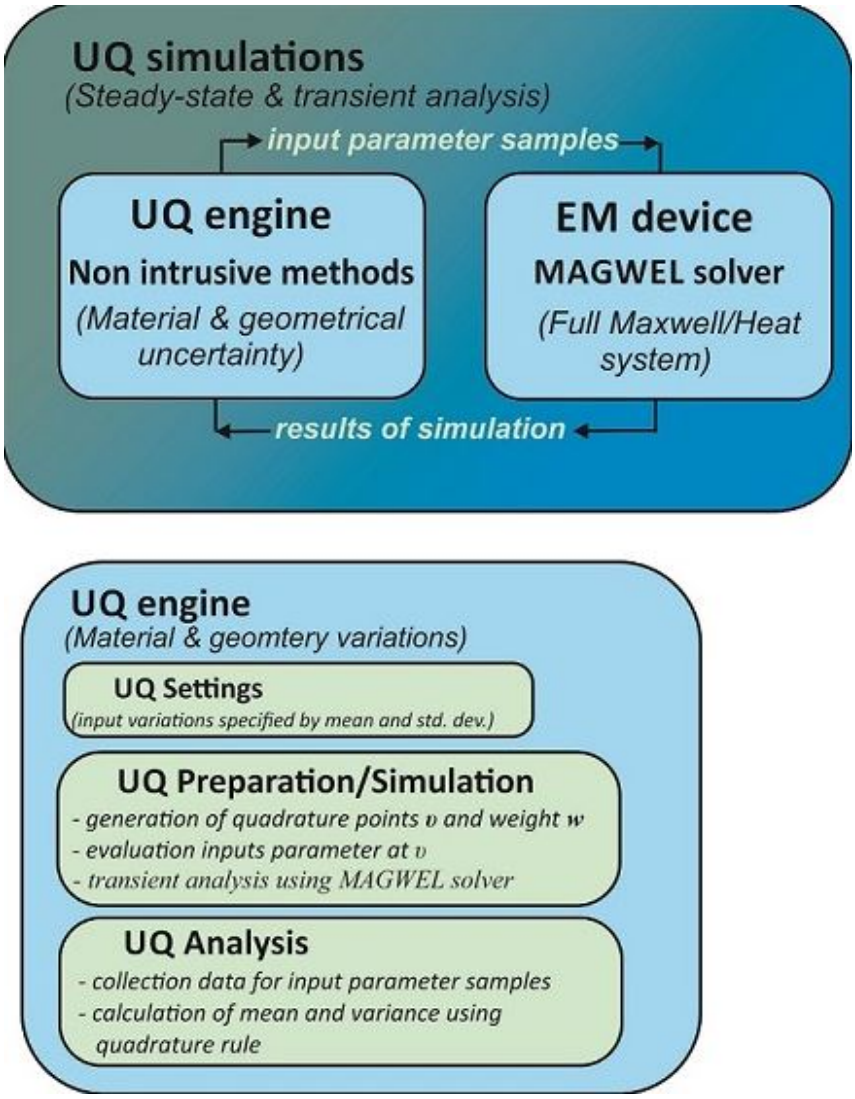

Figure 1: Concepts for numerical simulation in Uncertainty Quantification [4].

2 Quantification of uncertainties in device materials, geometry and boundary conditions

In this section, we consider the stochastic modeling for materials, geometry and boundary conditions in spatial domains. The results are used in multiphysics problems for the parts consisting of partial differential equations. This topic corresponds to Task T2.1.

2.1 Connection to test cases and deliverables

Link to test cases :

- Test case 1/2a A realistic size power MOS at constant temperature / in ET coupling mode
- Test case 2b A driver chip with multiple heat-sources
- Test case 4a An 8-shaped inductor
- Test case 4b ACCO inductor
- Test case 5 A fast and reliable model for bondwire heating
- Test case 7 Reliable RFIC Isolation
- Test case 12 Transformer (academic benchmark for weakly and strongly coupled field/circuit problems)

Link to WP2 deliverables :

- D2.1 Intermediate Report on Models and algorithms for quantification of uncertainties in materials, geometry and boundaries of devices
- D2.7 Algorithms implemented in software packages for all Tasks 2.1-2.6.

2.2 Reasons for uncertainty quantification in electronic devices

Due to the ongoing miniaturization and imperfections in manufacturing processes, the production of electronics system is affected by undesired variations of material, geometrical and environmental parameters like a temperature at the devices boundaries, for example. On one hand, at this stage of work, a special attention was given on material uncertainties in the nonlinear material constitutive law, e.g., reluctivity of core made of soft iron in electronic transformer, which belong to the most influential source of uncertainties in several applications [4, 60]. We investigated this problem by using Karhunen-Loève and a spline representation of the constitutive law. On the other hand, since in many applications, the physical domain cannot be determined precisely, uncertainties in the geometry such as an interface between two different materials or boundaries of the computational domain have been taken into account in simulations. To deal with this problem either topologically preserved method such as a mapping of random domain to the fixed domain or the topological method such the level set

or topological gradient method can be applied. In our case, due to some technical software restrictions and mainly the MAGWEL preferences, the random representation by the topological methods was beneficial and easier in the implementation [62, 63]. Additionally, the variablity of the bonding wire due to construction tolerances based on the stochastic electrothermal field-circuit model has been analyzed in [25], shown on Figure 3. Thus, this kind of input variations have been considered in order to develop reliable and robust tools for the prediction and simulations of electronic devices. For instant, a model of a power MOS transistor under consideration has been depicted on Figure 3.

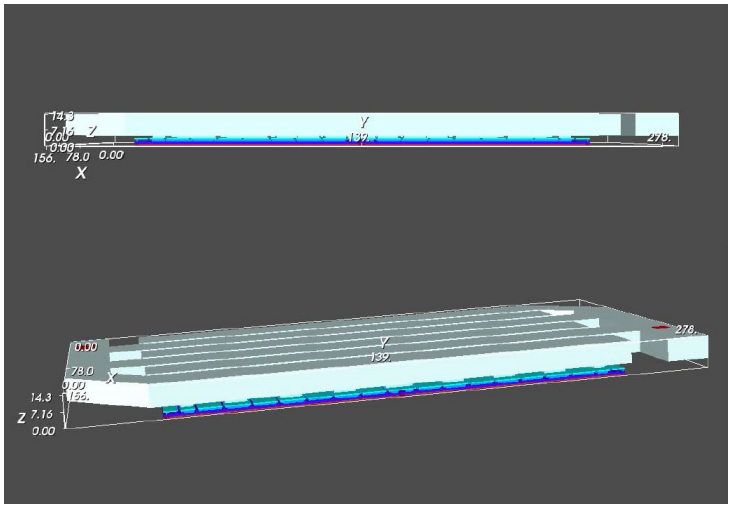

Figure 2: Cross-sections of a power MOS transistor model treated as a test case 1/2a [45, 62].

2.3 Distinction between Uncertainties in Material and Geometry

From the numerous types of possible model input parameters, we focus on uncertainties in the material properties and the geometry. In general, in a stochastic setting, uncertain inputs are modeled by means of (infinite-dimensional) random fields and hence, for computer simulations the task of discretization needs to be accomplished. Several techniques have been proposed to this end. We refer to the Karhunen-Loève expansion, the generalized Polynomial Chaos technique as well as model specific grid based or analytic representations. Moreover, as the dimensionality of the discrete representation is directly related to the computational cost, efficient low-rank representations are highly desirable and efforts should be devoted to their construction. In this context controlling the respective (modeling) error in the stochastic solution is of importance.

2.3.1 Materials

Here, the uncertainty can be found in the (nonlinear) material constitutive law. It has been observed that in several applications this is the most influential source of uncertainty [64]. The stochastic modeling is complicated by the fact that the material relations and hence the random fields are subject to shape constraints. In particular positivity, monotonicity and smoothness of nonlinear material curves need to be preserved. It

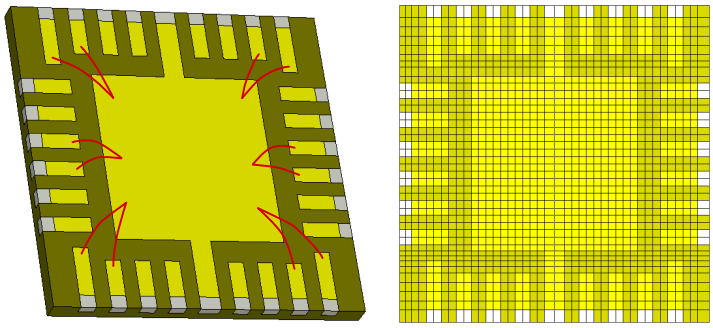

(a) Inclined top view (b) Hexahedral mesh

Figure 3: Model of investigated chip (figure from [25]).

has been investigated how this can be achieved by means of the Karhunen-Loève expansion and flexible spline representations of the constitutive laws [67]. In particular relations for the input discretization errors and for accomplishing the shape constraints have been derived.

2.3.2 Geometry

Uncertainties in the geometry may refer to both an interface of two different materials and the boundary of the computational domain. A major difficulty arises as the equations are formulated on different domains due to the uncertainty. Also shape perturbations have to be modeled appropriately and re-meshing efforts should be kept minimal. Here, spline representations are used to model shape deformations. Moreover, in the context of sensitivity analysis we employ the velocity method [30], a well established technique from shape optimization. A transformation $\mathcal{T}_s = x_s$ can be defined by means of the differential equation

$$\frac{\mathrm{d}}{\mathrm{d}s} x_s = \mathcal{V}, s \geq 0, \tag{1}$$

endowed with suitable initial conditions, where V is referred to as velocity field, see also Figure 4. The application of Non-Uniform Rational B-Splines (NURBS) to model uncertainties of the geometry was successfully implemented in [29] for Maxwell's Eigenvalue problem, uncertain bond wire length have been investigated in [25] and uncertain geometry in the context of robust optimization in [22, 60, 61, 63]. In [63] also the more complicated case of uncertain topology was considered.

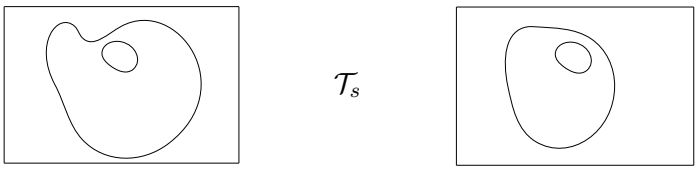

Figure 4: Velocity Method: family of transformed interfaces/domains by means of $\mathcal{T}_s$ [7].

Once a finite representation of the stochastic inputs is at hand, uncertainties need to be propagated efficiently through the model. To this end various deterministic techniques, such as spectral methods [35, 84] and moment based perturbations methods [72], have

been found to be superior to classical Monte Carlo sampling in several circumstances. This is true in particular for low-rank input representations and an analytical input-output dependence of the model. They will be discussed in the following sections.

2.4 Non-intrusive methods for uncertainty quantification

Non-intrusive methods belong to the sampling techniques, which require repetitive run of the deterministic solver in order to perform the uncertainty quantification. In each method, however, one of the aims is to compute an approximation of the statistical moments like the mean and the standard deviation, for example, or, alternatively, to find a finite set of coefficient functions, when a polynomial chaos expansion has been used [84].

2.4.1 Monte Carlo method

The Monte Carlo (MC) simulation, see [38], belongs still to the most popular methods for uncertainty quantification. As a consequence of the Strong Law of Large Numbers, the concept of this method constitutes in the repeated random sampling in order to provide numerical results. Given realizations $(\xi_1, \ldots, \xi_K)$ of a sample $(p_1, \ldots, p_K)$ of the random variable p, the mean value is estimated by

$$m_K := \frac{1}{K} \sum_{k=1}^{K} f(\xi_k). \tag{2}$$

Based on the Strong Law of Large Numbers, it holds that $m_K \to \mathbb{E}(f(p))$ for $K \to \infty$. Therefore the expectation value is approximated by the sample mean (2), i.e., $m_K \approx \mathbb{E}(f(p))$ for sufficiently large K. Consequently, the MC or quasi MC techniques, see [50], can be treated as a special case of sampling methods with weights defined as $\omega_k = \frac{1}{K}$ for all k. On the one hand, the convergence rate of the MC method is proportional to $1/\sqrt{K}$ with K denoting the number of sampling points, which might be considered as a drawback. On the other hand, this convergence rate is independent of a number of analyzed variables. In our work, it has been implemented only for the verification purposes.

2.4.2 Quadrature-based stochastic collocation

The quadrature-based stochastic collocation method (SCM), see [21, 53, 84], belongs also to the sampling methods but it is much more robust than the MC-based technique. It also relies on repetitive run of the deterministic model, however, for the integral approximation of the expectation, the appropriate quadrature rules have been applied

$$\mathbb{E}\left[f(p)\right] = \int_{\Pi} f(p)\rho(p)\, \mathrm{d}p \approx \sum_{k=1}^{K} w_k f(\xi_k) =: \hat{\mathbb{E}}\left[f(p)\right]. \tag{3}$$

Here the quadrature grid points $\{\xi_k\}_{k=1}^K$ and the weights $\{w_k\}_{k=1}^K$ are related to the assumed probability density function ρ. Likewise, the higher moments such as the

variance can be approximated by

$$\mathrm{Var}\left(f(p)\right) \approx \sum_{k=1}^{K} w_k \left(f(\xi_k)\right)^2 - \left(\hat{\mathbb{E}}\left[f(p)\right]\right)^2. \tag{4}$$

However, the effectiveness of this method is strongly affected by the choice of the quadrature grid points. For instance, the Stroud rules yield a relatively small number of grid points for a quadrature of a fixed order.

2.4.3 Pseudo-spectral approach

Another approach, which is closely related to the previous method is the pseudo-spectral technique. Again the basic concept is to provide the solution of the deterministic problem at each quadrature grid point $p^{(k)}$, $k = 0, \ldots, K$. Furthermore, under assumption that each component p_i exhibits a finite second moment, the random field y can be expanded in the truncated polynomial chaos (PC) series, cf. [84],

$$y\left(x, p\right) = \sum_{i=0}^{N} \alpha_i\left(x\right) \Phi_i\left(p\right) \tag{5}$$

with a priori unknown coefficient functions α_i. Here, the basis functions $(\Phi_i)_{i\in\mathbb{N}}$ with $\Phi_i : \Pi \to \mathbb{R}$ are orthonormal polynomials, i.e., $\langle \Phi_i(p), \Phi_j(p) \rangle = \delta_{ij}$ with the Kronecker delta denoted by δ_{ij}. In order to calculate a priori unknown coefficients α_i in (5), the output y is projected into the known polynomial basis $(\Phi_i)_{i\in\mathbb{N}}$ by using a multi-dimensional quadrature rule with corresponding weights w_k

$$\alpha_i(x) := \left\langle y\left(x,\, p\right),\, \Phi_i(p) \right\rangle \approx \sum_{k=0}^{K} w_k\, y\left(x,\, p^{(k)}\right)\; \Phi_i(p^{(k)}). \tag{6}$$

Finally, given the PC coefficient α_i, we can approximate statistical moments as follows

$$\mathbb{E}\left[y\left(x,\, p\right)\right] \doteq \alpha_0(x), \quad \mathrm{Var}\left[y\left(x,\, p\right)\right] \doteq \sum_{i=1}^{N} \left|\alpha_i(x)\right|^2. \tag{7}$$

Summarizing, in the presented sampling methods 2.4.1, 2.4.2 and 2.4.3, the repetitive run of the existing deterministic solver is required in order to find the propagation of uncertainty thorough a model under consideration. However, they differ themselves in the choice of the quadrature grid points and the weights, which has an impact on their efficiency. In our computations, the Stroud-3/5 formula [76] and the so-called sparse grid method [75], which suffer less from the curse of the dimensionality [84], have been used to approximate the statistical moments such the mean and variance values.

2.4.4 Worst-case scenario

Some industrial partners of the nanoCOPS project already used the worst case corner analysis (WCCA) for the quantification of uncertainties. For the WCCA, one has for

each single parameter p three predetermined values (lower value, nominal value, upper value). It follows that 3^q combinations exist n the case of q varying parameters. Thus the computational work is the same as in a tensor product quadrature formula with three points per dimension. By an optimization procedure, one calculates only for those parameter values that lower or minimize some performance function. The result represents a biased look on the parameter space.

In contrast, the quadrature in (generalized) PC is always symmetric. For worst case analyses, we may require biased schemes for the numerical computation of integrals. The technique looks similar to importance sampling, in which now one-point or two-point quadrature (using the points out of the three-point quadrature) are weighted against the three-point quadrature.

2.5 Implementation of the UQ workflow with a black-box model

The flowchart of the implemented the stochastic collocation - based algorithm for the UQ propagation using MAGWEL software as a black-box is shown on Figure 48. It is comprised of two main parts, like the UQ engine[1] and the MAGWEL solver (devEM or ptm-ET). In the Python-C++ interface, the communication between the UQ engine and the MAGWEL solver is established by files. The UQ engine involve three main sub-routines: (a) in the UQ settings the input random parameters are described by the assumed distribution, e.g., Gauss or Uniform type by means of the mean and the standard deviation are specified, (b) at the UQ Preparation/Simulation stage, first the quadrature points and the weights are generated and next the solution of the deterministic problem using the MAGWEL solver is computed at each quadrature grid point, (c) in the post-processing stage, the statistical moments like the mean value and the variance are calculated. Additionally, graphs of the probability density function and the cumulative distribution function of the quantity of interest can be generated. The efficiency of this algorithm can be improved by using a parallel technique, where the task related to deterministic calculation at grid points can be just sent to different cores or processors [36]. The above approach is non-intrusive, i.e., the UQ set up is make as a loop around the MAGWEL solver.

Within the nanoCOPS project a beta version of a graphical user interface (UQ GUI) was designed, implemented and added to MAGWELs software suite. It allows to quantify the impact of any design random parameter, described by assumed distributions on quantities of interest such as, e.g., S-parameters, drain/source currents and voltages, temperature of probe, heat flux, etc. The interface is based on the Dakota library of Sandia National Labs. Figures 5 – 8 give an overview of the GUI interface.

[1] The first experiments did exploit the UQ Toolkit, `http://www.sandia.gov/UQToolkit/`. Currently we consider Dakota, `http://dakota.sandia.gov/`. Both, UQ Toolkit and Dakota, are developed at Sandia National Laboratories.

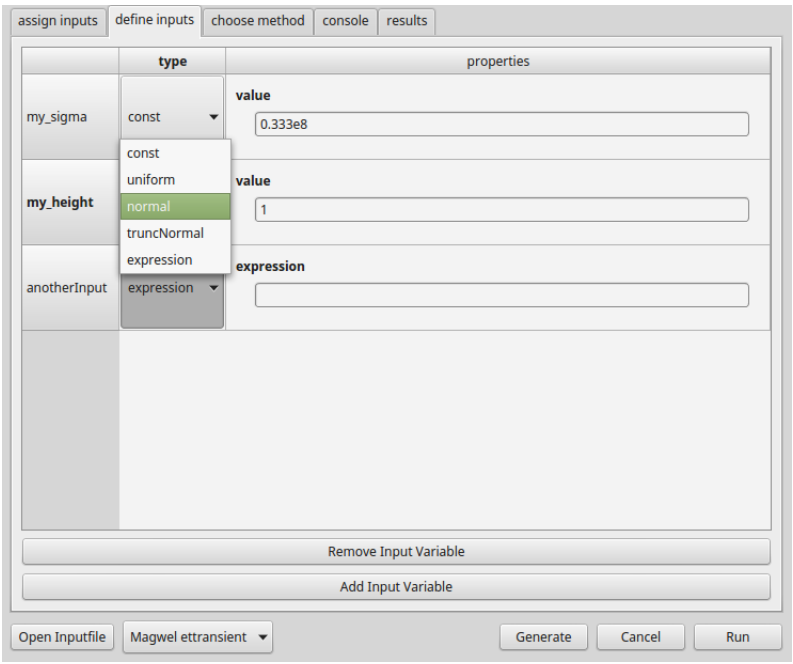

Figure 5: GUI panel for defining the inputs [7].

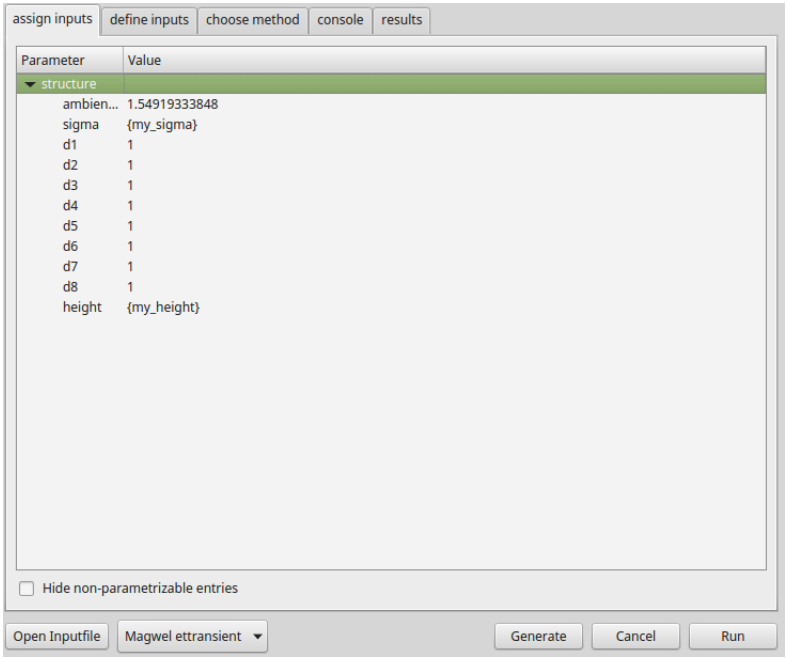

Figure 6: GUI panel for setting the inputs [7].

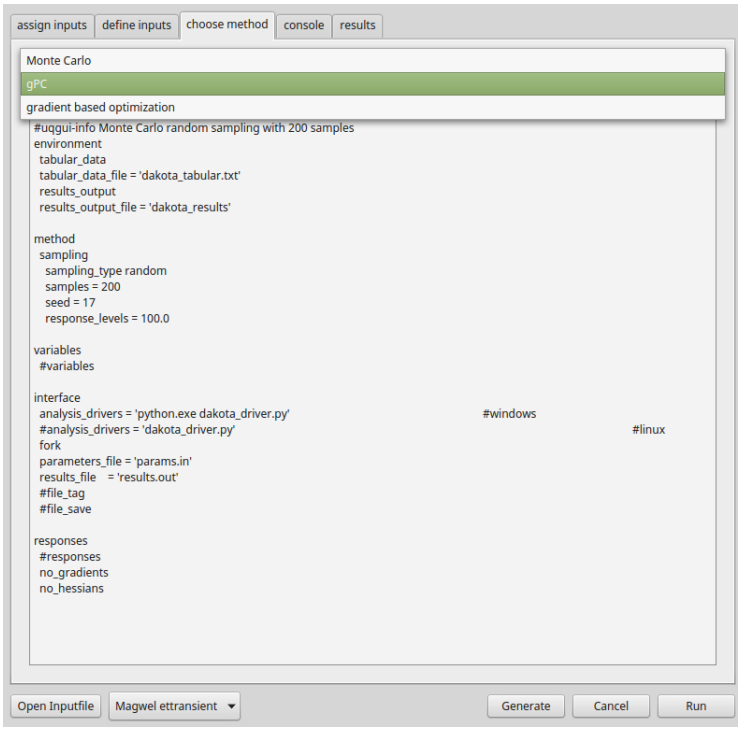

Figure 7: GUI panel for selecting the methods [7].

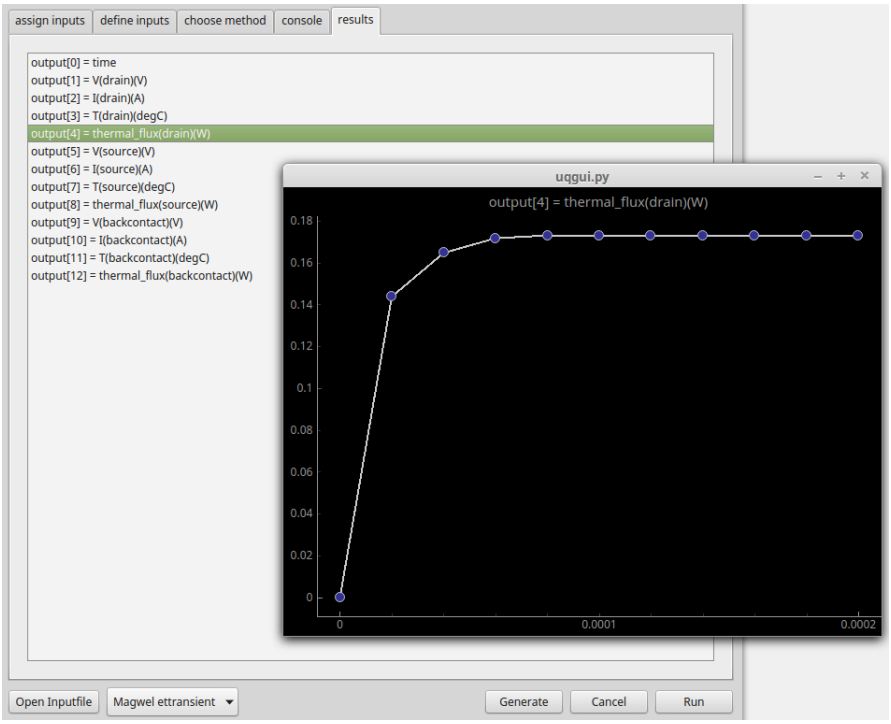

Figure 8: GUI panel showing the results [7].

3 EM-device-circuit co-simulation with random parameters

Now multiphysics problems are investigated, which represent coupled systems with subsystems modeling different effects. This topic corresponds to Task T2.2.

3.1 Connection to test cases and WP2 deliverables

Link to test cases :

- Test case 1/2a A realistic size power MOS at constant temperature / in ET coupling mode
- Test case 2b A driver chip with multiple heat-sources
- Test case 4a An 8-shaped inductor
- Test case 4b ACCO inductor
- Test case 5 A fast and reliable model for bondwire heating
- Test case 7 Reliable RFIC Isolation
- Test case 12 Transformer (academic benchmark for weakly and strongly coupled field/circuit problems)

Link to WP2 deliverables :

- D2.4 Intermediate Report on Methods (a) and algorithms (b) for co-simulation of coupled problems including random parameters without Polynomial Chaos or reduced-order models
- D2.7 Algorithms implemented in software packages for all Tasks 2.1-2.6.

3.2 Mathematical Modeling of Stochastic Coupled Systems

The stochastic modeling for multiphysics problems is outlined now.

3.2.1 Coupled multiphysics problems in nanoelectronics

The coupling of various physical phenomena in nanoelectronics plays an important role in the reliability assessment of the circuit and electronic systems, for example, high-performance applications such as CPUs and RF-circuits or applications related to automotive industry. In both cases various types of coupled effects exist, for example, including a electro-thermal coupling, which is of a great importance in operational cycles. On the one hand, a generated substantial amount of heat affects the voltage and current distribution. On the other hand, it also has an impact on the sources of the heat itself. Also the electro-thermal-stress coupling is investigated in the modeling of

a power-MOS device, both in DC and in the transient regime, while taking the environmental aspects such as metal stack and package into account. As a consequence, designs in nanoelectronics often lead to large-size simulation problems and include strong feedback couplings, whose modeling results in so-called Partial-Differential-Algebraic Equations (PDAEs). In order to solve these coupled PDAE models numerically, various methods have been investigated in the nanoCOPS project including a monolithic approach and a co-simulation framework, see [46, 55, 69]. The complexity of the problems related to the modeling methodology, based on the various mathematical approaches, is schematically shown on Figure 9.

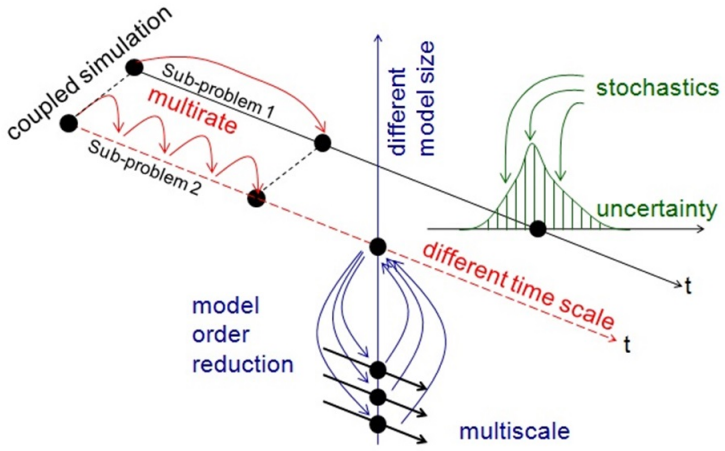

Figure 9: Schematic of a coupled problem (consisting of two sub-problems), including uncertainties. In nanoCOPS, those problems are efficiently solved in time domain and probability space with exploitation of their multirate (different time steps) and multiscale behavior (different discretizations) (figure from [47]).

.

3.2.2 Stochastic coupled problems description

For simplicity a time-dependent coupled problem has been described by two operators F_1 and F_2. In the following, they can represent the ordinary differential equations (ODEs), the differential algebraic equations (DAEs) or the partial differential equations (PDEs) after a semidiscretization in space as follows

$$F_1(y_1(t,p), y_2(t,p), t, p) = 0, \tag{8a}$$
$$F_2(y_2(t,p), y_1(t,p), t, p) = 0. \tag{8b}$$

Here some parameters are defined as $p \in \Pi \subseteq \mathbb{R}^Q$. Furthermore, we assume the time derivatives are included in each part of systems (8) and the operators F_i, for $i = 1, 2$, consist of n_i equations with given initial values for all $p \in \Pi$. Then, the solution of the system (8) is expressed by $y_i : [t_0, t_{\text{end}}] \times \Pi \to \mathbb{R}^{n_i}$ with the coupling variables being a subset of y_i, for each $i = 1, 2$. Surely, the random steady state counterpart of the system (8) reads as

$$F_1(y_1(p), y_2(p), p) = 0, \tag{9a}$$
$$F_2(y_2(p), y_1(p), p) = 0, \tag{9b}$$

For the uncertainty quantification, some parameters, which exhibit a certain level of uncertainty in the model described by (8) or (9), are replaced by independent random variables

$$p : \Omega \to \Pi, \quad p(\omega) = (p_1(\omega), \ldots, p_Q(\omega)), \tag{10}$$

defined on some probability space $(\Omega, \mathcal{A}, P)$ with a joint density $\rho : \Pi \to \mathbb{R}$. That is, we have Q stochastic parameters with independent probability distributions such as Gaussian, uniform, or beta, for example. As a result, the solution of (9) or (8) becomes a (time-dependent) random process. Thus, the statistical information like the expected value and the variance for a function $f : \Pi \to \mathbb{R}$ can be obtained by using (2), (3), (4), (7) (for transient analysis in a component-wise way) provided that the integrals $\mathbb{E}[f(p)]$ and $\mathbb{E}\left[(f(p))^2\right]$ over the parameter space are finite.

3.3 Results for the UQ propagation and stochastic optimization of chosen coupled problems

We present numerical results of the relevant test examples now.

3.3.1 Results for the UQ propagation in a steady state bond wire model (Test case 5)

Due to the continuous shrinking of elements, power densities increase and therefore thermal considerations in an early design stage are of major importance. This indicates the need for coupled electrothermal simulations. Additionally, small feature sizes lead to significant fabrication tolerances that need to be tackled by Uncertainty Quantification (UQ).

When designing bonding wires for the packaging of Integrated Circuits (ICs), the designer is left with the choice of its material and its thickness. There is a tradeoff between minimal cost and maximum performance. Moreover, the thinner the wire, the higher the probability of failure during operation. On the other hand, the length of a wire is predetermined by the geometry of the given package. While the material is commonly chosen according to economic aspects and its physical properties, the leftover design parameter is the wire's thickness. Bonding wire calculators allow to estimate appropriate parameters by simulation. Many electrothermal models have been proposed for dedicated bonding wire simulation. In particular, there are phenomenological models determined from measurement data and models derived analytically or by discretization from the electrothermal problem and combinations of those approaches, see e.g. [52, 51, 70, 31] and the references therein.

To incorporate all physical effects, field simulation of integrated and discrete semiconductor power devices is well established. It is typically based on volumetric space discretization using for example the Finite Element Method (FEM) or the Finite Integration Technique (FIT) [82, 83]. However, the treatment of dynamic electrothermal effects is still challenging due to the coupling [14] and in particular because of multirate and multiscale effects [28, 68]. Resolving small features as thin wires is such a multiscale problem and therefore, many commercial simulators include various surrogate models to avoid discretizing the bonding wire in the computational grid, e.g. [51].

Following [25], we discuss a framework for embedding lumped electrothermal bonding wire models into electrothermal field simulators. A nonlinear electric and thermal network based model is proposed and consistently coupled to the spatial discretization. As an application example, the global sensitivity of the bonding wires' temperatures w.r.t. their geometric parameters is investigated. This is necessary because manufacturing tolerances, measurement inaccuracies and model imperfections lead to deviations between simulation and reality.

We first introduce the coupling between electromagnetics and heat in the continuous setting. Then, the used discretization approach is introduced. After the presence and treatment of uncertainties in the bonding wires are explained, simulation results are discussed and conclusions are drawn.

On the one hand, if an electrical current is applied to a bonding wire, the temperature of the wire increases due to the Joule heating effect. On the other hand, a change in temperature of the wire leads to a change of the material parameters. Neglecting the temperature dependence of the volumetric heat capacity, the nonlinearity of electrical and thermal conductivities in temperature remains. After the introduction of the electrical and thermal sub-problems, this two-directional electrothermal coupling is described.

The distribution of electrical quantities can be described by the current continuity equation. Neglecting capacitive effects, only the stationary current problem

$$-\nabla \cdot \sigma(T)\nabla\varphi = 0$$

with suitable boundary conditions is considered. Here, σ is the electrical conductivity, φ the electrical potential and $T = T(t)$ the time dependent temperature. The spatial dependencies are suppressed to keep the notation short. A generalization to electroquasistatics is straightforward.

Thermal heat is distributed due to conduction, convection and radiation. In the general form, the transient heat equation describes conduction and is given by

$$\rho c\dot{T} - \nabla \cdot \lambda(T)\nabla T = Q(T, \varphi),$$

where ρc is the volumetric heat capacity and λ the thermal conductivity. The power density Q represents heat sources that affect the system. We assume three different sources to contribute to this heat source

$$Q(T, \varphi) = Q_{\mathsf{el}}(T, \varphi) + Q_{\mathsf{bnd}}(T) + Q_{\mathsf{bw}}(T, \varphi).$$

First, heat can be generated by the Joule heating term Q_{el} resulting from the electrical contribution. Secondly, heat exchange with the environment is described by the boundary term Q_{bnd}. Thirdly, the considered bonding wire acts as an external heat source Q_{bw} since it is not resolved by the grid. These quantities will be explained in the following. The heat exchange with the environment is modeled as Dirichlet, adiabatic, convective or radiative conditions.

The boundary term $Q_{\mathsf{bnd}} = Q_{\mathsf{conv}} + Q_{\mathsf{rad}}$ contains a contribution of convective and radiative effects given by

$$Q_{\mathsf{conv}} = -\frac{1}{|V|}\int_{\partial V} \vec{q}_{\mathsf{conv}} \cdot \mathrm{d}\vec{A}, \quad Q_{\mathsf{rad}} = -\frac{1}{|V|}\int_{\partial V} \vec{q}_{\mathsf{rad}} \cdot \mathrm{d}\vec{A}.$$

In these equations, $\vec{q}_{\mathsf{conv}}$ and $\vec{q}_{\mathsf{rad}}$ are the heat fluxes that leave a volume V due to convection or radiation as given by

$$\vec{q}_{\mathsf{conv}} = h\left[T_{\mathsf{bnd}}(t) - T_\infty\right]\vec{n}, \quad \vec{q}_{\mathsf{rad}} = \varepsilon\sigma_{\mathsf{SB}}\left[T_{\mathsf{bnd}}^4(t) - T_\infty^4\right]\vec{n},$$

respectively. Here, $\vec{n}$ is the outward-pointing normal, h the heat transfer coefficient, ε the emissivity and σ_{SB} the Stefan-Boltzmann constant. As boundary effects are dominated by the boundary nodes and the environment, T_{bnd} is the temperature at the boundary and T_∞ the ambient temperature.

By combining the transient heat equation with the stationary current problem, we obtain the nonlinear electrothermal system

$$-\nabla \cdot \sigma(T)\nabla\varphi = 0, \tag{11}$$

$$\rho c\dot{T} - \nabla \cdot \lambda(T)\nabla T = Q(T, \varphi) \tag{12}$$

with suitable boundary and initial conditions. The Joule heating due to the stationary current problem is described by $Q_{\mathsf{el}} = (\nabla\varphi)^\top\sigma(T)\nabla\varphi$ resulting from the electrothermal coupling from electrical to thermal side. The two-directional coupling is established by the temperature dependence of λ and σ.

The coupled electrothermal problem is discretized in space using the FIT [82, 83] on a staggered 3D hexahedral grid pair. For simplicity of notation, a staircase material approximation at the primary grid is assumed, i.e., each primary cell is assumed to consist of a homogeneous material. The discrete unknowns, i.e., the electric potentials Φ as well as the temperatures T are allocated at the nodes of the primary grid. The voltages and the temperature drops at the primary edges are found as differences, i.e., $\widehat{\mathrm{e}} = -G\Phi$ and $\widehat{\mathrm{t}} = -GT$ where G is the discrete gradient operator consisting of 0, 1 and -1 entries according to the topology of the primary grid. The currents $\widehat{\widehat{\mathrm{j}}}$ and the heat fluxes $\widehat{\widehat{\mathrm{q}}}$ are allocated at the facets of the dual grid. The currents and heat fluxes accumulating at the dual cells are calculated by $\widetilde{S}\widehat{\widehat{\mathrm{j}}}$ and $\widetilde{S}\widehat{\widehat{\mathrm{q}}}$ where $\widetilde{S}$ is the discrete divergence operator containing 0, 1 and -1 entries according to the topology of the dual grid. The duality of the grids gives rise to the property $G = -\widetilde{S}^\top$.

The currents $\widehat{\widehat{\mathrm{j}}} = M_\sigma\widehat{\mathrm{e}}$ and the heat fluxes $\widehat{\widehat{\mathrm{q}}} = M_\lambda\widehat{\mathrm{t}}$ are related to the voltages and temperature drops by the electrical and thermal conductance matrices M_σ and M_λ, respectively. In the case of a mutually orthogonal grid pair, every primary edge crosses a unique dual facet perpendicularly. In that case, the primary edges and dual facets can be indexed similarly and the material matrices M_σ and M_λ are diagonal with the entries

$$M_{\sigma,i,i} = \frac{\overline{\sigma}_i\tilde{A}_i}{\ell_i} \quad \text{and} \quad M_{\lambda,i,i} = \frac{\overline{\lambda}_i\tilde{A}_i}{\ell_i}$$

where ℓ_i is the length of primary edge i and $\tilde{A}_i$ is the area of dual facet i. The material parameters $\overline{\sigma}$ and $\overline{\lambda}$ are found by a volumetric averaging of the corresponding parameters of the primary cells touching the considered primary edge.

The thermal capacitance matrix $M_{\rho,c}$ relates the heat power to the temperature change, i.e., $Q_{\dot{T}} = M_{\rho,c}\dot{T}$ and operates between the primary nodes and the dual cells. Also here, a one-to-one relation is present and the indexing scheme is shared. The diagonal entries of $M_{\rho,c}$ read

$$M_{\rho c,j,j} = \overline{\rho c}_j\tilde{V}_j$$

where $\tilde{V}_j$ is the volume of dual cell j. Here, $\overline{\rho c}_j$ is obtained by averaging the volumetric heat capacity of the primary cells touching the considered dual cell j.

The heat generated by the current is calculated at the dual cells, i.e., the voltages $\widehat{\mathrm{e}}$ are interpolated to the midpoints of the primary cells yielding $\vec{E}_k$ where k counts over all primary cells. There, the power density is calculated by $Q_{\mathrm{el},k} = \sigma_k \vec{E}_k \cdot \vec{E}_k$. The electrical contribution to the power then follows from

$$Q_{\mathrm{el}}(T, \varphi) = \tilde{V}_j \overline{q}_j$$

where $\overline{q}_j$ results from averaging the powers from the primary cells to the primary nodes.

The topological operators G and $\widetilde{S}^\top$ and the material matrices M_σ, M_λ and $M_{\rho,c}$ are put together in the discrete counterpart to (11) and (12), i.e.,

$$-\widetilde{S} M_\sigma(T) G \Phi = 0, \tag{13}$$

$$M_{\rho,c} \dot{T} - \widetilde{S} M_\lambda(T) G T = Q(T, \Phi). \tag{14}$$

The degrees of freedom are the discrete temperature vector $T = T(t)$ and the electrical potential vector $\Phi = \Phi(t)$, while $Q = Q_{\mathsf{el}} + Q_{\mathsf{bnd}} + Q_{\mathsf{bw}}$ is the discrete representation of Q. It includes Joule heating by the field model, the boundary term for convective and radiative effects as well as the self-heating of the bonding wires as explained in the following. Subsequently, the time is discretized by the implicit Euler method.

For an overview of the involved quantities and their relation, the discrete electrothermal house based on [27] and [14] is shown in Figure 10. The figure consists of two parts showing the Maxwell house on the left hand side and the thermal house on the right hand side. The coupling is established due to the Joule heating term and the nonlinear electrical conductivity as illustrated.

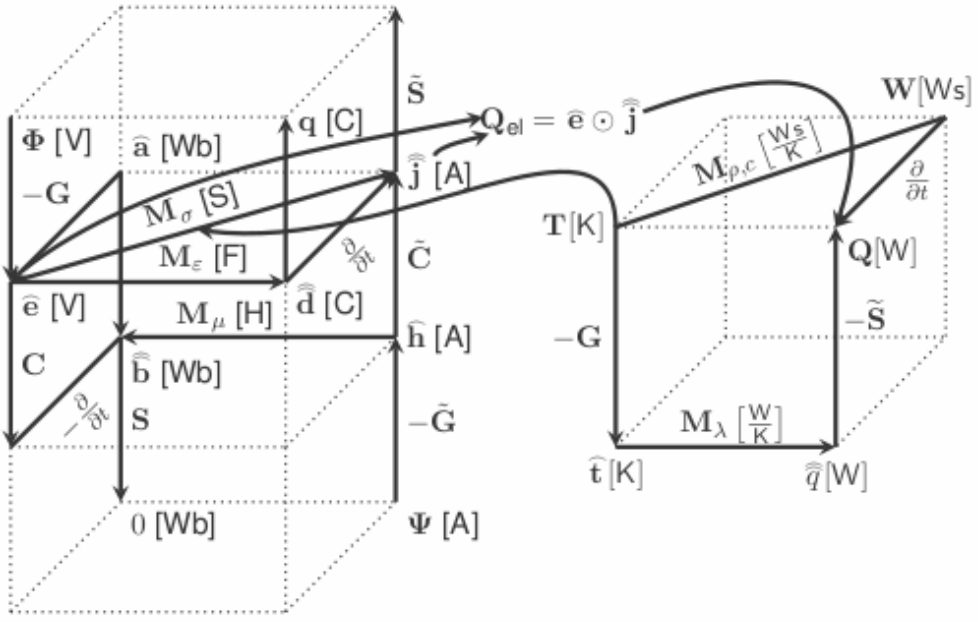

Figure 10: Discrete electrothermal house (figure from [25]).

To account for the different scales of the bonding wires in comparison to any other microelectronic components in their vicinity, the wires are not resolved by the grid but

instead modeled by a lumped element approach. Assuming that conduction is dominant compared to capacitive effects, pairs of mesh points are connected by an electrothermal conductance only. Here, the conductance G_{bw} serves as a placeholder for both the electrical and thermal conductance $G_{\mathrm{bw}}^{\mathrm{el}}$ and $G_{\mathrm{bw}}^{\mathrm{th}}$. This approach is illustrated in Figure 11.

For the implementation, the conductance matrix

$$G_{\mathrm{bw}} = \begin{bmatrix} G_{\mathrm{bw}} & -G_{\mathrm{bw}} \\ -G_{\mathrm{bw}} & G_{\mathrm{bw}} \end{bmatrix}$$

needs to be stamped to the correct positions in the system matrices of (13) and (14). If this is done for all N_{bw} bonding wires present in the model, the extended electrothermal system reads

$$\widetilde{S} M_\sigma(T) \widetilde{S}^\top \Phi + \sum_{j=1}^{N_{\mathrm{bw}}} P_j G_{\mathrm{bw},j}^{\mathrm{el}}(T_{\mathrm{bw},j}) P_j^\top \Phi = 0,$$

$$M_{\rho,c} \dot{T} + \widetilde{S} M_\lambda(T) \widetilde{S}^\top T + \sum_{j=1}^{N_{\mathrm{bw}}} P_j G_{\mathrm{bw},j}^{\mathrm{th}}(T_{\mathrm{bw},j}) P_j^\top T = Q(T).$$

Here, $\widetilde{S}^\top = -G$ represents the negative gradient matrix and P_j is a bonding wire gradient vector consisting of $0, 1$ and -1 entries that additionally handles the incidences between the contacts of the bonding wire j and the grid. The above equation assumes a linear temperature distribution across each lumped element with its average defined by

$$T_{\mathrm{bw},j} = X_j^\top T, \tag{15}$$

The vector X_j contains two $1/2$ entries and averages the temperature from both bonding wire connection nodes. To account for nonlinear temperature distributions, a single bonding wire can be modeled by a more complex model or by a number of concatenated lumped elements resulting in a piecewise linear temperature distribution.

With these quantities defined, the Joule heating of a single bonding wire reads

$$Q_{\mathrm{bw},j} = \Phi^\top P_j G_{\mathrm{bw},j}^{\mathrm{el}}(T_{\mathrm{bw},j}) P_j^\top \Phi.$$

Finally, the contribution of all bonding wires to the right hand side of (14) is given by

$$Q_{\mathrm{bw}} = \sum_{j=1}^{N_{\mathrm{bw}}} X_j Q_{\mathrm{bw,j}}.$$

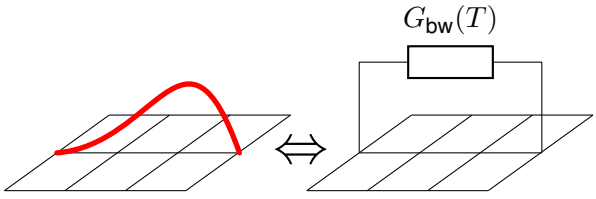

Figure 11: Bonding wire modeling by a lumped element approach (figure from [25]).

While the methodology has already been presented, an application example is given in the following. Bonding wires attached to a chip are modeled using the lumped element approach to realize an electrothermal simulation of the full package. Additionally, UQ is applied to account for the variations in the bonding wire lengths.

The example features 28 contacts and $N_{\mathrm{bw}} = 12$ bonding wires as shown in the X-ray pictures in Figure 12. Each wire connects the chip with one of the contact pads. Because only the contacts are accessible from the outside, a constant voltage is always applied over two adjacent bonding wires (e.g. wires 3 and 4 or wires 7 and 8).

The time until the wire fails depends on the applied voltage, the material properties and the geometry of the wire. Assuming that we know the voltage and the conductivity of the material accurately, the uncertainty is only related to the wires' geometry. While the thickness of the wires can be fabricated very accurately, the only unknown parameter remains to be the length of the wire. This length is not a priori known as it highly depends on the bonding process. By using the X-ray pictures in Figure 12(a) and (b), the lengths have been measured after fabrication.

The correct length of a bonding wire depends on three parameters. First, the minimal length of a wire is given by the direct distance d between contact pad and chip as shown in Figure 13(a). Here, it has been assumed that the bonding was done such that the position of the wire's end points is exactly as planned by the designer. This means that the connection point on the contact pad is equally spaced (length a) to its edges. Secondly, any deviation from the perfect position on the contact pad leads to an elongation Δs that adds up to the corrected distance $D = d + \Delta s$ as depicted in Figure 13(b). Thirdly, any additional bending results in an additional elongation Δh (see Figure 13(c)) giving the total wire length $L = d + \Delta s + \Delta h$. Due to the camera angle in Figure 12(b), the elongation Δh could only be determined for 6 wires. For the other wires, the average value of these 6 measurements has been assumed. In the example presented here, only possible construction errors according to Figure 13(b) and Figure 13(c) have been considered to determine the uncertain elongations Δs and Δh, respectively.

The measurement of these different length parameters has been done for one chip with 12 bonding wire samples using the X-ray pictures shown in Figure 12. Instead of taking the total length L of a bonding wire as the uncertain quantity, the relative elongation $\delta = \frac{L-d}{L}$ is used. The random elongations for all bonding wires, possibly of different

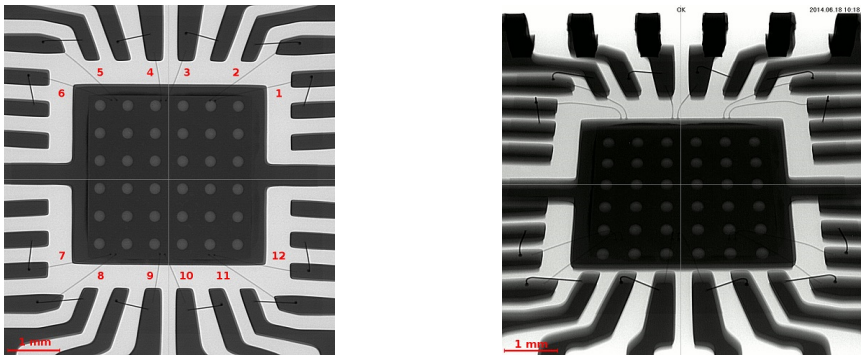

(a) Top view (b) Perspective view

Figure 12: X-ray photos of investigated chip (figure from [25]).

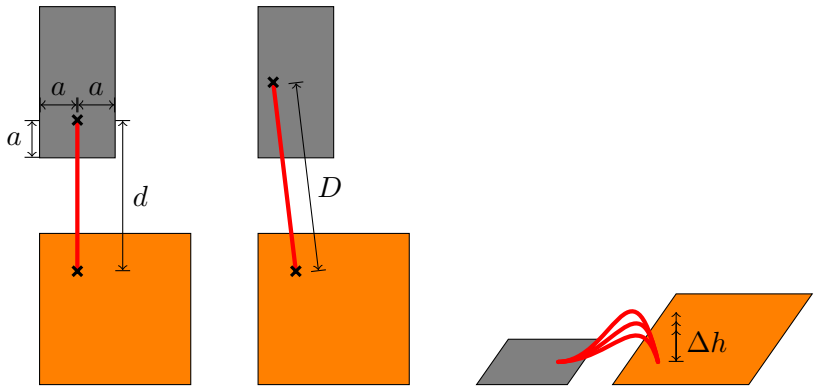

(a) Exact position on contact pad.

(b) Elongation due to misplacement.

(c) Elongation due to bending.

Figure 13: Variability of the bonding wire length due to construction tolerances (figure from [25]).

lengths, are determined by the probability density function for δ. From the histogram shown in Figure 14, we identify a normal distribution with expectation value $\mu_{\text{BW}} = 0.17$ and standard deviation $\sigma_{\text{BW}} = 0.048$ albeit the rather small number of samples. A more rigorous analysis would require the fabrication of additional test chips.

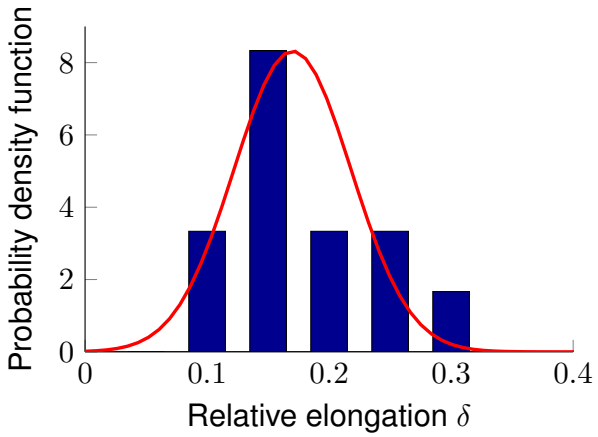

Figure 14: Probability density function for the relative elongation δ (figure from [25]).

Particularly, if the number of random input parameters is high, the Monte Carlo (MC) method is a well established technique to quantify the variation of outputs [24]. To this end, MC solves repeatedly the problem, i.e., in our case (13-14), for random sets of parameters. Naturally, the error committed by taking a finite amount of samples M is decreasing with increasing number of samples. It serves as a guideline for the necessary amount of samples and is approximated by

$$\text{error}_{\text{MC}} = \frac{\sigma_{\text{MC}}}{\sqrt{M}}, \tag{16}$$

where σ_{MC} is the standard deviation approximated with the M samples. The estimator unveils the rather slow convergence in terms of $\sqrt{M}$. However, the application of other methods is straightforward.

The chip is modeled following the geometry obtained by measuring the X-ray pictures

shown in Figure 12. All 28 contact pads have been modeled to be of equal width $w_{\text{pad}} = 0.311\,\text{mm}$. 24 of them have the same length $\ell_{\text{pad}} = 1.01\,\text{mm}$, whereas the other 4 have a length $L_{\text{pad}} = 1.261\,\text{mm}$. As an approximation, all structures are approximated using rectangular shapes. Copper is chosen as the material for the bonding wires, the contact pads and the chip while epoxy resin is used for the mold compound. Additionally, the outer end of each contact pad is modeled as Perfectly Electric Conducting (PEC). In Figure 3, the model and the computational mesh are shown. The corresponding materials and their conductivities at $T = 300\,\text{K}$ are collected in Table 3.

As electric boundary conditions, the PEC nodes are connected to a constant potential of $V_{\text{dc}} = \pm 20\,\text{mV}$ such that the voltage over each of the 6 pairs of bonding wires equals $V_{\text{bw}} = 40\,\text{mV}$. For all other boundaries, current flow is prevented by setting homogeneous Neumann conditions. All non-PEC nodes are set to the initial potential $V_{\text{init}} = 0\,\text{V}$ at time $t = 0\,\text{s}$.

The thermal boundary conditions are as follows. For all boundaries, convection and radiation conditions with a heat transfer coefficient of $h = 25\,\text{W/m}^2\text{/K}$ and an emissivity of $\sigma_{\text{rad}} = 0.2475$ are chosen, respectively. As initial conditions, the whole chip is assumed to be at the ambient temperature $T_\infty = 300\,\text{K}$.

Since a possible failure of the bonding wires is investigated, we are interested in the temperature of the wires over time. As the wires themselves are not resolved by the grid, the representative wire temperatures are extracted from the end-points of the wires as given by (15). The expectation value $E_j(t)$ for each wire temperature is calculated by averaging over all M samples, i.e.,

$$E_j(t) = \frac{1}{M} \sum_{m=1}^{M} T_{\text{bw},j}^{(m)}(t).$$

With the objective in mind that none of the bonding wires should fail, it is sufficient to pick out the wire that experiences the highest expected temperature $E_j(t)$. Therefore, we define $E_{\max}(t)$ to be the maximum of the expectation values of all wires, viz.

$$E_{\max}(t) = \max_j [E_j(t)], \text{ for } j \in \{1, ..., N_{\text{bw}}\}. \tag{17}$$

Other stochastic moments, for example the variance or standard deviation, can be determined analogously.

A Monte Carlo simulation with $M = 1000$ samples was carried out using the probability density function from Figure 14. With the simulation parameters as given in Table 4, the Monte Carlo error calculates to $\text{error}_{\text{MC}} = 0.147\,\text{K}$. In Figure 15, the resulting expectation value $E(t)$ for the temperature of the hottest wire is plotted over time. Error bars indicate the output variation resulting from the variability in the input, being the

Table 3: Material Properties @ $T = 300\,\text{K}$

Region	Material	λ [W/K/m]	σ [S/m]
Compound	Epoxy resin	0.87	1×10^{-6}
Contact pad	Copper	398	5.80×10^7
Chip	Copper	398	5.80×10^7
Bonding wire	Copper	398	5.80×10^7

Table 4: Simulation Parameters.

Parameter	Value
Bonding wire voltage V_{bw}	40 mV
End time	50 s
No. of time steps	51
No. of MC samples	1000
Wires' diameter	25.4 µm
Average wires' length $\bar{\text{L}}$	1.55 mm
Ambient temperature	300 K
Heat transfer coefficient	25 $\text{W}/\text{m}^2/\text{K}$
Emissivity	0.2475

length of the wire. Assuming that a bonding wire fails mainly due to the degradation of the surrounding mold, a critical temperature $T_{\text{critical}} = 523\,\text{K} \approx 250\,^\circ\text{C}$ is defined to mark the threshold for failure. This critical temperature is inserted as a red line to indicate the upper bound for design validity.

Thanks to convection and radiation at the chip's boundaries, a stationary situation is observed after $t \approx 50\,\text{s}$. Then, the mean temperature of the hottest wire is still lower than the critical temperature T_{critical}. However, the uncertainty in the lengths of the bonding wires leads to variations of the temperature with a standard deviation of $\sigma_{\text{MC}} = 4.65\,\text{K}$. As the failure of bonding wires is a relevant reliability problem, the 6σ-deviation is visualized by the error bars in the figure. For the given configuration, the variation may indeed influence whether a bonding wire fails or not. This can be seen as the error bars cross the critical temperature for $t > 26\,\text{s}$. Figure 16 shows the spatial temperature distribution at $t = 50\,\text{s}$. As one would expect, the region where the contacts are closest and are connected by the shortest wires experience the largest temperature increase. These wires are the most sensitive in the system. This is confirmed by the fact that one of these wires is the one with the maximal temperature evolution shown in Figure 15.

To conclude, bonding wires are included as lumped elements in a coupled electrothermal field model. By this, the behavior of the bonding wires can be checked already in the design phase. The thickness and material of the bonding wires can be selected by evaluating the simulation results.

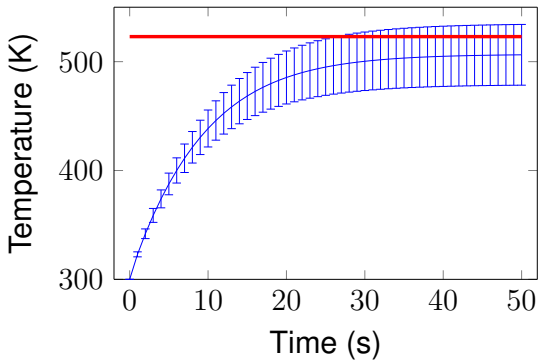

Figure 15: Expected temperature at end-point of the hottest bonding wire with plotted $6\sigma_{\text{MC}}$-deviation over time. In red, the critical temperature of the wire's material is indicated (figure from [25]).

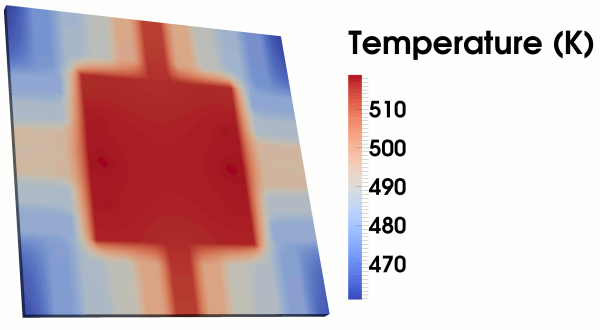

Figure 16: Spatial temperature distribution at $t = 50\,\mathrm{s}$ (figure from [25]).

As a possible application, a stochastic model for uncertain bonding wire lengths has been set up for an exemplary chip package. This uncertainty is included in the coupled electrothermal field model and affects the final operating temperature of the bonding wires. It is quantified in terms of expectation value and standard deviation. Concerning the investigated uncertainty of the bonding wires' lengths, it is important to recall that the used data set to extract the probability density function is very small. However, the simulation result of the presented example indicates that the relative influence of the uncertainties can be significant for the validity of bonding wire design.

3.3.2 Results for the robust topology optimization of a steady state Power Transistor model (Test case 1)

We dealt with the topology optimization of a power transistor device when taking geometrical and material uncertainties into account. On one hand we could use the advanced technologically ptm-ET (MAGWEL) solver for the simulation of the complicated structure of a power MOS device in order to predict behavior of the device in critical conditions. On the other hand, our methodology allowed for the solution of a real engineering problem such as an anomalous failure mechanism due to the thermal runway. Specifically, we reduced the thermal instability by optimizing the geometry within the device layout, while taking both the conductive power losses and shape variations of source/drain into account. Thus, in [63] and [62] we mainly focused on a shape/topology optimization problem of a power MOS device with three metal layers under geometrical and material uncertainties to reduce the current density overshoot. This problem, occurring in the automotive industry, yields a stochastic electro-thermal coupled problem. It is a multi-finger MOSFET power transistor with a stripe cell structure, which consist of several thousands of parallel channel devices.

The source and drain contacts are located on the top metal finger of the design, as shown in Figure 17. A series of metal stripes and complex via patterns transport the current to drain and away from the sources of the individual channels. Consequently, the multi-dimensional current flow is governed by a coupled time-dependent system of stochastic Partial Differential Equations (PDEs). Its solution enables to investigate the propagation of uncertainties through a 3-D model, which affect yield and performance of a power transistor. In particular, $p(\omega) = [\sigma_3(\omega), W_2(\omega), C_v(\omega), V_{\mathrm{D}}(\omega), V_{\mathrm{S}}(\omega)]$ are taken as parameters, in which the conductivity of the Metal3 layer, σ_3, the thickness of the Metal2, W_2, and the thermal capacitance of the Via12, C_v, and the drain and source

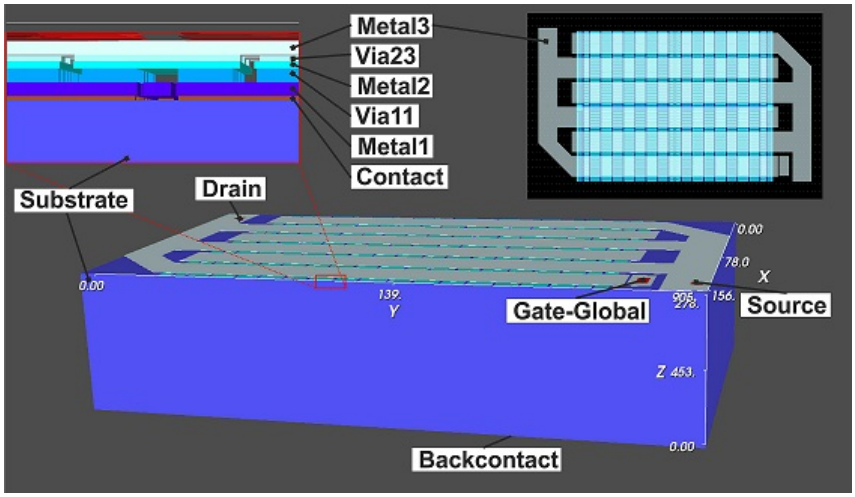

Figure 17: Power Transistor Model (figure from [46, 62]).

contacts are considered, see also Figure 18. Here ω varies over some probability space and the probability distributions of the parameters are predetermined. The PDEs are equipped with random Dirichlet boundary conditions that describe the potentials at the drain and source pads.
To reduce the current density overshoots in the area of the contact layer of the power device, as basic random-dependent cost functional

$$F(\upsilon) = w_1 \int_{\mathrm{D}} Q_{\mathrm{e}}\left[\upsilon, V(\upsilon)\right] \mathrm{d}x + w_2 \int_{\Gamma} h\left[V(\upsilon)\right] \mathrm{d}\gamma, \tag{18}$$

was taken, where the dissipation power Q_{e} is analyzed in the area of Metal3 layer $\mathrm{D} \subset \mathbb{R}^3$, and the source voltage term h is represented by the random Dirichlet boundary condition in the area of the source and drain pads $\Gamma \subset \mathbb{R}^2$. The variable υ is defined as $\upsilon = (x, p\,(\omega))$, whereas the weights w_1 and w_2 refer to known a priori information about objectives.
For the robust optimization one minimizes a PDE-constrained minimization problem

$$\min_{\boldsymbol{\upsilon}} \mathbb{E}\left[F(\boldsymbol{\upsilon})\right] + \eta \sqrt{\mathrm{Var}\left[F(\boldsymbol{\upsilon})\right]}, \tag{19}$$

where $\eta = 3$ was taken. The Stochastic Collocation Method, based on Polynomial Chaos Expansion (PCE) [84], provided a response surface model to estimate the expectation $\mathbb{E}\left[F_{\boldsymbol{\upsilon}}(\boldsymbol{\upsilon})\right]$ and the standard variation $\sqrt{\mathrm{Var}\left[F_{\boldsymbol{\upsilon}}(\boldsymbol{\upsilon})\right]}$. Combining with a Topological Derivative Method, we could reduce hot spot phenomena in a robust sense, see Figure 19 and 20.

Additionally, we present also the course of the total conductance, the course of the total power and the course of the total current during the optimization in Figure 21, in Figure 23 and in Figure 22, respectively.

3.3.3 Results of the UQ analysis for a transient nonlinear field/circuit coupled problem (Test case 12)

We solved a stochastic field/circuit problem, shown in a Figure 24 using a monolithic approach. The stochastic eddy-current field problem, defined in a spatial domain $D \in$

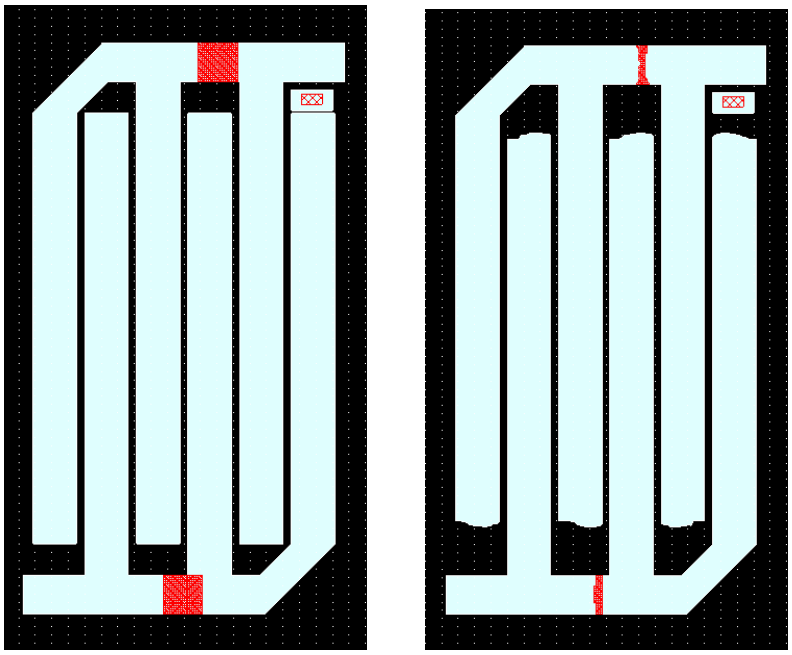

(a) initial configuration (b) optimized configuration

Figure 18: Shapes of the metal3 layer as well as the drain and source pads (red color) for: the initial configuration (a), the optimized model in the 18th iteration (b) (figures from [62]).

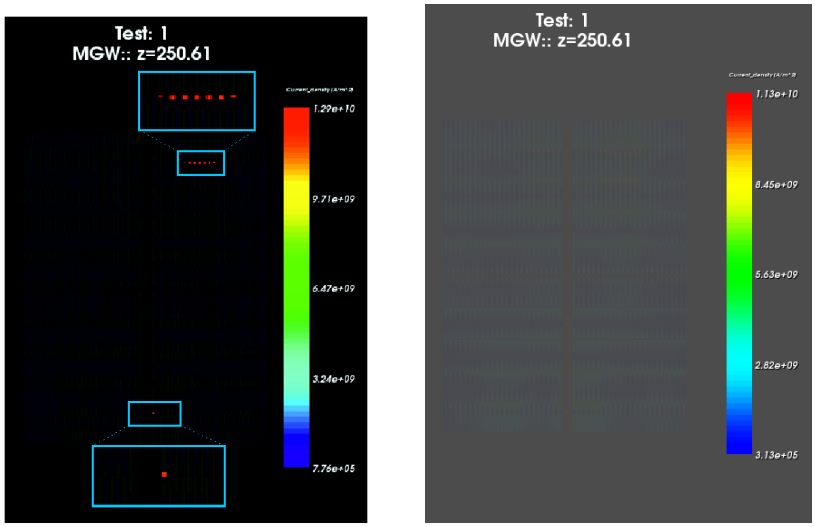

(a) initial configuration (b) optimized configuration

Figure 19: The current density for the initial model (CD) in the contact layer - hot spots, represented, by 8 red dots in the enlarged blue box (a) and the CD in the contact layer after optimization (b) (figures from [62]).

$\mathbb{R}^2$ and a time domain $[t_0, t_{\text{end}}]$, is governed by the random quasi-linear equation

$$\sigma \partial_t a + \nabla \times \Big((\nu(|\nabla \times a|)\ \kappa(x,\omega))\ \nabla \times a \Big) = \chi j, \tag{20}$$

where $\omega \in \Omega$ denotes the random inputs of the model, $a := a(x,t,\omega)$ is the magnetic vector potential (with homogeneous Dirichlet conditions), σ and ν are conductivity and reluctivity, respectively. Additionally, the function $\kappa(x,\omega)$ has been introduced in order

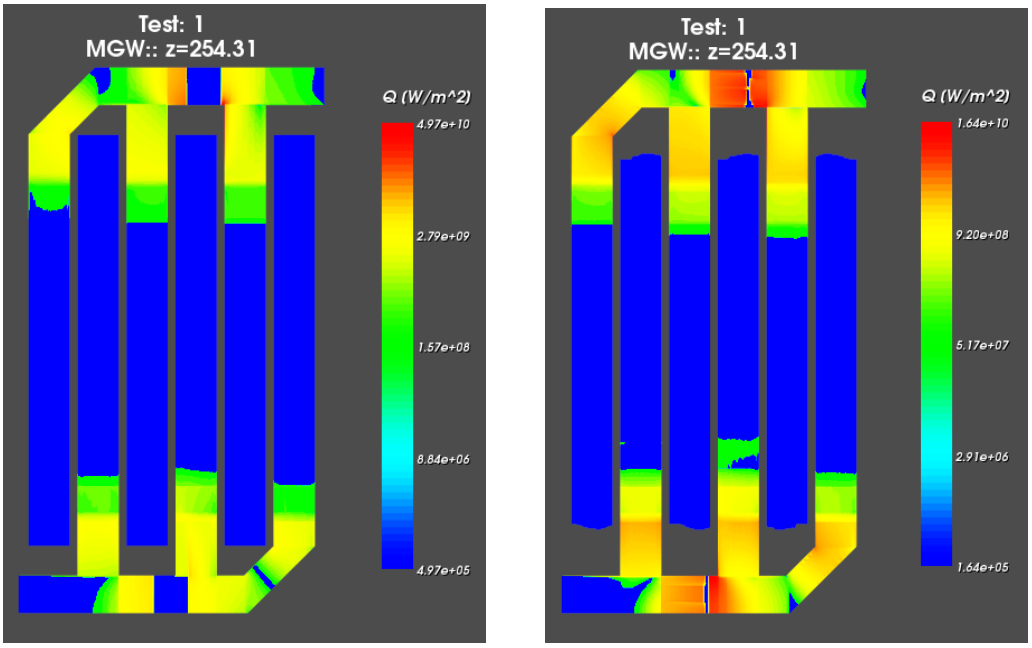

(a) initial configuration (b) optimized configuration

Figure 20: The heat flux density (HFD) in the metal3 layer for initial model (a) and the HFD in the optimized topology (b) [62].

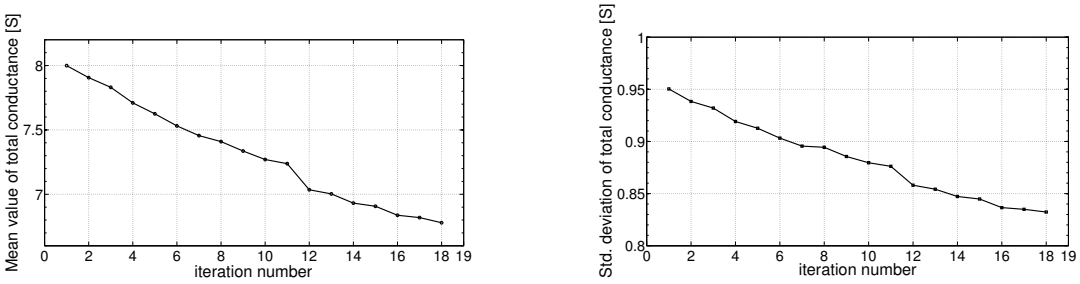

(a) mean values (b) standard deviations

Figure 21: The total conductance as a function of the iteration steps: mean value (a) and standard deviation (b) [62].

to model the local degradation of material (reluctivity). It has been parameterized by a truncated Karhunen-Loève Expansion (KLE) [73] with N terms, i.e.,

$$\kappa(x,\omega) \approx \overline{\kappa}(x) + \sum_{i=1}^{N} \hat{\kappa}_i(x) Z_i(\omega), \tag{21}$$

where $\overline{\kappa}(x)$ denotes the mean of the random field, the functions $\hat{\kappa}_i(x)$ are determined by the eigenvalues and eigenfunctions of the assumed covariance function, e.g., the exponential covariance function, and $Z_i(\omega)$ are uncorrelated [84]. In eq. (20), the winding functions $\chi = [\chi_1, \ldots, \chi_l, \ldots, \chi_L]^\top$ are functions of space that distribute the lumped currents $j = [j_1, \ldots, j_l, \ldots, j_L]^\top$ in the 2D domain [15, 71]. To establish the

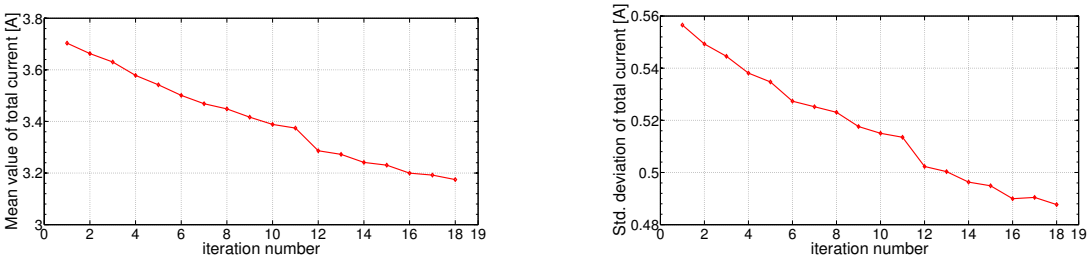

(a) mean values (b) standard deviations

Figure 22: The total current as a function of the iteration steps: mean value (a) and standard deviation (b) [62].

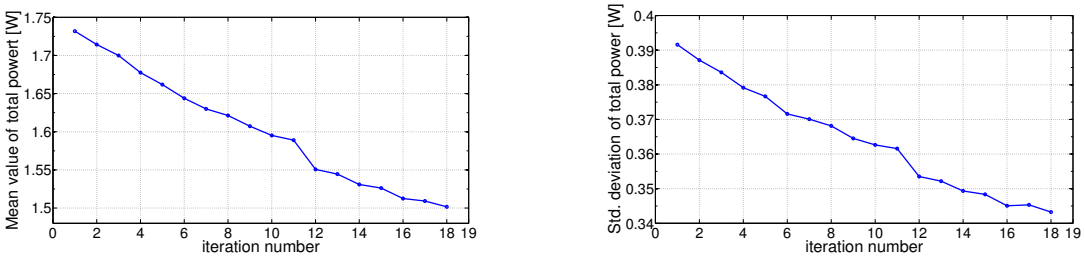

(a) mean values (b) standard deviations

Figure 23: The total power as a function of the iteration steps: mean value (a) and standard deviation (b) [62].

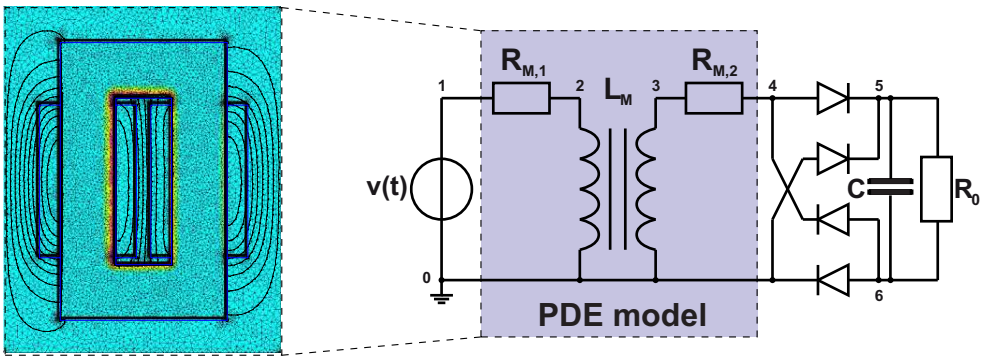

(a) 2D transformer FEMM **(b) rectifier circuit with embeded FEMM model**

Figure 24: Nonlinear Field/Circuit configuration [15, 71] using FEMM [49] as prototype field simulator.

circuit coupling we calculate

$$\partial_t \int_D \chi_l a \, \mathrm{d}x + R_l j_l = v_l \qquad l = 1, \ldots, L, \tag{22}$$

where $R_l j_l$ is some voltage loss. Each conductor has its own conductance and R_l is given by $\int_D \frac{1}{\sigma_l}\chi_l \cdot \chi_l \mathrm{d}x$, see [71, Eq. (17)]. The v_l in (22) are the couplings to the circuit system of stochastic differential-algebraic equations [37]

$$\begin{aligned} A_{\mathsf{C}} \tfrac{\mathrm{d}}{\mathrm{d}t} q_{\mathsf{C}}(A_{\mathsf{C}}^\top u, t) + A_{\mathsf{R}} g_{\mathsf{R}}(A_{\mathsf{R}}^\top u, t) + A_{\mathsf{L}} i_{\mathsf{L}} \\ + A_{\mathsf{M}} j + A_{\mathsf{V}} i_{\mathsf{V}} + A_{\mathsf{I}} i_{\mathsf{s}}(t) = 0, \\ \tfrac{\mathrm{d}}{\mathrm{d}t} \Phi_{\mathsf{L}}(i_{\mathsf{L}}, t) - A_{\mathsf{L}}^\top u = 0, \\ A_{\mathsf{V}}^\top u - v_{\mathsf{s}}(t) = 0, \end{aligned}$$

with additional incidence matrices A_* such that $v_l = A_l^\top u$, or $v = (v_1, ..., v_L)^\top = A^\top u$, for suitable A_l or A) and constitutive laws for (nonlinear) conductances, inductances and capacitances (random functions with subscripts R, L and C, determined by, e.g., the statistical moments), independent sources i_{s} and v_{s}, unknowns are the potentials $u := u(t, \omega)$ and currents $i_{\mathsf{L}} := i_{\mathsf{L}}(t, \omega)$ and $i_{\mathsf{V}} := i_{\mathsf{V}}(t, \omega)$.
To perform the UQ analysis, the nominal parameters of all the four diodes as well as the resistance and the capacitance of the low pass filter have been replaced by

$$\begin{aligned} \tilde{I}_{\mathsf{S}}(p_1) := I_{\mathsf{S}}(1 + 0.05p_1), \quad \tilde{V}_{\mathsf{th}}(p_2) := V_{\mathsf{th}}(1 + 0.05p_2), \\ \tilde{R}(p_2) := R(1 + 0.1p_3), \quad \tilde{C}(p_4) := C(1 + 0.1p_4) \end{aligned}$$

with independent, uniformly distributed, random variables $p_j \in [-1, 1]$, for j = 1, ..., 4. Hence, a relatively high uncertainty of 10% or 5% is considered for each parameter. The same procedure has been conducted for other stochastic parameters (with the variance of 10% for each component) related to the first seven components of the KLE that capture 95% of the random field energy. For the purpose of modeling of the transformer core, we consider a random field of reluctivity with one mean and an exponential two-point covariance function

$$C(x, y) = \delta^2 \exp(-\|x - y\|_2 / L), \tag{23}$$

with δ = 0.1 and L=10 being the correlation length. This resulted in 22 deterministic

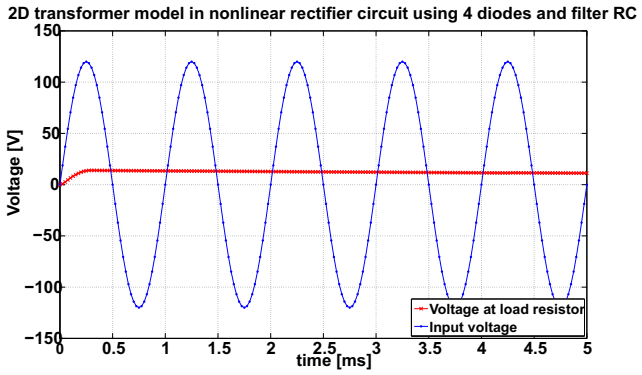

Figure 25: Output/input relation in a bridge rectifier with an RC filter [4].

transient simulations of a rectifier circuit model. In each simulation, the degradation of an iron core of the transformer has been taken into account using a KLE dimension-reduction technique. Figure 26 presents the approximation of the mean and standard deviation obtained by the numerical simulation using the non-intrusive method (SCM).

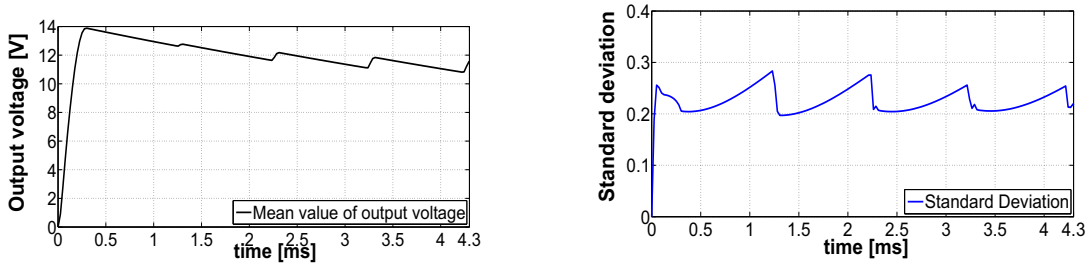

(a) mean values (b) standard deviations

Figure 26: Expected value (a) and standard deviation (b) of the solution of the bridge rectifier with random parameters [4].

The result of the variance-based sensitivity analysis, see [58, 57, 77], is depicted on Figure 27. It shows that the output voltage is more or less equally sensitive to all considered parameters.

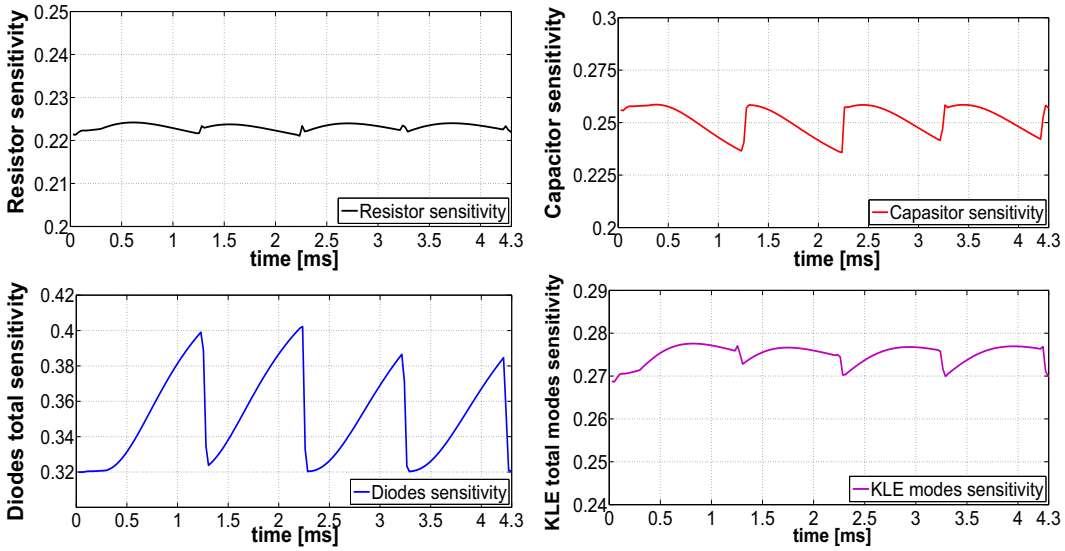

Figure 27: The variance based sensitivities calculated for the resistance, capacitor and diodes parameters and of the KLE components [4].

3.3.4 Results of the UQ transient analysis for the Power Transistor model (Test case 2a)

The implementation at MAGWEL deals with the electro-thermal coupling problem in an ab-initio self-consistent manner [45, 12]. In this case, electrical and thermal equations are solved simultaneously and self-consistently from a single set of equations. Accurate modeling of metal layers as required for advanced integrated BCD (Bipolar-CMOS-DMOS) technologies has been obtained by the application of a high spatial resolution. At the same time, the simulator uses a well-adopted mesh for the substrate, which is important for the simulation of the temperature. Consequently, both the voltage drop in the on-chip metallization and the device temperature can be determined without sacrificing accuracy. Joule self-heating and heat flow in metal is modeled together

with non-linear temperature-dependent electrical and thermal resistivity and thermal capacitances of materials [11, 45]. The electrical part of the integrated field solver [45] addresses the current-continuity equation and Ohm's law

$$\nabla \cdot J = 0, \qquad J = \sigma(T)E, \tag{24}$$

where J and E denote the current density and the electrical field, respectively, and σ is the temperature-dependent electrical conductivity. The thermal part of the solver refers to the heat equation which is controlled by Joule's law

$$\partial_t U = -\nabla \cdot Q + Q_e, \quad Q = -\lambda \nabla T, \quad U = C_v(T - T^*), \tag{25}$$

where the local heat generation is defined by $Q_e = J \cdot E$. Furthermore, C_v is the constant-volume heat capacitance of the material, T refers to the reference or ambient temperature, λ represents the thermal conductivity. The Neumann (adiabatic) boundary condition is imposed on the side walls of the simulation domain. The solution of (25), assuming the heat source is known, provides the needed information about the temperature to (24). The source may comprise several contributors such as the boundaries of the domain with heat-injecting or extracting properties or the Joule self-heating component Q_e. To perform the uncertainty quantification, some parameters $\tilde{\mathrm{p}}$ in the model defined by the coupled system (24) and (25) have been substituted by independent random variables $\vec{p} = (\epsilon(\omega), W_k(\omega), \sigma_k(\omega), C_v(\omega)))$ defined on some probability space. Consequently, the model for a semiconductor device [78, 74] stated on a bounded domain $D \subset \mathbb{R}^d$ is governed by the coupled stochastic partial differential equations (PDEs)

$$\begin{cases} \nabla \cdot (\epsilon \nabla V) = \rho, \\ \nabla \cdot \vec{J}_{(p)} + q\partial_t p + qR(p,n) = 0, \\ \nabla \cdot \vec{J}_{(n)} - q\partial_t n - qR(p,n) = 0, \\ \vec{J}_{(n,p)} = q\ (n,p)\ \mu_{(n,p)} \cdot \nabla V \pm qD_{(n,p)} \nabla (n,p), \\ C_v \partial_t T = \nabla \cdot \lambda(T) \nabla T + \sigma(T) \|\nabla V\|^2, \end{cases} \tag{26}$$

equipped with suitable boundary conditions, where ρ, ϵ and q denote the charge density, the permittivity and the elementary charge, respectively. In this model, generation-recombination processes are involved by the recombination rate R, for example, the Shockley-Read-Hall term.The electrical field $\vec{E} := E(x,t,\omega)$ is determined by the electric scalar potential $V := V(x,t,\omega)$. Furthermore, n and p, represent the concentration of holes and electrons, while D_n, D_p, μ_n, μ_p, $J_n := J_n(x,t,\omega)$, $J_p := J_p(x,t,\omega)$ are the diffusion, mobility and currents densities of electrons and holes, respectively. The symbol (n,p) describes in compact way equations for electrons and holes. In this case, also temperature is defined as $T = T(x,t,\omega)$. For the kth conductive layer of the model, the σ is represented by $\sigma = W_k \sigma_k$, where W_k denotes the size of the layer, for example, the thickness.

The problem with uncertainty quantification of both material and geometrical parameters comes from the automotive industry, where there is a need to handle the demanding electro-thermal operational constraints to design both components and systems. First, a similar structure to the one proposed in *Use Case I: Power-MOS - electro-thermal-stress coupling*, shown in Figure 28(b), has been considered as a case study. The geometrical finger structure of a device design has been shown in Figure 28(a). For uncertainty quantification, the coupled problem defined by stochastic PDEs (26) is

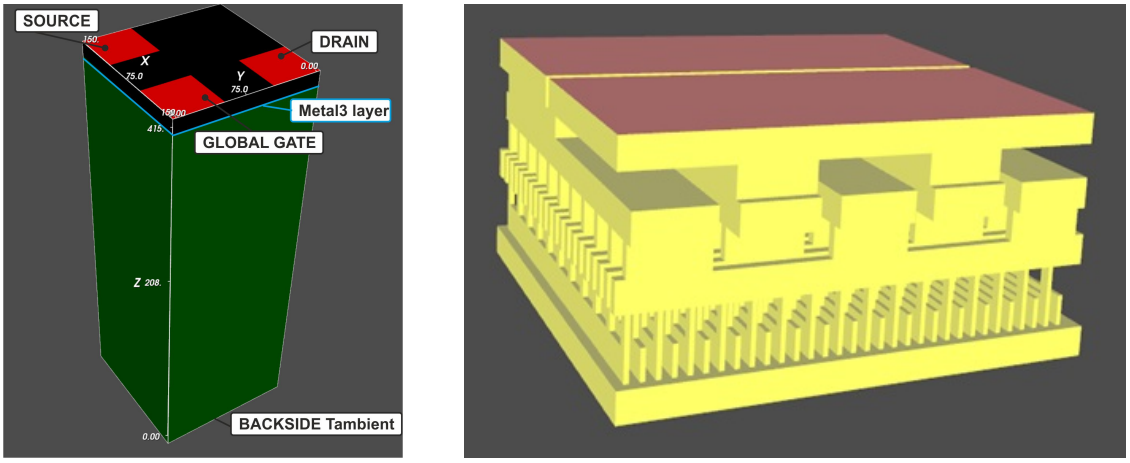

(a) Part of the finger structure in a typical device of a power transistor.

(b) Case I: The geometry of the power transistor.

Figure 28: The layout of the power transistor (figures from [47, 61]).

solved by the deterministic MAGWEL solver [45] at every quadrature grid point using a type of the stochastic collocation method. In the case of the uncertainty of geometry, the thickness variation has been modeled by Gaussian distribution. The nominal and mean value as well as the standard deviations caused by uncertain geometry have been shown on Figure 29. A similar analysis has been performed when conductivity is treated as uncertain parameter. The UQ propagation in the part of the power device caused by conductivity variation is presented in Figure 30.

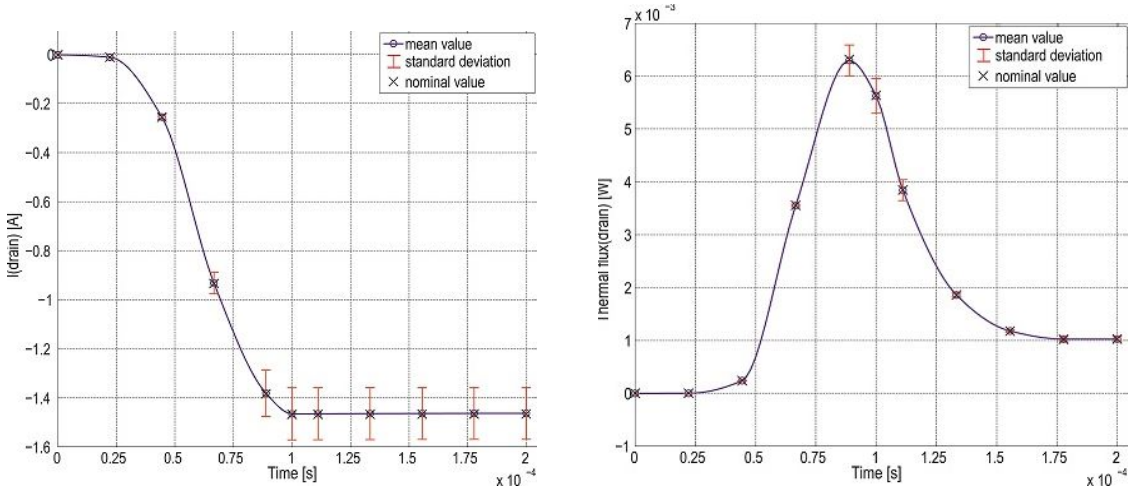

Figure 29: UQ analysis for the thickness of the Metal3 layer modeled by a Gaussian distribution with 10% variation around a nominal value 1μm [61].

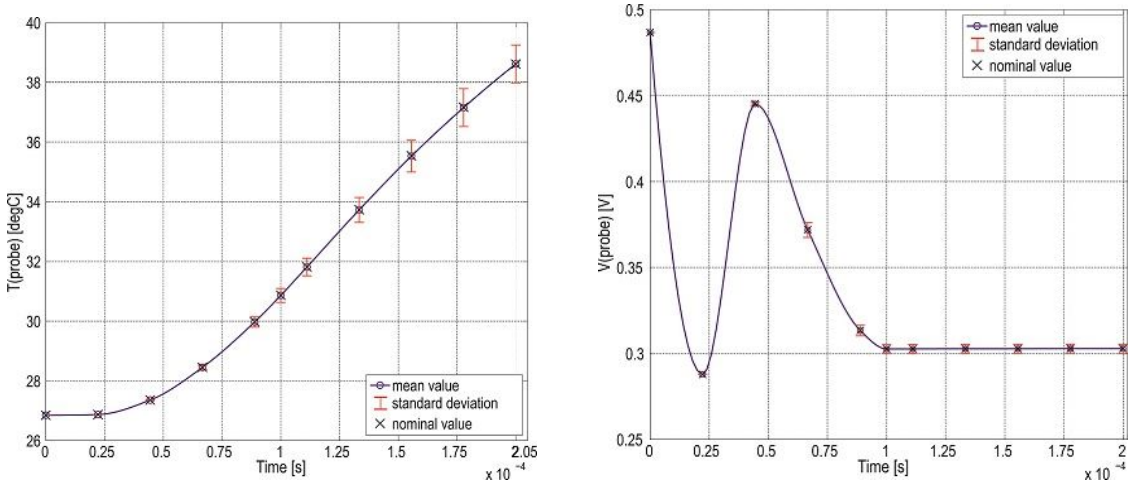

Figure 30: UQ analysis for σ_k (of the Metal3 layer) modeled by a uniform distribution with 15% variation around a nominal value 2e7 S/m [61].

4 Parameterized MOR for uncertainty quantification

This section focuses on using parametric MOR (PMOR) to accelerate non-intrusive uncertainty quantification (UQ), which corresponds to Task T2.3. In non-intrusive UQ, a parametric system needs usually to be solved at many different parameter samples, which is computationally expensive when the parametric system is of large dimension, e.g., a dynamical system resulting from discretization of partial differential equations. Parametric MOR [18], which builds a reduced order parametric system of a much lower dimension for the relevant computations at all parameter samples, is a powerful method to reduce the high computational cost.

(P)MOR has been proved to be efficient in many application areas such as optimization [22] and UQ [20, 85, 56, 19, 21]. Various (P)MOR methods have been proposed within the nanoCOPS project such as balanced truncation [54], multi-moment-matching methods, and reduced basis methods [19, 20, 21]. Another type of MOR, where insignificant input random variables are detected by a sensitivity analysis and reset back to constants, is presented in [58]. Some intermediate results have been reported in deliverable D2.2 [2].

The focus of this section is PMOR-based UQ for the power-MOS device, for which the multi-moment-matching method is shown to be highly accurate, robust and efficient.

4.1 Mathematical modeling of the Power-MOS device

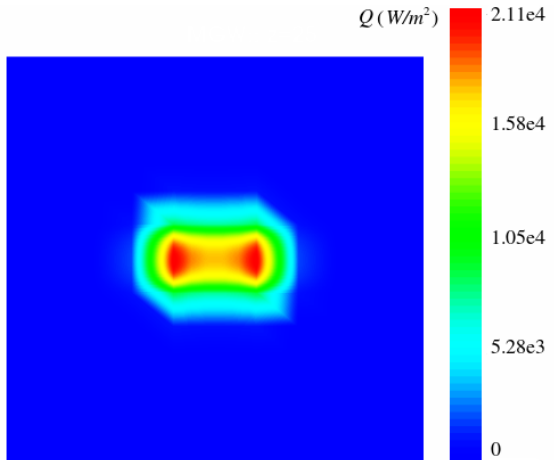

Figure 31: Heat flux density of the power-MOS device on the back contact at $t = 10^{-6}$ s (figure from [46]).

The model of interest in this section is a Power-MOS device shown in Figure 28(a) [85]. The device has three contacts: the drain, the source, and the back contact. Here we study the system behavior within the time interval $t \in [0\,\text{s}, 10^{-6}\,\text{s}]$, where 10^{-6} s is the rise time of the source voltage. The main interest of our analysis is to study how an electrical excitation influences the electrical and thermal field. As is shown in Figure 31, the circuit is heated up because the electrical excitation results in Joule self-heating:

$$Q_{\text{SH}} = \vec{E} \cdot \vec{J}.$$

The dynamics of the Power-MOS device is described by the electrical and the thermal sub-systems. The electrical sub-system can be described by

$$\begin{aligned}
&\nabla \cdot J + \frac{\partial \rho}{\partial t} = 0, \\
&J = \sigma \cdot E, \quad E = -\nabla U, \\
&\rho = -\nabla \cdot (\epsilon \nabla U),
\end{aligned}$$

where J is the current density, E is the electrical field, U is the electrical potential, σ is the electrical conductivity, ϵ is the permittivity, and ρ is the charge density. In this section, we ignore both the local charging, i.e., $\epsilon = 0$ and $\rho = 0$, and the dependence of the electrical conductivity σ on temperature, i.e., the electrical sub-system is independent of the thermal sub-system, and obtain the following simplified governing differential equation, which is time-independent:

$$\nabla \cdot (\sigma \cdot \nabla U) = 0.$$

The thermal sub-system is governed by similar equations:

$$\begin{aligned}
&\nabla \cdot \phi_q + \frac{\partial w(T)}{\partial t} = Q, \\
&\phi_q = -\kappa \nabla T, \\
&w(T) = C_T (T - T_{\mathsf{ref}}),
\end{aligned}$$

where ϕ_q is the heat flux, w is the local energy storage, C_T is the thermal capacitance, and Q represents heat sources or sinks. For the thermal sub-system, we also ignore the dependence of the thermal capacitance on the temperature.

The inputs of the system include the voltages (V) and temperatures (T) of the three contacts, namely:

$$\begin{aligned}
&V_{\mathsf{drain}}(t) = V_{\mathsf{back}}(t) = 0\,(\mathsf{V}), \quad V_{\mathsf{source}}(t) = 10^7 t\,(\mathsf{V}), \quad (t \in [0\,\mathsf{s}, 10^{-6}\,\mathsf{s}]) \\
&T_{\mathsf{drain}}(t) = T_{\mathsf{source}}(t) = T_{\mathsf{back}}(t) = 300\,(\mathsf{K}).
\end{aligned}$$

The outputs we consider here include the currents (I) and thermal fluxes (ϕ) of the three contacts. The electro-thermal model of the power-MOS device that we consider in this section is

$$\begin{cases}
A_{\mathsf{E}}(p) x_{\mathsf{E}}(p,t) = -B_{\mathsf{E}}(p) u(t), & \text{(Electrical Part)}, \quad \text{(27a)} \\
E_{\mathsf{T}}(p) \dot{x}_{\mathsf{T}}(p,t) = A_{\mathsf{T}}(p) x_{\mathsf{T}}(p,t) + B_{\mathsf{T}}(p) u(t) \\
\qquad\qquad + F(p) \times_2 x_{\mathsf{E}}(p) \times_3 x_{\mathsf{E}}(p), & \text{(Thermal Part)}, \quad \text{(27b)} \\
x_{\mathsf{T}}(p,0) = x_{\mathsf{T}}^0,\ x_{\mathsf{E}}(p,0) = x_{\mathsf{E}}^0, & \text{(Initial Conditions)}, \quad \text{(27c)} \\
y(p,t) = C_{\mathsf{E}}(p) x_{\mathsf{E}}(p,t) + C_{\mathsf{T}}(p) x_{\mathsf{T}}(p,t) + D(p) u, & \text{(Output)}. \quad \text{(27d)}
\end{cases}$$

For the whole system, p represents parameter(s), $u(t) \in \mathcal{R}^l$ is the input vector and $y(p) \in \mathcal{R}^m$ is the output vector. In the electrical part (27a) governed by algebraic equations, $A_{\mathsf{E}}(p) \in \mathcal{R}^{n_{\mathsf{E}} \times n_{\mathsf{E}}}$ is the system matrix, $B_{\mathsf{E}}(p) \in \mathcal{R}^{n_{\mathsf{E}} \times l}$ is the input matrix and $x_{\mathsf{E}} \in \mathcal{R}^{n_{\mathsf{E}}}$ is the state vector. In the thermal part (27b) governed by ordinary differential equations, $B_{\mathsf{T}}(p) \in \mathcal{R}^{n_{\mathsf{T}} \times l}$ is the input matrix, $x_{\mathsf{T}}(p) \in \mathcal{R}^{n_{\mathsf{T}}}$ is the state vector, $A_{\mathsf{T}}(p), E_{\mathsf{T}}(p) \in \mathcal{R}^{n_{\mathsf{T}} \times n_{\mathsf{T}}}$ are system matrices. The tensor $F(p) \in \mathcal{R}^{n_{\mathsf{T}} \times n_{\mathsf{E}} \times n_{\mathsf{E}}}$, which can

be considered as n_T slices of n_E by n_E matrices $F_i(p) \in \mathcal{R}^{n_\mathsf{E} \times n_\mathsf{E}}$, $i = 1, \ldots, n_T$, represents the nonlinear coupling from the electrical part to the thermal part. Denoting the j-mode tensor-matrix product by $\times_j$, the product $F(p) \times_2 x_\mathsf{E}(p) \times_3 x_\mathsf{E}(p)$ is a vector of length n_T, whose i-th component is the standard vector-matrix-vector product $x_\mathsf{E}(p)^\top F_i(p) x_\mathsf{E}(p)$. In the output part (27d), $D \in \mathcal{R}^{m \times l}$ represents the feedthrough, and $C_\mathsf{E}(p) \in \mathcal{R}^{m \times n_\mathsf{E}}$ and $C_\mathsf{T}(p) \in \mathcal{R}^{m \times n_\mathsf{T}}$ represent the output matrices corresponding to the electrical part and the thermal part, respectively. In this formulation, some weak factors are ignored, e.g., the Joule self heating related to the input variables and the dependence of the electrical and thermal conductivity on the temperature. First, Joule self-heating should theoretically be modeled by two tensor products: $F(p) \times_2 x_\mathsf{E}(p) \times_3 x_\mathsf{E}(p)$ and $G(p) \times_2 x_\mathsf{E}(p) \times_3 u(t)$. The G part describes the nonlinear coupling corresponding to the boundary and the inner field, while the F part describes the coupling corresponding only to the inner field. Since the influence of the G part is rather limited, only the F part is considered in our formulation. In addition, besides the Joule self-heating, the temperature change also results in coupling since both the electrical and the thermal conductivity varies with temperature. This effect is also ignored as it is dominated by Joule self heating. Due to the two simplifications above, system (27b) has a one-way coupling from the electrical part to the thermal part through the tensor $F(p)$, and the coupling the other way round is ignored. Instead of a single coupled system, we write out the electrical and the thermal sub-systems explicitly not only to show the one-way coupling, but also emphasize the fact that applying pMOR to the electrical part and the thermal part separately is much more efficient than applying pMOR to the single coupled system, which we observed in our numerical tests.

In our numerical tests, p represents a single parameter σ, the conductivity of the third metal layer. Therefore, all parametric matrices in system (27) take the form

$$Y(p) = Y_\mathsf{c} + pY_\mathsf{v}, \qquad Y \in \{A_\mathsf{E}, A_\mathsf{T}, B_\mathsf{E}, B_\mathsf{T}, C_\mathsf{E}, C_\mathsf{T}, D, E_\mathsf{T}, F\}, \tag{28}$$

because the finite-integration technique (FIT) assembles fluxes that are proportional to the conductivity of each mesh cell material.

4.2 PMOR based on multi-moment-matching

The multi-moment-matching methods are arguably the most computationally efficient for many applications, especially for linear systems of the form

$$\begin{aligned} E(p)\tfrac{dx(t,p)}{dt} &= A(p)x(t,p) + B(p)u(t), \\ y(t,p) &= C(p)x(t,p) + D(p)u(t), \end{aligned} \tag{29}$$

where only $E(p), A(p) \in \mathbb{R}^{n \times n}$, $B(p) \in \mathbb{R}^{n \times l_\mathsf{I}}$, $C(p) \in \mathbb{R}^{l_\mathsf{O} \times n}$, and $D(p) \in \mathbb{R}^{l_\mathsf{O} \times l_\mathsf{I}}$. The multi-moment-matching PMOR method computes a basis matrix V based on the series expansion of the state vector x in the frequency domain. Under the zero initial condition, the frequency domain description for system (29) is

$$\begin{aligned} (sE(p) - A(p))x(s,p) &= B(p)u(s), \\ y(s,p) &= C(p)x(s,p) + D(p)u(s), \end{aligned} \tag{30}$$

where we assume that the matrix pencil $(A(p), E(p))$ is regular for any p value, i.e., there exists $\lambda_{p,0}$ such that $\lambda_{p,0}E(p) - A(p)$ is nonsingular. In this section, we assume

that $A(p)$, $B(p)$, $C(p)$, $D(p)$ and $E(p)$ all take the affine form

$$M(p) = p_1 M_1 + \ldots + p_m M_m. \tag{31}$$

Given expansion points $p^0 = [p_1^0, \ldots, p_m^0]$, and s_0, $x(s,p)$ in (30) can be expanded as

$$\begin{aligned} x(s,p) &= [I - (\sigma_1 G_1 + \ldots + \sigma_m G_m + \sigma_{m+1} G_{m+1} + \ldots + \sigma_{2m} G_{2m})]^{-1} B_M u(s) \\ &= \sum_{i=0}^{\infty} (\sigma_1 G_1 + \ldots + \sigma_{2m} G_{2m})^i B_M u(s), \end{aligned} \tag{32}$$

where $\sigma_i = s p_i - s_0 p_i^0$, $\sigma_{m+i} = p_i - p_i^0$, $G_i = -[s_0 E(p^0) - A(p^0)]^{-1} E_i$, $G_{m+i} = [s_0 E(p^0) - A(p^0)]^{-1} A_i$, $i = 1, 2, \ldots, m$, and $B_M = [s_0 E(p^0) - A(p^0)]^{-1} B(p)$, under the condition that all matrices in $[\cdot]^{-1}$ are nonsingular and

$$\|\sigma_1 G_1 + \ldots + \sigma_{2m} G_{2m}\| < 1. \tag{33}$$

Because of condition (33), the resulting ROM is normally accurate only around the expansion point p^0. To obtain a parametric ROM valid on a wider range, multiple expansion points are often employed as we will show below.

Defining

$$R_j = [G_1, \ldots, G_p] R_{j-1}, \qquad j = 1, \ldots, q,$$

and

$$R_0 = [s_0 E(p^0) - A(p^0)]^{-1} [B_1, \ldots, B_m],$$

where $B_1, \ldots B_m$ are derived from (31), we can compute the matrix $V_{s_0,p^0,q}$, whose columns form an orthonormal basis of the subspace spanned by the first q of R_i's [33]:

$$\text{range}\{V_{s_0,p^0,q}\} = \text{span}\{R_0, R_1, \ldots, R_q\}_{s_0,p^0}. \tag{34}$$

Using $V := V_{s_0,p^0,q}$, which is assumed to be an $n \times k$ matrix, we obtain the parametric reduced-order model via Galerkin projection,

$$\begin{array}{rcl} \left(V^\top E(p) V\right) \frac{dx_r(t,p)}{dt} & = & \left(V^\top A(p) V\right) x_r(t,p) + \left(V^\top B(p)\right) u(t), \\ y_r(t,p) & = & (C(p)V)\, x_r(t,p) + D(p) u(t), \end{array} \tag{35}$$

where the state vector $x_r(t,p)$ is of order k. When $A(p)$, $B(p)$, $C(p)$ and $E(p)$ all take the affine form (31), the reduced parametric matrices can be computed by the formulae

$$\begin{aligned} V^\top E(p) V &= p_1 V^\top E_1 V + \ldots + p_m V^\top E_m V, \\ V^\top A(p) V &= p_1 V^\top A_1 V + \ldots + p_m V^\top A_m V, \\ V^\top B(p) &= p_1 V^\top B_1 + \ldots + p_m V^\top B_m, \\ C(p) V &= p_1 C_1 V + \ldots + p_m C_m V, \end{aligned}$$

where all constant matrices on the right-hand side can be pre-computed.

Note that the number of columns in R_j increases exponentially with j. When the number of the parameters in p is larger than 2, or when there are many inputs, multiple expansion points should be used to keep the size of the reduced-order model reasonable. The idea is straightforward. Given a set of expansion points $(s_i, p^i), (i = 0, \ldots, j)$,

where the superscript i for p indicates the i-th expansion point rather than a power, a matrix V_{s_i,p^i} can be computed for each pair (s_i, p^i) as

$$\text{range}\{V_{s_i,p^i,q_r}\} = \text{span}\{R_0, R_1, \ldots, R_{q_r}\}_{s_i,p^i}. \tag{36}$$

The final projection matrix V is obtained from the orthogonalization of all matrices V_{s_i,p^i,q_r},

$$V = \text{orth}\{V_{s_0,p^0,q_r}, \ldots, V_{s_j,p^j,q_r}\}. \tag{37}$$

For similar accuracy, the number q_r in (36) can usually be taken much smaller than q in (34) and normally, only a few well-chosen expansion points suffice. For example, 1 or 2 commonly suffices for q_r, while q must be taken a much larger value depending on the problem. The reason is that, using multiple expansion points, the difficulty of the parametric dependence can be tackled by adding new interpolation points, each of which adds only a few columns due to the small q_r, which is much more economical than using a single expansion point, where this difficulty must be treated with the increase of q, each step of which becomes increasingly more expensive. Consequently, the reduced-order model is normally smaller and more accurate on a broader parameter range when multiple expansion points are used.

The choice of the numbers and locations of the expansion points (s_i, p^i) has an important influence on the efficiency of multi-moment-matching PMOR methods. Actually, good accuracy and compactness of the reduced-order model can only be achieved when the expansion points are selected judiciously.

In the next section, we introduce a technique for adaptively selecting the expansion points according to an *a posteriori* error bound $\Delta(s, p)$ for the ROM. By using the error bound to access the reliability of the reduced-order model, we develop an automatic procedure for constructing the ROM.

4.3 Adaptively selecting the expansion points

For the general system (29) with l_I inputs and l_O outputs, the error bound $\Delta(s, p)$ is defined as

$$\Delta(s, p) = \max_{\substack{1\le i\le l_\text{I},\\ 1\le j\le l_\text{O}}} \Delta_{ij}(s, p),$$

where $\Delta_{ij}(s, p)$ is the error bound for the (i, j)-th entry of the transfer function matrix of the ROM, i.e.,

$$|H_{ij}(s, p) - \hat{H}_{ij}(s, p)| \le \Delta_{ij}(s, p),$$

where $H(s, p)$ and $\hat{H}(s, p)$ represent the transfer functions of the full-order model and the reduced-order model, respectively. In this section, we define the $\Delta_{ij}(s, p)$ as in [32, 33], which is inspired by the *a posteriori* error bounds proposed for the reduced basis method:

$$\Delta_{ij}(s, p) = \frac{||r_i^{du}(s, p)||_2 ||r_j^{pr}(s, p)||_2}{\beta(s, p)} + |(\hat{x}^{du})^* r_j^{pr}(s, p)|,$$

where

$$\begin{aligned} r_j^{pr}(s, p) &= B(:, j) - [sE - A]\hat{x}_j^{pr}, \\ \hat{x}_j^{pr} &= V(sV^\top EV - V^\top AV)^{-1} V^\top B(:, j), \\ r_i^{du}(s, p) &= -C(i, :)^\top - [\bar{s}E^\top - A^\top]\hat{x}_i^{du}, \end{aligned}$$

$\bar{s}$ is the conjugate of s, and the state x_i^{du} of the dual system is approximated by

$$\hat{x}_i^{du} = -V^{du}(\bar{s}(V^{du})^\top E^\top V^{du} - (V^{du})^\top A^\top V^{du})^{-1}(V^{du})^\top C(i,:)^\top.$$

Here, for ease of notation, p is dropped from the matrices $E(p), A(p), B(p)$ and $C(p)$, and the j-th column of $B(p)$ and the i-th row of $C(p)$ are denoted by $B(;,j)$ and $C(i,:)$, respectively. The variable $\beta(s,p)$ is the smallest singular value of the matrix $sE(p) - A(p)$. The matrix V^{du} can be computed, for example, using (36) and (37), but replacing $R_0, \ldots, R_{q_r}$ with $R_0^{du}, R_1^{du}, \ldots, R_{q_r}^{du}$, where the matrices $s_i E(p^i) - A(p^i)$ in $R_0, \ldots, R_{q_r}$ are substituted by $\bar{s}_i E^\top(p^i) - A^\top(p^i)$, and E_j by $E_j^\top$, A_j by $A_j^\top$, $B(:,j)$ by $C(j,:)^\top$, $j = 1, \ldots, m$. The derivation of $\Delta(s,p)$ is detailed in [32].

Algorithm 1 Adaptively selecting expansion points $\hat{s}$, $\hat{p}$, and computing V automatically [32, 33]

1: $V = []; V^{du} = []$;
2: Choose some $\varepsilon_{tol} < 1$ and a small positive integer q_r; set $\varepsilon = 1$;
3: Choose Ξ_{train}: a large set of samples of s and p, taken over the domain of interest;
4: Choose the initial expansion point: $(\hat{s}, \hat{p})$;
5: **while** $\varepsilon > \varepsilon_{tol}$ **do**
6: $\quad \mathrm{range}(V_{\hat{s},\hat{p},q_r}) = \mathrm{span}\{R_0, R_1, \ldots, R_{q_r}\}_{\hat{s},\hat{p}}$;
7: $\quad \mathrm{range}(V^{du}_{\hat{s},\hat{p},q_r}) = \mathrm{span}\{R_0^{du}, R_1^{du}, \ldots, R_{q_r}^{du}\}_{\hat{s},\hat{p}}$;
8: $\quad V = \mathrm{orth}\{V, V_{\hat{s},\hat{p},q_r}\}$;
9: $\quad V^{du} = \mathrm{orth}\{V^{du}, V^{du}_{\hat{s},\hat{p},q_r}\}$;
10: $\quad (\hat{s}, \hat{p}) = \arg \max_{s,p \in \Xi_{train}} \Delta(s,p)$;
11: $\quad \varepsilon = \Delta(\hat{s}, \hat{p})$;
12: **end while**.

Thanks to the error bound $\Delta(s,p)$ for the ROM, the expansion points (s_i, p^i) can be selected adaptively, and the projection matrix V can be computed automatically as is shown in Algorithm 1. It is worth pointing out that although the error bound is parameter-dependent, many p-independent terms constituting the error bound need to be pre-computed only once, which can be repeatedly used in the algorithm for all samples of p in Ξ_{train}, e.g., the terms $V^\top M_1 V, \ldots, V^\top M_m V$, etc.

4.4 Parametric MOR of the Power-MOS model

Following the idea of quadratic Krylov-type MOR, we first ignore the nonlinear part $F(p) \times_2 x_{\mathsf{E}}(p) \times_3 x_{\mathsf{E}}(p)$ in system (27b) and use the adaptive PMOR algorithm proposed to reduce the resulting system in the form (29). To approximate the one-way coupling term, we need to reduce the electrical sub-system before reducing the thermal sub-system [85].

- The electrical sub-system (27a) is already in the form (30) if we assign $E(p) = 0$, $A(p) = -A_{\mathsf{E}}(p)$, $B(p) = -B_{\mathsf{E}}(p)$, $s = t$, by noting that for the validity of the proposed PMOR method, system (30) is actually not necessarily a frequency-domain system. We denote the basis built for the electrical sub-system (27a) by V_{E}.
- If we ignore the nonlinear coupling term in the thermal sub-system (27b), it is already in the form (29). To use the methods developed, we first conduct the

Laplace transform to obtain its frequency domain representation

$$(A_{\mathsf{T}1} + \sigma A_{\mathsf{T}2} - sE_{\mathsf{T}1} - (\sigma s)E_{\mathsf{T}2})X = [B_{\mathsf{T}1} \;\; B_{\mathsf{T}2} \;\; A_{\mathsf{T}1}x_{\mathsf{T}}^0 \;\; A_{\mathsf{T}2}x_{\mathsf{T}}^0] \begin{bmatrix} -U \\ -\sigma U \\ \frac{-1}{s} \\ \frac{-\sigma}{s} \end{bmatrix}. \quad (38)$$

Then, we apply Algorithm 1 to system (38) to obtain the basis for the thermal sub-system, which we denote by V_{T}.

- To obtain a ROM for (27b), we approximate x_{E} by $V_{\mathsf{E}}\widehat{x}_{\mathsf{E}}$ and x_{T} by $V_{\mathsf{T}}\widehat{x}_{\mathsf{T}}$, and then force the approximation error to be orthogonal to the range of V_{T}. The resulting parametric ROM is

$$\widehat{E}_{\mathsf{T}}(p)\dot{\widehat{x}}_{\mathsf{T}}(t,p) = \widehat{A}_{\mathsf{T}}(p)\widehat{x}_{\mathsf{T}}(t,p) + \widehat{B}_{\mathsf{T}}(p)u + \widehat{F}(p) \times_2 \widehat{x}_{\mathsf{E}}(p) \times_3 \widehat{x}_{\mathsf{E}}(p), \quad (39)$$

where $\widehat{E}_{\mathsf{T}}(p) = V_{\mathsf{T}}^\top E_{\mathsf{T}}(p)V_{\mathsf{T}}$, $\widehat{A}_{\mathsf{T}}(p) = V_{\mathsf{T}}^\top A_{\mathsf{T}}(p)V_{\mathsf{T}}$, $\widehat{B}_{\mathsf{T}}(p) = V_{\mathsf{T}}^\top B_{\mathsf{T}}(p)$, $\widehat{F}(p) = F(p) \times_1 V_{\mathsf{T}} \times_2 V_{\mathsf{E}} \times_3 V_{\mathsf{E}}$, which has r_{T} slices of $r_{\mathsf{E}} \times r_{\mathsf{E}}$ matrices with its j-th slice $\sum_{i=1}^{n_T} V_{\mathsf{T}}(i,j)V_{\mathsf{E}}^\top F(i,:,:)(p)V_{\mathsf{E}}$, where r_{E} and r_{T} are the number of columns of V_{E} and V_{T}, respectively. To obtain the reduced tensor $\widehat{F}(p)$, we first approximate $x_{\mathsf{E}}(p)$ in the range of V_{E}, and then project the approximation onto the test subspace V_{T}, i.e., the tensor product $\widehat{F}(p)\times_2\widehat{x}_{\mathsf{E}}(p)\times_3\widehat{x}_{\mathsf{E}}(p)$ equals $V_{\mathsf{T}}^\top [F(p) \times_2 (V_{\mathsf{E}}\widehat{x}_{\mathsf{E}}(p)) \times_3 (V_{\mathsf{E}}\widehat{x}_{\mathsf{E}}(p))]$. The advantage of the tensor formulation for the ROM is that using the reduced tensor, evaluating the ROM does not require computations with quantities of the order of the FOM. In our actual computations, the parametric matrices in the ROM are computed by

$$\widehat{Y}(p) = \widehat{Y}_{\mathsf{c}} + p\widehat{Y}_{\mathsf{v}}, \qquad \widehat{Y} \in \{\widehat{A}_{\mathsf{T}}, \widehat{B}_{\mathsf{T}}, \widehat{C}_{\mathsf{T}}, \widehat{E}_{\mathsf{T}}, \widehat{F}\}, \quad (40)$$

where $\widehat{Y}_{\mathsf{c}}$ and $\widehat{Y}_{\mathsf{v}}$ are pre-computed during the construction of the ROM. This pre-computation is also applied to the electrical sub-system (27a) and the output computation (27d).

4.5 PMOR-based UQ

As was reviewed in Section 2, UQ methods can be categorized into non-intrusive methods and intrusive methods. In this section, we focus on non-intrusive methods since the pROM of the original deterministic model (FOM) can be directly used to replace the FOM in UQ. We embed our pROMs into two UQ methods, namely the Latin Hypercube Sampling (LHS) method and the Stochastic Collocation (SC) method [21].

- LHS. To obtain n samples, LHS divides the input distribution into n intervals of equal probability, and selects one sample randomly in each interval. The mean and standard deviation of the samples are used to approximate those of the original continuous model. Compared to the standard Monte-Carlo sampling, LHS ensures a set of evenly distributed samples.

- SC descried in Section 2.4.2. Since the mean and the standard deviation can be computed via numerical integration, SC uses a quadrature rule to present the relevant integrals as a weighted sum of the corresponding function values at the collocation points. As we conduct UQ on a single normally-distributed random variable, we use the Gauss-Hermite quadrature rule.

The computationally dominant part of both LHS and SC is the simulation of the high-order FOM at all sampled points p_i. Since our pROMs are highly accurate for these simulations, pROM-based UQ replaces the FOM (27) with pROMs for these simulations to achieve a significant speedup.

4.6 Numerical results

In this section, we test the effectiveness and efficiency of pROM-based UQ [85]. All codes are implemented in MATLAB®. For the SC method, we use the SGMGA library to compute the quadrature rule.

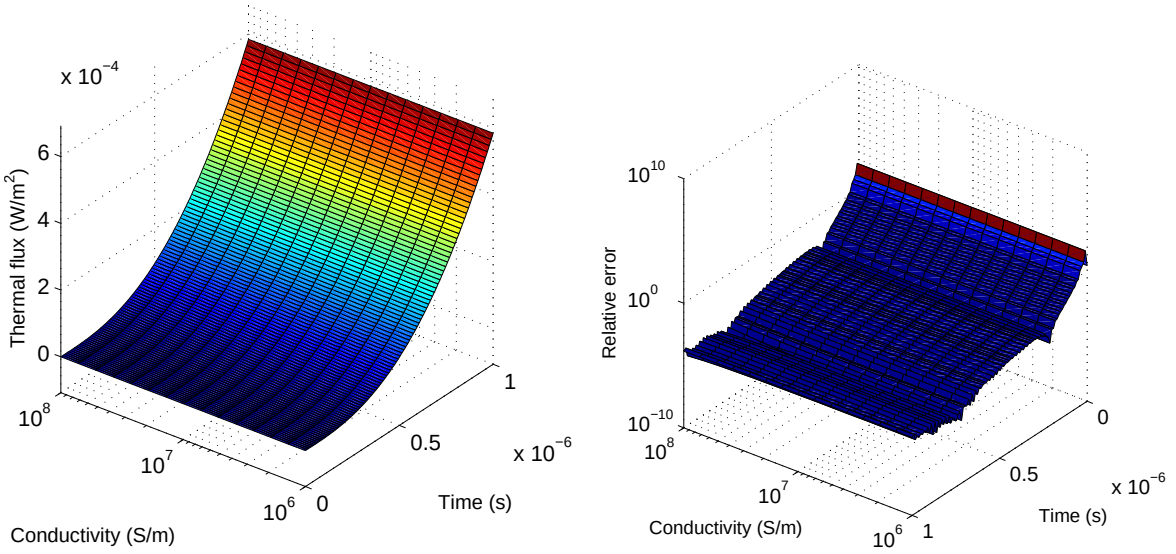

(a) Thermal flux on drain computed by the full-order model

(b) Relative error of the thermal flux on drain

Figure 32: Evolution of the relative errors of the thermal outputs for extreme σ's at $t = 10^{-6}$ s [85].

First, we check the quality of the pROMs in a simulation analysis. For (27), we build an order-2 pROM for the order-1660 FOM of the electrical part (27a), and an order-30 pROM for the order-11556 FOM of the thermal part (27b). Figure 32 shows that the relative error for thermal fluxes for the drain. When the system starts, the relative errors are high because: 1) the thermal fluxes are close to zero since the system is hardly heated up; 2) the thermal outputs are dominated by modeling error and numerical error at the starting stage: the outputs of the full-order model also oscillate slightly around zero even when the temperature is the same everywhere and no voltage excitation is imposed. However, as time elapses, the relative errors decrease to the order of 10^{-4} and therefore, the dominant dynamics are accurately captured over a large parameter range.

Now we apply the pROMs to UQ analysis of the electro-thermal system (27). Here we conduct UQ on the outputs at $t = 10^{-6}$ s. We assume that the conductivity obeys the normal distribution $\mathcal{N}(3 \times 10^7, (10^7)^2)$. The numerical results in Table 5 show that for both UQ methods, pROM-based UQ computes highly accurate means ($E(\cdot)$). For the nontrivial electrical outputs I_{drain} and I_{source}, which are sensitive to the change in the conductivity with the same coefficient of variation (CV) of 33.23%, the standard deviations ($\sigma(\cdot)$) are also computed with high accuracy. The thermal outputs ϕ_{drain}, ϕ_{source} and ϕ_{back}, however, are insensitive to the change in the conductivity with CV's of 3.77e-07, 4.4138e-07 and 2.3483e-08, respectively. Although the standard deviations to these insensitive thermal outputs are not of so high accuracy, the relative orders are correct: actually Table 5 shows that even different FOM-based methods provide different results with a comparable deviation.

Table 5: UQ results for the outputs at $t = 10^{-6}$ s [85].

	LHS (FOM)	LHS (ROM)	SC (FOM)	SC (ROM)
$E(I_{\text{drain}})$	7.4621e-04	7.4621e-04	7.4602e-04	7.4602e-04
$\sigma(I_{\text{drain}})$	2.4794e-04	2.4794e-04	2.4867e-04	2.4867e-04
$E(I_{\text{source}})$	-7.4621e-04	-7.4621e-04	-7.4602e-04	-7.4602e-04
$\sigma(I_{\text{source}})$	2.4794e-04	2.4794e-04	2.4867e-04	2.4867e-04
$E(I_{\text{back}})$	0	0	0	0
$\sigma(I_{\text{back}})$	0	0	0	0
$E(\phi_{\text{drain}})$	5.8479e-04	5.8478e-04	5.8479e-04	5.8479e-04
$\sigma(\phi_{\text{drain}})$	1.5838e-10	1.5677e-10	1.5985e-10	1.5719e-10
$E(\phi_{\text{source}})$	4.1977e-04	4.1975e-04	4.1977e-04	4.1977e-04
$\sigma(\phi_{\text{source}})$	1.8528e-10	9.1986e-11	4.6370e-11	9.2124e-11
$E(\phi_{\text{back}})$	6.6781e-07	6.6773e-07	6.6781e-07	6.6781e-07
$\sigma(\phi_{\text{back}})$	1.5682e-14	1.7778e-14	1.1199e-14	1.6189e-14
Number of samples	100	100	11	11
CPU time	6001.14 s	94.19 s	733.64 s	30.51 s

In conclusion, the numerical results shows that the proposed PMOR-based UQ framework provides accurate results and significant speedups.

5 Polynomial Chaos and reduced models in co-simulation

A specific approach, which allows for some adaptivity of discretizations in the random space, was constructed in the project. This topic corresponds to Task T2.4.

5.1 Motivation of the problem

In nanoelectronics, multiphysics problems appear characterized by the coupling of different effects like electromagnetics, heat transport, mechanical deformation and quantum mechanics, for example. Hence the mathematical model consists of two or more parts, which are interconnected by a few coupling variables. On the one hand, the coupled system can be solved by a transient analysis of the set of all involved equations, which is called a holistic simulation or a monolithic time integration. On the other hand, often a dynamic iteration, see [15, 71, 34], which is sometimes called co-simulation, is used for a numerical simulation of the coupled system for two reasons. Firstly, the equations of a part of the coupled system may not be available directly and can be evaluated only by calling black-box routines in a software package. Secondly, the dynamic iteration enables to use different time step sizes in the separate parts of the coupled system and thus achieves an efficient simulation in the case of multiscale or multirate behavior.

In this task, we consider multiphysics problems including random variables, where the solution becomes a random process. Statistics of the random process can be obtained by a sampling method or a quadrature technique, where the coupled system is solved for each realization of the random variables. Now the idea is to design a numerical integration scheme based on a dynamic iteration such that also different discretization levels can be applied in the random space. More precisely, different grids for the random parameters can be employed for the separate parts of the coupled system in the quadrature schemes.

5.2 Mathematical formulation of the problem

The description of the dynamic iteration method follows deliverable D2.5 [5, Sect. 2]. The algorithm is formulated for time-dependent coupled problems consisting of two parts, i.e.,

$$\begin{aligned} F_1\left(y_1(t,p), y_2^{\mathrm{cpl}}(t,p), t, p\right) &= 0, \\ F_2\left(y_2(t,p), y_1^{\mathrm{cpl}}(t,p), t, p\right) &= 0, \end{aligned} \tag{41}$$

where independent random variables $p : \Omega \to \Pi \subseteq \mathbb{R}^Q$ are included from some probability space $(\Omega, \mathcal{A}, \mu)$ with event space Ω, sigma-algebra $\mathcal{A}$ and probability measure μ. The operators F_1, F_2 represent systems of ordinary differential equations or differential-algebraic equations typically stemming from the semi-discretization of partial differential equations. Hence time derivatives are involved in each part. The operators F_i comprise n_i equations and the solution of the system (41) is $y_i : [t_0, t_{\mathrm{end}}] \times \Pi \to \mathbb{R}^{N_i}$ for $i = 1, 2$, where initial values are given for all p. The coupling variables are defined as

$y_i^{\mathrm{cpl}} := B_i y_i$ with constant matrices $B_i \in \{0,1\}^{R_i \times N_i}$ such that the coupling variables include just a subset of y_i for each $i = 1, 2$. Typically, it holds that $R_1 \ll N_1$ and $R_2 \ll N_2$, i.e., the coupling variables represent just a small portion of the solution. Furthermore, it is allowed that just one of the two subsystems in (41) includes all the parameters.

To solve the coupled problem (41) for a fixed $p \in \Pi$, we consider a dynamic iteration, where the total time span is split into windows with a first window $[t_0, t_{\mathrm{win}}]$. The resulting iteration of Gauss-Seidel type reads as

$$\begin{aligned} F_1\Big(y_1^{(\nu+1)}(t,p), y_2^{\mathrm{cpl}\,(\nu)}(t,p), t, p\Big) &= 0, \\ F_2\Big(y_2^{(\nu+1)}(t,p), y_1^{\mathrm{cpl}\,(\nu+1)}(t,p), t, p\Big) &= 0, \end{aligned} \qquad \text{for } \nu = 0, 1, 2, \ldots \tag{42}$$

and $t \in [t_0, t_{\mathrm{win}}]$ using the starting values $y_2^{(0)}(t,p) \equiv y_2(t_0, p)$. A numerical method yields the solutions $y_1,\ y_2$ only on a discrete set of time points, which may also differ for the two subsystems. We assume that all coupling variables are interchanged at a few communication time points $\bar{t}_j$ with $t_0 \le \bar{t}_1 < \bar{t}_2 < \cdots < \bar{t}_J = t_{\mathrm{win}}$. Interpolation in time yields approximations of the coupling variables $y_i^{\mathrm{cpl}}(t,p)$ for $t \in [t_0, t_{\mathrm{win}}]$ and $i = 1, 2$.

Statistical information for a function $g : \Pi \to \mathbb{R}$ depending on the random parameters is obtained by probabilistic integrals

$$\mathrm{E}(g) := \int_\Omega g(p(\omega))\ \mathrm{d}\mu(\omega) = \int_\Pi g(p)\,\rho(p)\ \mathrm{d}p, \tag{43}$$

provided that the integral is finite, where the existence of a joint probability density function $\rho : \Pi \to \mathbb{R}$ is assumed. For example, probabilistic integration can be applied to the solution of (41) component-wise. The expected value as well as the variance represent elementary statistics. Our aim is to compute statistics of the solution y_1, y_2 for either the complete time interval or just at a final time.

A quadrature scheme or a sampling method yields an approximation of a probabilistic integral (43), see [84] and the references therein. We obtain a finite sum of the form

$$\mathrm{E}(g) \doteq \sum_{k=1}^{K} w_k g(p^{(k)}),$$

with grid points $p^{(1)}, \ldots, p^{(K)} \in \Pi$ and weights $w_1, \ldots, w_K \in \mathbb{R}$. Still a single grid of parameter values is involved here. For a quantity of interest

$$g(p) = \tilde{g}(y_1(t_{\mathrm{end}}, p), y_2(t_{\mathrm{end}}, p)),$$

at some final time, it follows that an initial value problem of the system (41) has to be resolved K times for the different realizations of the parameters.

5.3 Adjusted grid technique

Now the above strategy is modified to obtain a potential for adjustments in discretizations of the random space.

5.3.1 Definition of the algorithm

We introduce two grids

$$\mathcal{G}_i := \left\{ p_i^{(1)}, \ldots, p_i^{(K_i)} \right\}, \quad \text{with } p_i^{(k)} \in \Pi, \tag{44}$$

for $i = 1, 2$, dedicated to the two parts of the coupled problem (41). The numbers of grid points K_1, K_2 may differ significantly. The subsystem for F_i together with its solution y_i is integrated in time on the grid $\mathcal{G}_i$ for each $i = 1, 2$.

Following (42), we have to solve the problems

$$\begin{aligned} F_1\left(y_1^{(\nu+1)}(t, p_1^{(k)}), y_2^{\mathrm{cpl}\,(\nu)}(t, p_1^{(k)}), t, p_1^{(k)}\right) &= 0 \qquad \text{for } k = 1, \ldots, K_1, \\ F_2\left(y_2^{(\nu+1)}(t, p_2^{(k)}), y_1^{\mathrm{cpl}\,(\nu+1)}(t, p_2^{(k)}), t, p_2^{(k)}\right) &= 0 \qquad \text{for } k = 1, \ldots, K_2, \end{aligned} \tag{45}$$

in each step of the dynamic iteration. The first iteration step $\nu = 0$ in (45) for F_1 can be computed directly using the globally defined initial values. The outputs are $y_1^{(1)}(\bar{t}_j, p_1^{(k)})$ for $k = 1, \ldots, K_1$ in the communication time points $\bar{t}_1, \ldots, \bar{t}_J$ introduced above. To this end, we need the coupling variables $y_1^{\mathrm{cpl}(1)}(\bar{t}_j, p_2^{(k)})$ for $k = 1, \ldots, K_2$ and $j = 1, \ldots, J$. Likewise, the outputs of F_2 are the solutions $y_2^{(1)}(\bar{t}_j, p_2^{(k)})$ for $k = 1, \ldots, K_2$ and $j = 1, \ldots, J$. Thus they have to be transformed into the coupling variables $y_2^{\mathrm{cpl}(1)}(\bar{t}_j, p_1^{(k)})$ for $k = 1, \ldots, K_1$, i.e., the evaluation on the other quadrature grid is required. This strategy repeats in each iteration step. Hence transitions between the two grids have to be defined for a fixed time point.

For the interchange of information between the two grids, we consider global approximations of the coupling variables in the parameter space Π. If a global approximation is available, we can evaluate at any point $p \in \Pi$. There are two techniques to construct a global approximation:

1. *Best-approximation in integral norm*
   Orthogonal basis polynomials are available with respect to the L^2-inner product of the probability space induced by the integral (43). Hence a truncated sum of the polynomial chaos expansion is used, see [84]. Let the time $\bar{t}$ be fixed. The global approximation reads as

   $$\tilde{y}_i^{\mathrm{cpl}}(\bar{t}, p) := \sum_{m=0}^{M_i} u_{i,m}(\bar{t}) \Phi_m(p) \tag{46}$$

   for $i = 1, 2$ with known basis polynomials $\Phi_m : \Pi \to \mathbb{R}$ satisfying the orthonormality condition $\mathrm{E}(\Phi_m \Phi_n) = \delta_{mn}$. In general, all polynomials up to a certain degree are involved. The coefficient functions in (46) are determined approximately by

   $$u_{i,m}(\bar{t}) := \int_\Pi y_i^{\mathrm{cpl}}(\bar{t}, p) \Phi_m(p) \rho(p)\, \mathrm{d}p \doteq \sum_{k=1}^{K_i} w_i^{(k)} y_i^{\mathrm{cpl}}(\bar{t}, p_i^{(k)}) \Phi_m(p_i^{(k)}) \tag{47}$$

   for $i = 1, 2$, where the values $w_i^{(k)} \in \mathbb{R}$ represent the weights of quadrature formulas on the grids $\mathcal{G}_i$. Thus the sums (46) can be evaluated for an arbitrary $p \in \Pi$. This introduces UQ inside the dynamic iteration of the co-simulation in a time integration. Although this strategy is intrusive, the evaluations (46),(47) only require calls to standard procedures in the UQ library.

2. *Interpolation scheme in parameter space*
   The coupling variables are approximated by an interpolating function. For fixed time $\bar{t}$, it holds that

$$\tilde{y}_i^{\mathrm{cpl}}(\bar{t}, p) := \sum_{k=1}^{K_i} \Psi_{i,k}(p) y_i^{\mathrm{cpl}}(\bar{t}, p_i^{(k)}) \tag{48}$$

   for $i = 1, 2$ with the functions $\Psi_{i,k} : \Pi \to \mathbb{R}$ satisfying

$$\Psi_{i,k}(p_i^{(\ell)}) = \begin{cases} 0 & \text{for } k \neq \ell, \\ 1 & \text{for } k = \ell, \end{cases}$$

   which are independent of time. For example, Lagrange polynomials are applicable in the case of uniform grids. Obviously, the approximation coincides with the exact coupling values at the grid points. Again the formula (48) can be evaluated at an arbitrary parameter value.

Since the number of coupling variables is relatively low in comparison to the dimension of the coupled problem, the computational effort for the global approximation is usually negligible compared to the time integration. After the convergence of the dynamic iteration in a time window, the same approach is repeated in the next time window. Therein, initial values can be transformed between the two grids again by the above procedure. If the approximations have been computed at the final time t_{end}, then we reconstruct statistical data by quadrature formulas using the same grid points.

5.3.2 Numerical results for thermal-electric problem

In [55], this numerical method was applied to a thermal-electric circuit problem introduced by [16], where the differential algebraic equations of a circuit and the one-dimensional partial differential equation of the heat transport are coupled. Random variables are included in both subsystems. Figure 33 and Figure 34 depict the resulting statistics (expected value and standard deviation) of the crucial quantities in the circuit part and the thermal part, respectively. Therein, the space domain is standardized to the unit interval. Deliverable D2.4 [4, Sect. 3.1] also includes these numerical results.

5.4 Inclusion of Model Order Reduction

The dynamic iteration decouples the multiphysics problems to an extend that also model order reduction can be applied in some subsystem.

5.4.1 Substitution of subsystem models

If the solutions of the subsystems in the coupled problem (41) behave differently with respect to the random parameters, then the application of different quadrature formulas might become advantageous. Firstly, a higher variance within a subsystem often indicates that a higher accuracy of the quadrature is required. Secondly, a ROM can allow

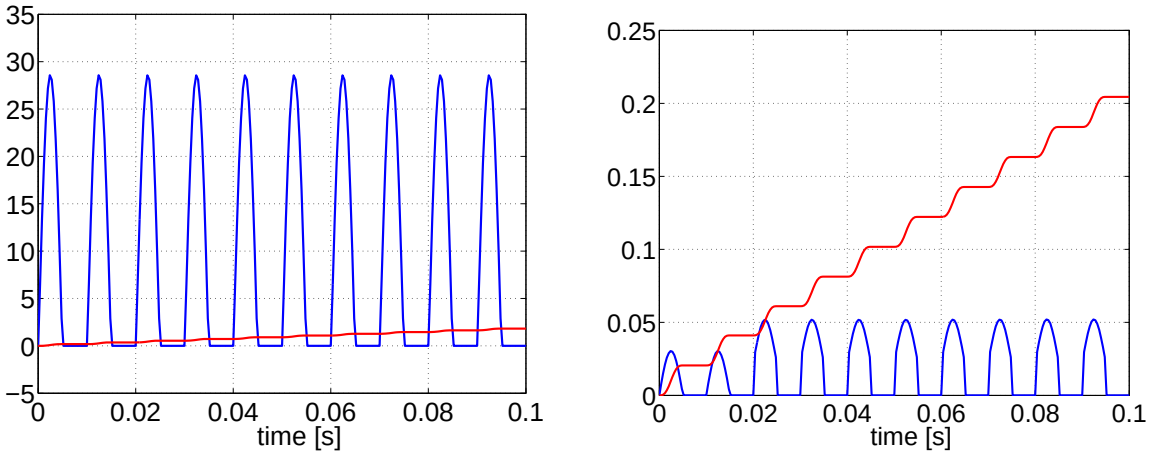

(a) expected values (b) standard deviations

Figure 33: Expected values (a) and standard deviations (b) of the output current [V] (blue) and of the dissipated energy [J] (red) in the circuit part of the heat-circuit problem [55].

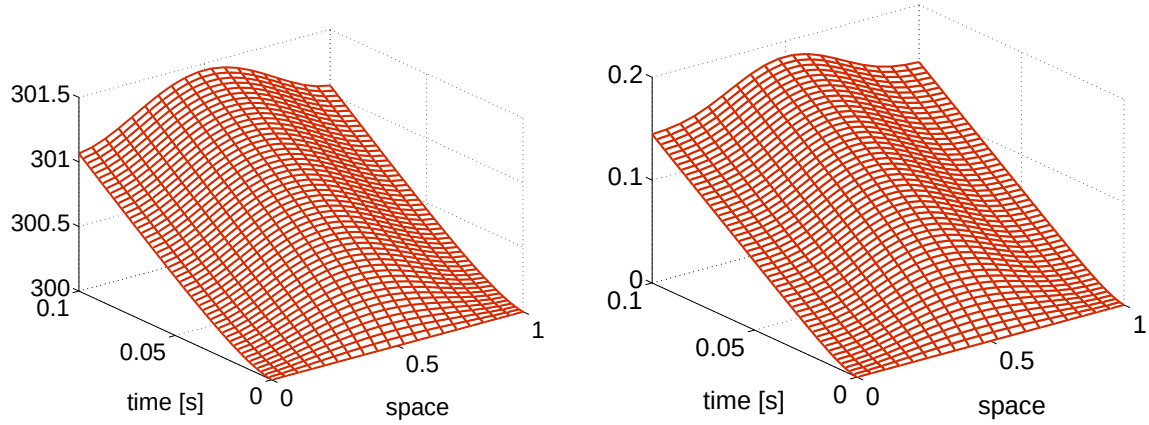

(a) expected values (b) standard deviations

Figure 34: Expected values (a) and standard deviations (b) of the temperature [K] in the thermal part of the heat-circuit problem [55].

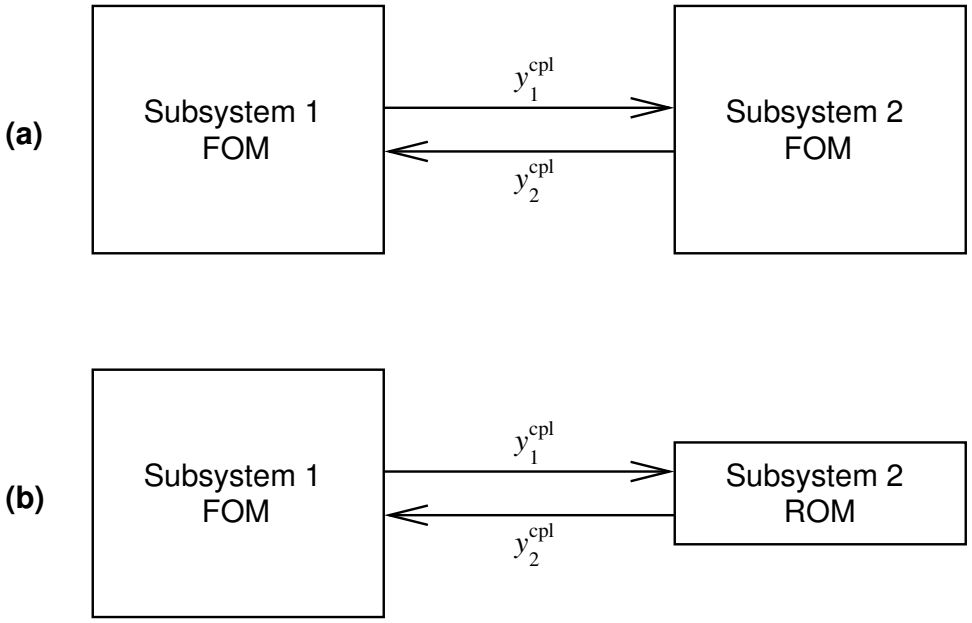

Figure 35: Original setting with full order models (a) and with inclusion of a reduced order model (b) [5].

for a much finer quadrature grid, since its evaluation requires just a low computational effort. Figure 35 illustrates the inclusion of an ROM. If sufficiently accurate ROMs are available for both subsystems, then even the complete system may be sampled on a fine grid with a low computational effort, which is in the context of parameterized MOR as discussed in Section 4. Thus the usage of different quadrature grids is mainly relevant only if one of the subsystems cannot be replaced by an ROM and thus its full order model (FOM) must be used.

5.4.2 Numerical results for field-circuit problem

For the dynamic iteration including a ROM, we investigate the multiphysics field-circuit problem shown in Figure 24. Random variables are introduced in both parts of the coupled problem. The electromagnetic part is replaced by an ROM now. Figure 36 illustrates the expected value and the standard deviation of the output voltage computed by the dynamic iteration including the ROM, as well as a reference solution using the FOM within a monolithic time integration. The associated differences between the statistics of the output voltages produced by the two numerical approaches are depicted in Figure 37. More details can be found in deliverable D2.5 [5, Sect. 3].

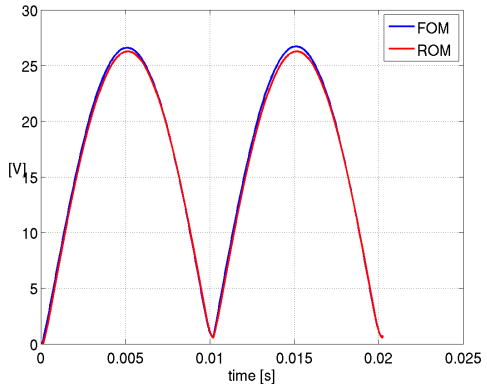

(a) expected values

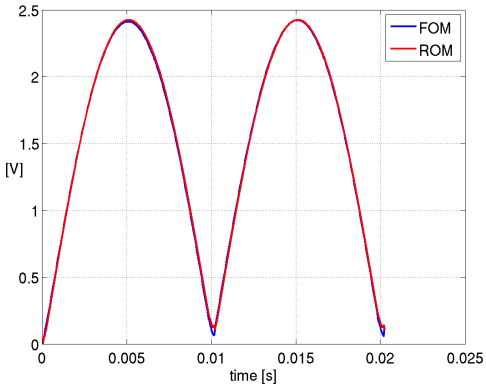

(b) standard deviations

Figure 36: Statistics of the output voltage computed by the full order model (FOM) variant and by the reduced order model (ROM) variant in field-circuit problem [5].

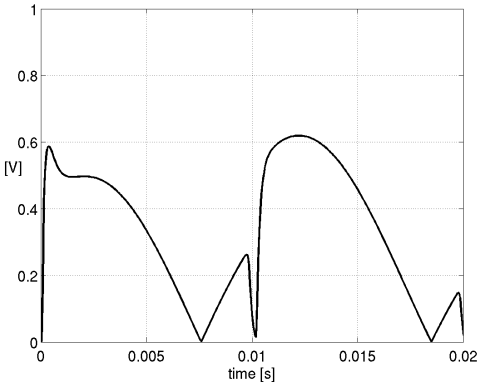

(a) expected values

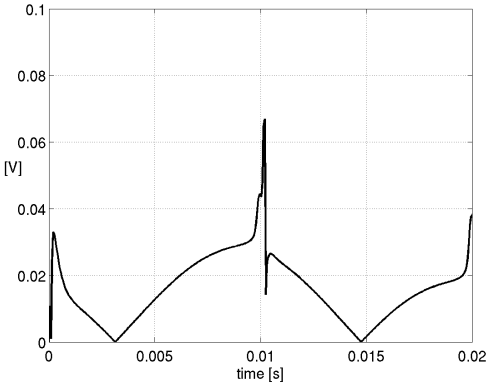

(b) standard deviations

Figure 37: Modulus of the difference between the full order model (FOM) variant and the reduced order model (ROM) variant for the statistics of the output voltage in the field-circuit problem [5].

6 Small failure probabilities and ageing

This part of the project refers to the concepts of variability and reliability for technical components. The topic corresponds to Task T2.6.

6.1 Motivation of failure analysis

The determination of failure probabilities and the detection of faults was considered to address the reliability of electronic devices in view of undesired variations in an industrial production. Assuming that most of the produced devices exhibit a good or acceptable functionality, only a small number of devices have to be rejected. Thus a numerical simulation shall determine small failure probabilities to confirm that an industrial production is acceptable and efficient. A strong criterion is the six sigma (6σ) concept, where variations of six standard deviations under the assumption of a normal distribution for an input parameter still results in acceptable outputs. The associated failure probability is below 0.00034% and thus tiny.

In a circuit or a device, a source of failures and faults are imperfections in an industrial production. The miniaturization and down-scaling makes a precise manufacturing more difficult. An example for faults within a production are undesired bridges between conducting lines, which should be isolated from each other in the regular case. Figure 38 shows pictures of bridges provided by the industrial partner NXP. If bridges appear in an electronic circuit, it has to be determined whether the overall performance is still acceptable or the component fails.

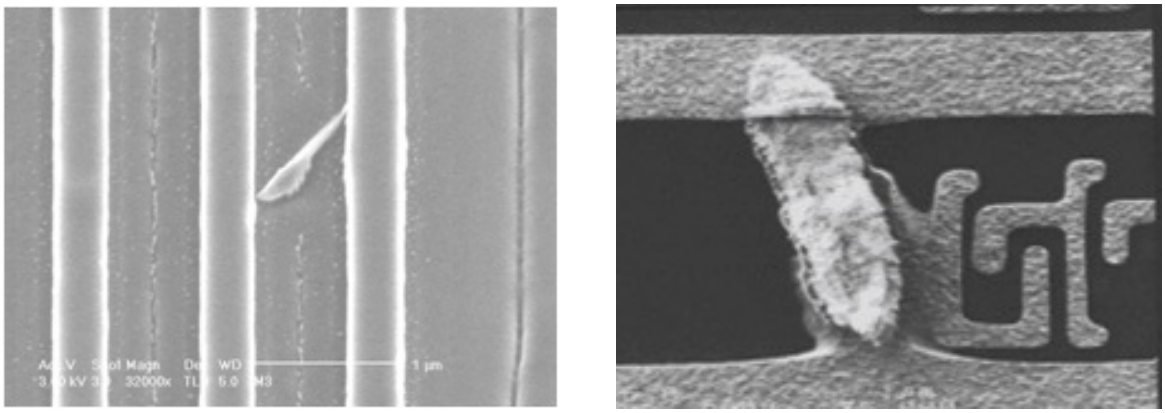

Figure 38: Bridges as imperfections in the manufacturing process (figures from NXP [81]).

6.2 Mathematical formulation

The mathematical formulation of a failure probability is as follows. Let $y \in \Gamma \subseteq \mathbb{R}^{n_y}$ be the state variables of a mathematical model like ordinary differential equations or partial differential equations, for example. The failure of the system is described by a function

$$g : \Gamma \to \mathbb{R} \qquad \text{with} \qquad \begin{array}{ll} g(y) \geq 0 & \text{for acceptable,} \\ g(y) < 0 & \text{for failure.} \end{array} \tag{49}$$

Due to (49), the region of failure becomes $\Gamma_{\mathrm{F}} = \{y \in \Gamma : g(y) < 0\}$. To quantify uncertainties, random variables are introduced as inputs to the mathematical model. Thus the state variables as an output become random variables $Y : \Omega \to \Gamma$ defined on some probability space $(\Omega, \mathcal{A}, \mu)$ with event space Ω, sigma-algebra $\mathcal{A}$ and probability measure μ. Under the assumption that a probability density function $\rho : \Gamma \to \mathbb{R}$ of the random variables is available, the failure probability reads as

$$P_{\mathrm{F}} = \int_{\Omega} \chi_{\Gamma_{\mathrm{F}}}(Y(\omega)) \, \mathrm{d}\mu(\omega) = \int_{\Gamma} \chi_{\Gamma_{\mathrm{F}}}(y)\rho(y) \, \mathrm{d}y. \tag{50}$$

Therein, the characteristic function is defined by

$$\chi_A(y) := \begin{cases} 1 & \text{for } y \in A, \\ 0 & \text{for } y \notin A, \end{cases}$$

for an arbitrary subset $A \subseteq \Gamma$. Each evaluation of the integrand in (50) requires to solve the model equations.

6.3 Hybrid technique

A straightforward numerical technique for the computation of failure probabilities is the Monte-Carlo simulation. The approximation of (50) reads as

$$P_{\mathrm{F}} = \frac{1}{M} \sum_{i=1}^{M} \chi_A(y^i) \tag{51}$$

with $A = \Gamma_{\mathrm{F}}$ and a set of samples $S_y = \{y^1, \ldots, y^M\}$. For small failure probabilities (50), a rule of thumb is to simulate until 10 failures appear. Hence the total number of samples becomes $M \approx 10/P_{\mathrm{F}}$ on average, which causes a huge number of simulations. Alternatively, surrogate models (also called response surface methods) can be applied, where a complex model function g is substituted by a cheap approximation $\tilde{g}$. The estimate of the failure probability (50) becomes (51) with $A = \widetilde{\Gamma}_{\mathrm{F}} = \{y \in \Gamma : \tilde{g}(y) < 0\}$. However, often the surrogate models produce bad approximations for small failure probabilities.

Li and Xiu [43] designed an hybrid method, where the concepts of full order model valuations and surrogate model evaluations are combined. This technique was applied successfully to academic test examples. An improved variant of this method was constructed in [44]. The crucial idea of this approach is to partition the domain of the parameters using a neighborhood of the boundary of the failure region. Figure 39 sketches this strategy. It holds that

$$\chi_{\Gamma_{\mathrm{F}}^{\gamma}} = \chi_{\{\tilde{g} < -\gamma\}} + \chi_{\{|\tilde{g}| < \gamma\} \cap \{g < 0\}} \tag{52}$$

with some threshold value $\gamma > 0$. The threshold γ is related to the size of the neighborhood. The equality (52) is often fulfilled even for a moderate accuracy of the surrogate model. The error control is derived given a desired tolerance TOL for the approximation of the failure probability P_{F} from (50). The threshold γ has to be chosen as

$$\gamma = \eta \mathrm{TOL}^{-1/p} \qquad \text{with} \qquad \eta = \|g - \tilde{g}\|_{L^p_\rho(\Omega)}.$$

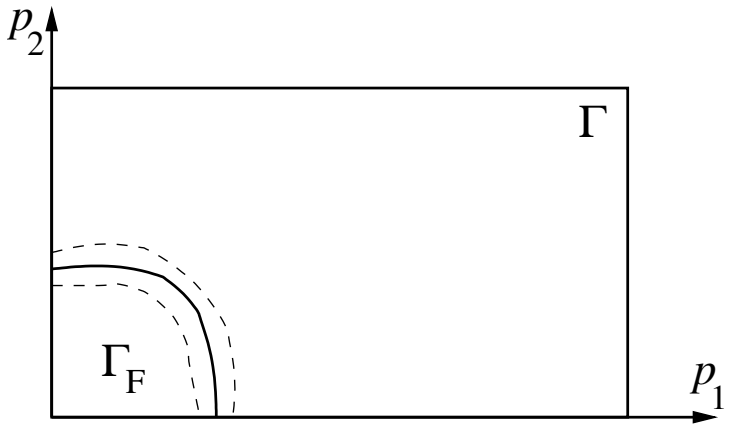

Figure 39: Two-dimensional parameter domain Γ with failure region Γ_F and a neighborhood of the boundary of Γ_F indicated by dashed lines [6, 26].

The hybrid approach was neither known nor used for industrial applications yet. We implemented the method from [43] and thus made it available to the industrial partners in the project. Algorithm 2 describes the technique. More details on the implemented algorithm are given in deliverable D2.6 [6].

Thus the response surface model (or a gPC series expansion) is helpful in detecting the volume for failures. In this volume, a full simulation is applied. Not that these full simulations may also require smaller time stepping and more Newton iterations. Furthermore, the assumption has to be made that libraries (like for circuit devices) still provide accurate compact models.

Algorithm 2 Iterative Failure Probability Algorithm [6, 26]

procedure HYBRID(g, $\tilde{g}$, $M, \delta M, \eta$,S_y)
set $k = 0, M^{(k)} = 0$
evaluate P_F^0 using (51) with $\widetilde{\Gamma}_F$
find permutation π of set $[1 : M]$, such that $\{|\tilde{g}(y^{\pi_i})|\}_{i=1}^{M}$ is ascending
while $k < \lceil M/\delta M \rceil$ **do**
  define $S_z^{(k)} = \pi_{[M_1:M_2]}$, where $M_1 = M^{(k)} + 1, M_2 = M^{(k)} + \delta M$
  evaluate g for each element of $S_z^{(k)}$;
  set $P_F^{(k)} = P_F^{(k-1)} + 1/M \sum_{y^i \in S_z^{(k)}} \left(-\chi_{\widetilde{\Gamma}_F}(y^i) + \chi_{\Gamma_F}(y^i) \right)$
  if $|P_F^{(k)} - P_F^{(k-1)}| \leq \eta$ **then**
    return P_F^k
  end if
  update $k = k + 1$, $M^{(k)} = M^{(k-1)} + \delta M$
end while
return P_F^k
end procedure

6.4 Numerical results for an electro-thermal problem

On domain D and time interval I, we are concerned with a nonlinear electrothermal problem

$$-\nabla \cdot (\sigma(T)\nabla\varphi) = 0, \qquad \text{in } I \times D, \tag{53a}$$

$$\rho c \partial_t T - \nabla \cdot (\lambda(T)\nabla T) = \sigma |\nabla\varphi|^2, \qquad \text{in } I \times D, \tag{53b}$$

endowed with suitable initial and mixed boundary conditions. Bond wires, see Figure 3 (left), are incorporated in (53) using lumped elements after discretization with FEM

$$K_\alpha(y, x_T) = K_\alpha^{\mathrm{FE}}(x_T) + K_\alpha^{\mathrm{lmp}}(y, x_T), \quad \alpha \in \{\lambda, \sigma\}.$$

Therein, K_α^{FE} denotes the standard FE stiffness matrix, K_α^{lmp} includes the lumped bond wire contribution and y are the bond wire lengths as random parameters. With $x = (x_T, x_\varphi)$ we obtain a parametric index-1 differential algebraic equation

$$M\dot{x} + K(y, x)x = q(y, x).$$

Now we apply the hybrid technique outlined in Section 6.3. The failure indicator function (49) reads as

$$g = \int_I f^\top x \, \mathrm{d}t.$$

The surrogate model $\tilde{g}$ is constructed by a stochastic collocation approach based on a tensor product grid or a sparse grid. We solve the adjoint system

$$-M\dot{z} + \overline{K}(y)z = f$$

backward in time to obtain the evaluations in the grid points for the surrogate model. With the stochastic collocation approximation $\tilde{z}$, we obtain

$$\eta = \left\| \int_I \tilde{z} \cdot (q(\tilde{x}) - M(\tilde{x})' + K(\cdot, \tilde{x})\tilde{x}) \, \mathrm{d}t \right\|_{L^p_\rho(\Omega)}.$$

In the numerical computation, we consider two uncertain bond wires. The length of a wire is $l_i = l_{i,0}/(1 - y_i)$ with random variables y_i uniformly distributed in the interval $(0.17, 0.048)$. In the stochastic collocation method, we use a tensor product grid of degree p in the domain of the parameters. The computational effort of the hybrid method is dominated by the number of evaluations of the full order model. Table 6 shows the required number of full model evaluations and the resulting thresholds γ for different degrees p.

6.5 Ageing

The hybrid technique can be extended to simulate ageing as outlined in deliverable D2.6 [6, Sect. 4]. In addition to uncertainties due to manufacturing imperfections, ageing may cause parameter variations. Modeling of ageing is achieved by introducing a random process $\tilde{Y} : \tilde{I} \times \Omega \to \mathbb{R}$, where $\tilde{I} \subset \mathbb{R}$ contains the time-scale of the ageing process. We can then seek for an approximation in separated form

$$\tilde{Y}_{n_y}(\tau, \omega) = \sum_{i=1}^{n_y} f_i(\tau) Y_i(\omega), \tag{54}$$

Table 6: Computational effort in hybrid approach for calculating the failure probability of bond wire fusion for different degrees p of the collocation grid.

degree p	threshold γ	no. full evaluations
1	4.31 $\times 10^{-2}$	768
2	4.60 $\times 10^{-4}$	12
3	1.31 $\times 10^{-6}$	0

e.g., by truncating the Karhunen-Loève expansion. In this way we identify again a set of uncorrelated random variables. If necessary, independence can be achieved by using an additional Hermite polynomial chaos expansion. Now, also the system's response depends on the time τ, i.e., $\tilde{g} : \tilde{I} \times \Gamma \to \mathbb{R}$ and one might define the performance function as

$$g = \min_{\tau \in \tilde{I}} \tilde{g}(\tau, \cdot). \tag{55}$$

Provided that (54) and (55) can be computed efficiently, failure probabilities can be evaluated in the presence of ageing effects using the hybrid method described above.

As an example, consider the threshold voltage of transistors shifted by a negative bias temperature instability [42]. There, the ageing effect is modeled as

$$\Delta V_{\mathrm{th}}(\tau, \omega) = Z_1(\omega) \log\left(Z_2(\omega) + Z_3(\omega)\tau\right), \tag{56}$$

where the Z_i, $i = 1, 2, 3$, denote random variables with statistics inferred from measurement data. If the Z_i from (56) are independent, we can directly identify $Y_i = Z_i$, $i = 1, 2, 3$. If the data is correlated, the Karhunen-Loève expansion (54) can be used instead (note that the log-normal part will ask for some transformation).

6.6 Fast Fault Detection

In the context of failure of technical systems, there is also the field of (fast) fault detection, which was considered in [79, 80, 81, 23].

A special algorithm for fast fault simulation was developed in NXP's in-house circuit simulator Imperfections in manufacturing processes may cause unwanted connections (faults) that are added to the nominal, golden, design of an electronic circuit. When considering faults from the point of view of parameter variations this is well in the range of large deviations. The faulty elements are represented by adding linear conductivities to the circuit. The approach also works for analyzing the effect of additional linear capacitors. However, the main interest is in adding linear conductivities: thus $p\, uv^\top x(t,p)$, where $p = 1/R$, with resistance R, and given vectors u, v, to the system of circuit equations of which the solution becomes $x(t,p)$. By fault simulation we simulate all situations: a huge number of new connections of pairs of vectors (u, v) and each with many different values of p, up to the regime of large deviations, for the newly added element and comparing the result $x(t,p)$ at specific time points with the "golden" solution $\tilde{x}(t) = x(t,0)$ of the fault-free circuit, corresponding with $p = 0$. If the deviation between $x(t,p)$ and $\tilde{x}(t)$ exceeds some threshold, the fault triple (u, v, p), is marked as detectable and is taken out of the list. We also consider opens (broken connections).

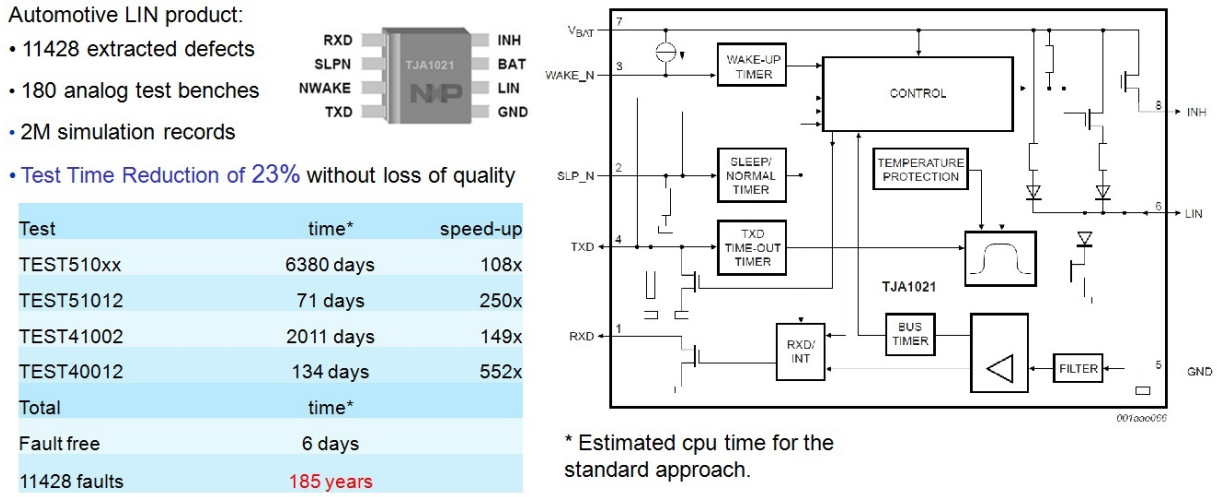

Figure 40: Test time reduction. The faults were detected by the Fast Fault Simulation algorithm. The CPU needed for using the traditional loop order was estimated [81].

A strategy was developed to efficiently simulate the faulty solutions until their moment of detection. The hierarchical structure was enhanced, such that the hierarchical circuit solver could deal with all new elements: note that some new connections may violate the original hierarchical structure of the golden circuit. A clever software solution was developed to cover this case as well. By this, also the faulty problems could benefit from an enhanced form of hierarchical bypassing. Because each candidate fault is a low-rank modification of the designed circuit an hierarchical variant of the Sherman-Morrison formula was exploited. Fast fault simulation is achieved in which the golden solution and all faulty solutions are calculated over the same time step.

The results are stored in a database. This database is of help to first externally diagnose a faulty IC and to identify the candidate circuit submodels where the fault may have happened. After that the IC can be studied further internally. This can help to improve next productions. Moreover, the collection of simulations can also be helpful as a priori check before layouting.

By this implementation, NXP can identify locations on a chip that are probably affected by tiny manufacturing accuracies, which case faulty behaviour at predefined time points for measurements. Inclusion of sensitivity analysis brought speeds up in CPU time of a factor 20 or more. Later invoking of faults gave an additional order of magnitude in speed up. By this reduction of simulation time candidate faults could be detected that would have been impossible otherwise because of excessive CPU time.

With this implementation, NXP's simulator is the best in the world for this functionality on fault detection. Currently, Cadence is implementing the algorithm into their Spectre circuit simulator. Based on our experiences with the implementation in NXP's simulator, the algorithm can relatively easily be re-implemented in any circuit simulator that can be interfaced with the MAGWEL solvers.

6.7 Calibration

In the Progress Report D5.2 [13], a calibration approach was already mentioned to improve yield by electronic control. Design for high yield either means to make a huge number of Monte Carlo samples, or to exploit techniques like Importance Sampling. At NXP the latter was exploited for, e.g., SRAM design [23, 48].

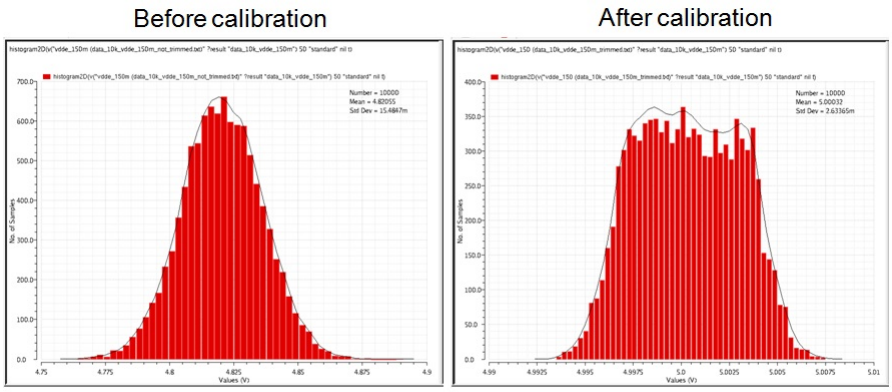

Figure 41: Probability density functions before and after calibration (NXP) [17].

An alternative approach is based on electronic control. Small additional circuitry is optimized and tuned to assure best performance of the main circuit to end-users. To determine the best location of this circuitry, techniques from fast fault simulation can be re-used. The effect of this approach is that the resulting probability density function looks better centered and that the tails look more narrow than without this approach, see Figure 41.

This use of electronic control is called (electronic) 'trimming'. It has no relation to statistical techniques like Winsoring (in which one clips outliers to a boundary percentile), or Trimming (in which one simply neglects outliers). Here it is an electronic tuning, especially on outliers, f.i., by tuning a variable resistor. Assume that a circuit has a DC solution $V(R,p)$, at some measurement point, that depends on a resistor R and an uncertain parameter p. The circuit design aims to satisfy a performance criterion $V_{\rm Low} \leq V \leq V_{\rm Up}$. Now for each p we can determine how V depends on R. An optimal $R(p)$ assures that $V(R(p),p) = V_{\rm Ref} \in [V_{\rm Low}, V_{\rm Up}]$. $R(p)$ can determined by some nonlinear solution technique, involving solving the circuit equations several times. Alternatively,t $R(p)$ can also be found by exploiting the expansion series in generalized polynomial chaos for Uncertainty Quantification using R and p as two parameters, see (57).

$$V(R,p) = e_{ij}^{\top} \sum_{k=1}^{m} a_k \phi_k(R,p), \tag{57}$$

$$\frac{\partial V(R,p)}{\partial R} = e_{ij}^{\top} \sum_{k=1}^{m} a_k \frac{\partial \phi_k(R,p)}{\partial R}. \tag{58}$$

Here $e_{ij}^{\top}$ selects the measurement nodes.

The UQ facilities provide fast evaluations of $V(R,p)$ as well as sensitivities with respect

to R and to p as library functionality in post processing, see (58). This allows that $R(p)$ can be determined quite efficiently for every realization of p. In practice a table can be made from which $R(p)$ can easily be determined or approximated.

In [17] we did fit Generalized Gaussian Density (GGD) distribution

$$f(x) \;=\; \frac{\beta}{2\alpha\,\Gamma(1/\beta)}\exp\left(-\left(\frac{|x-\mu|}{\alpha}\right)^{\beta}\right), \tag{59}$$

to the 'trimmed' data in Figure 41. Here $\alpha, \beta > 0$, $\mu \in \mathbb{R}$ and

$$\Gamma(z) = \int_0^\infty t^{z-1}\mathrm{e}^{-t}\,\mathrm{d}t \qquad \text{for } \; z > 0,$$

is the Gamma function. The mean and the variance of the GGD (59) are given by μ and $\alpha^2\Gamma(3/\beta)/\Gamma(1/\beta)$, respectively. Hence after expressing $\alpha = \sigma\sqrt{\Gamma(1/\beta)/\Gamma(3/\beta)}$ we get that, for all β, the variance is σ^2. We note that for $\beta = 2$ one has $\Gamma(1/2) = \sqrt{\pi}$, $\Gamma(3/2) = 0.5\sqrt{\pi}$ and then $\alpha = \sigma\sqrt{2}$; i.e., the GGD becomes the Gaussian distribution. The parameter β determines the shape. For $\beta = 1$ the GGD corresponds to a Laplacian distribution; for $\beta \to +\infty$ the probability density function in (59) converges to a uniform distribution in $(\mu - \sqrt{3}\sigma, \mu + \sqrt{3}\sigma)$, and when $\beta \downarrow 0$ we get a degenerate distribution in $x = \mu$ (but with a finite variance). For some graphical impression, see Figure 42. Clearly, we are interested in the cases when $\beta \geq 2$.

The initially fitted (non-symmetrical) empirical density function $\hat{f}$ is given in Figure 43 (middle). The fitted Generalized Gaussian Density (GGD) distribution is given in Figure 43 (right). Note that even the tails are very well approximated.

By this a process capability index C_{pkg} similar to the standard Gaussian case could be generalized [17]. This helps communication with the production plants.

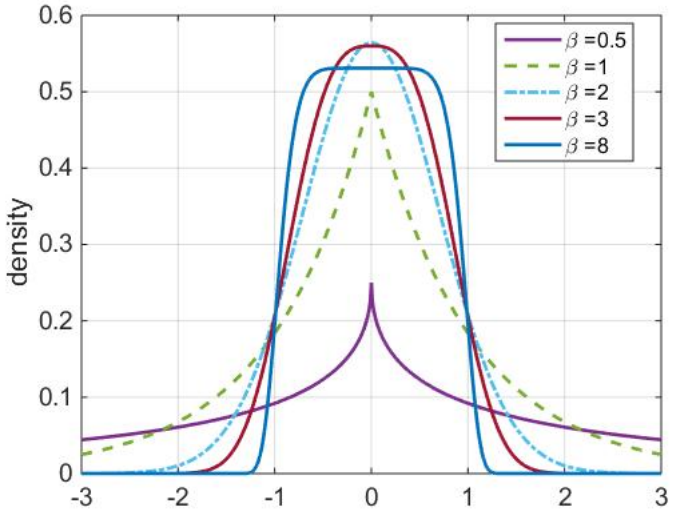

Figure 42: Generalized Gaussian density functions with $\mu = 0$ and $\alpha = 1$ [17].

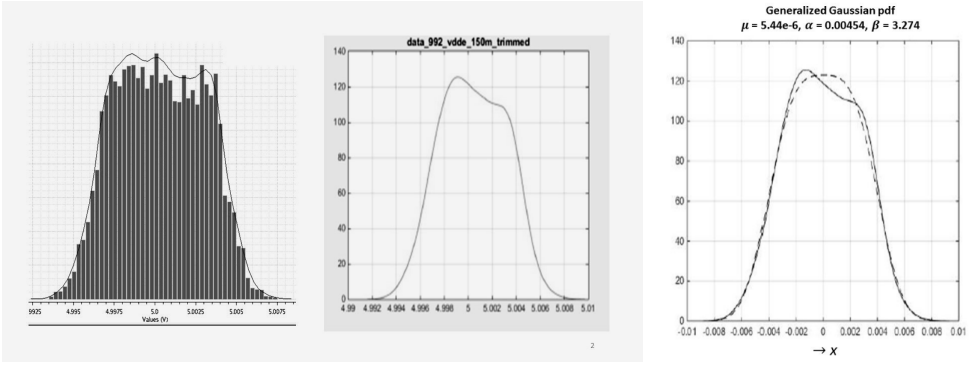

Figure 43: Calibrated data (left) and the associated empirical probability density function $\hat{f}$ (middle) and the fitted Generalized Gaussian Density (GGD) distribution (right) [17].

7 Modeling of uncertainties by probability distributions

A task of the project was the identification of some probability distributions for input parameters, where specific fields of applications from the industrial partners have to be considered. This topic corresponds to Task T2.6.

7.1 Motivation of the task

In nanoelectronics, the miniaturization causes imperfections in the manufacturing of circuits and devices. These variations of an industrial production can often be described sufficiently accurate by a stochastic model, where specific probability distributions are assumed for the physical parameters. This task is dedicated to the identification of appropriate probability distributions of the random variables or random processes, which appear as inputs in the model equations. On the one hand, just a few parameters (like mean and standard deviation, for example) have to be identified under the assumption that an input parameter satisfies a common probability distribution like uniform, beta, normal, etc. On the other hand, irregular probability distributions may underlie the variations, which requires the fitting of a cumulative distribution function or, equivalently, a probability density function.

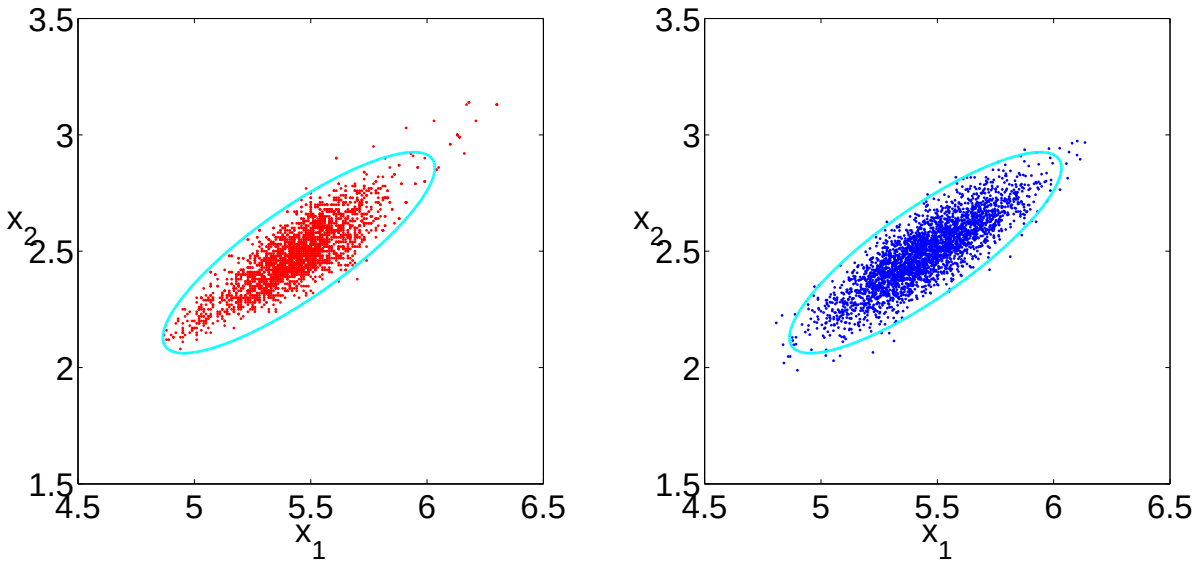

(a) measurements (b) random samples

Figure 44: Measurements in the NXP example (a) and samples from an approximating normal distribution (b). x_1 and x_2 are the currents of an NMOS and of a PMOS, respectively. In both cases, also a 3σ-ellipse is shown (demonstrating the mean and the covariance matrix) [3].

7.2 Statistical analysis of data sets

The industrial partner NXP provided a data set for tests, where the currents of an NMOS as well as a PMOS were measured. This test example was also investigated in [3]. Figure 44 (a) shows the data set consisting of bivariate measurements. The

form of the data suggested an approximation by a two-dimensional normal distribution. The parameters of the normal distribution were fitted to the measurement. Figure 44 (b) depicts (pseudo) random samples from the fitted probability distribution to validate the stochastic modeling. The two sets of samples exhibit a good agreement except for some outliers in the measurement data for high values of the currents. Yet this test data represents output quantities of a device and not input parameters of a model.

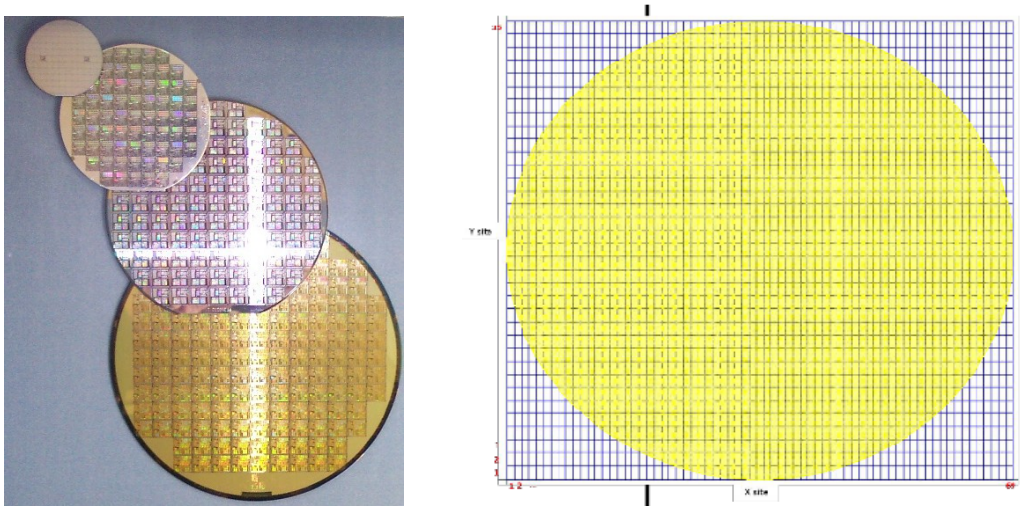

(a) examples of wafers (b) cells for measurements

Figure 45: Examples of wafers (a), from `www.wikipedia.org`, and partition in cells for spatial measurements (b), from ACC [3].

The industrial partners ONN and ACCO made measurements on wafers (semiconductor material) available. Many different material parameters were measured in cells of a two-dimensional grid, where an example is shown in Figure 45 (b). This data represents input parameters for device models. In deliverable D2.3 [3], the properties of the data sets were investigated by statistical tests. It turned out that the measurements do not obey traditional probability laws like normal distributions even for moderate significance levels. The observed variations of the material parameters are tiny. Consequently, the underlying industrial production still achieves a high precision. Moreover, the measurements on wafers exhibit a typical sparse structure in space, because just a few cells from the two-dimensional grid are considered. This sparsity prohibits the resolution of spatial random effects. Thus the provided data sets do not allow for the identification of input probability distributions. Other measurement data was not available from the industrial partners yet. This problem is also mentioned in milestone MS5 [10, Sect. 3].

7.3 Glue-package-die problem

Alternatively, a test problem was designed, which is relevant for the industrial partner ONN.

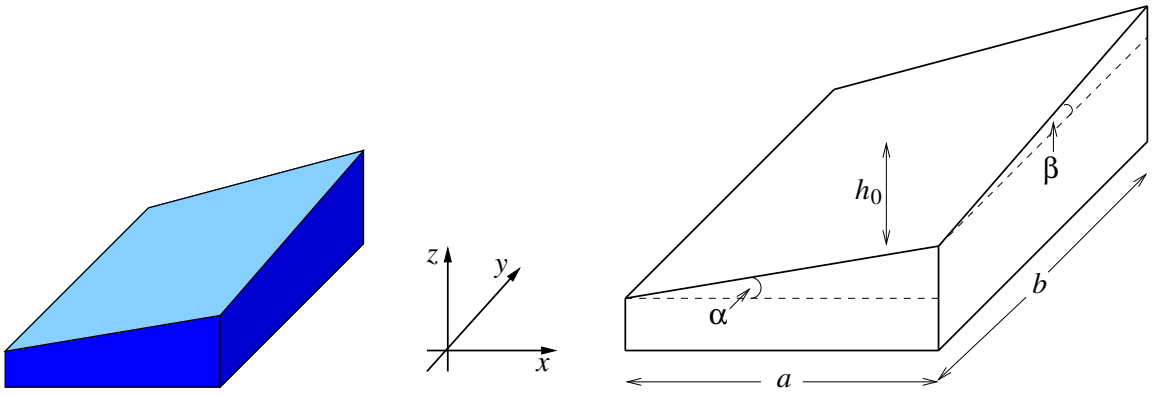

Figure 46: Model of geometry for a piece of glue connecting a die and a package [8, 59].

7.3.1 Description of the problem

Glue is applied to keep a die and a package together. On the one hand, metallic parts of devices can be produced with a high precision. On the other hand, the glue represents a cheap substance, where both the material properties and the resulting position of the connected layers undergo significant variations. The material properties as well as the geometry are important for the quantity of the heat transfer between the layers. The simplified geometry of a piece of glue is illustrated by Figure 46. The bottom layer is given by a rectangle with fixed lengths a, b. The top layer is not parallel due to the variations. Now five random variables are considered as input parameters: thermal conductivity λ and volumetric heat capacity ρc as material parameters, the average height h_0 and the two angles α, β as geometrical parameters.

The output data consists of measurements in L different patches of the piece of glue. The thermal conductance G and the heat capacitance C for each patch reads as

$$G_\ell = \frac{\lambda \; a_\ell \; b_\ell}{h_\ell} \qquad \text{and} \qquad C_\ell = \frac{\rho c \; h_\ell \; a_\ell \; b_\ell}{3} \tag{60}$$

for $\ell = 1, \ldots, L$. Therein, a_ℓ, b_ℓ denote the predetermined lengths of the rectangle for a single patch and h_ℓ is the average height in the patch. It holds that

$$h_\ell = h_0 + \tan\alpha \; x_\ell + \tan\beta \; y_\ell \doteq h_0 + \alpha \; x_\ell + \beta \; y_\ell \tag{61}$$

with known coordinates x_ℓ, y_ℓ for $\ell = 1, \ldots, L$. The relation (61) is inserted into the model functions (60).

In our test problem, we predetermine independent uniform distributions with fixed intervals for each input parameter. The model functions (60) allow for the simulation of measurements by pseudo random numbers, where measurement errors of up to 0.1% are included. We apply $L = 8$ patches. Now the aim is to recover the original probability distributions from the measurements only.

For this purpose, a method of moments was applied, where the moments of the model functions are compared to the moments of the measurement data. This approach requires the knowledge about the type of the input probability distributions. A nonlinear least squares problem yields an approximation of the parameters, which determine the uniform distributions uniquely (two parameters per random variable). However, the

method of moments yields a moderate success, although large numbers of measurements are involved. In particular, the random parameter ρc was inaccessible by this technique, because its influence is less than for the other parameters in the model function.

7.3.2 Fitting of cumulative distribution function

Therefore another approach was implemented, which generates an approximation of the cumulative distribution for the input parameters. An advantage of this strategy is that it does not require a priori knowledge about the type of the underlying probability distributions. Moreover, the approach is able to recover irregular probability distributions, which have to be expected for variations in an industrial manufacturing. For each input parameter $p \in [p_{\min}, p_{\max}]$, a piecewise linear approximation of the cumulative distribution function $F : [p_{\min}, p_{\max}] \to [0, 1]$ is constructed by

$$\tilde{F}(p) := \begin{cases} 0 & \text{for } p < q_1 \\ \frac{j-1}{m-1} \cdot \frac{q_{j+1}-p}{q_{j+1}-q_j} + \frac{j}{m-1} \cdot \frac{p-q_j}{q_{j+1}-q_j} & \text{for } p \in [q_j, q_{j+1}) \text{ and } j \in \{1, \ldots, m-1\} \\ 1 & \text{for } p \geq q_m \end{cases} \quad (62)$$

using discrete points $p_{\min} \leq q_1 < q_2 < \cdots < q_m \leq p_{\max}$ and some integer m. This construction guarantees that the function $\tilde{F}$ is increasing monotone. The grid points $q_1, \ldots, q_m$ represent the unknowns now. Given starting values, an arbitrary number of samples for p can be generated by the approximation (62), where the inverse function $\tilde{F}^{-1}$ is applied to uniformly distributed (pseudo) random numbers in $[0, 1]$. On the one hand, a sample set of the output quantities (60) is computed by the samples of the input parameters. On the other hand, the measurement data is available for (60). The ranges of G_ℓ and C_ℓ are partitioned into a finite number of intervals. Comparing the ratio of samples and the ratio of measurements for each interval, a nonlinear least squares problem occurs for the unknown grid points. Figure 47 illustrates the resulting approximations for the five input parameters in the case of $m = 20$. A comparison to the exact cumulative distribution functions shows a relatively good agreement, since other numerical techniques like the method of moments yield worse approximations.

At a later stage, the package-die-glue problem shall be simulated in a more realistic and relevant form. Firstly, the artificially computed measurements have to be replaced by real measured data. Secondly, the simple model functions (60) are substituted by parabolic partial differential equations describing the heat transfer.

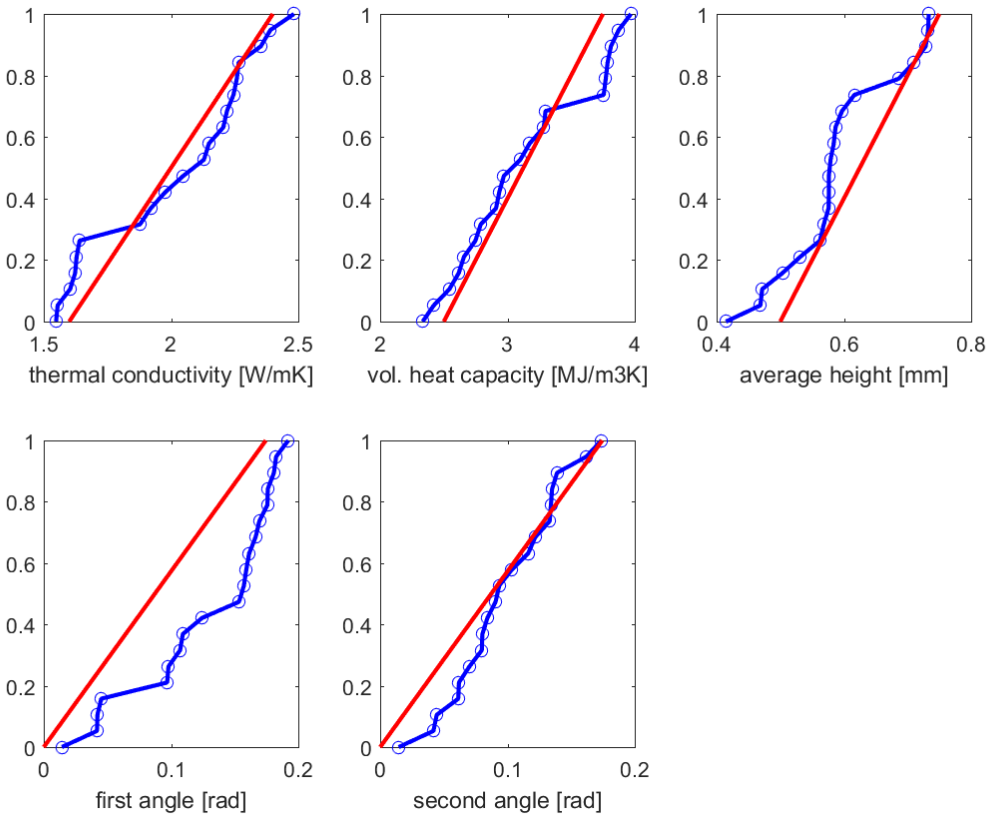

Figure 47: Cumulative distribution functions for five random variables: exact input distributions (red) and piecewise linear approximation (blue) [59].

8 Implementation

The implementation of algorithms for the tasks of WP2: Uncertainty Quantification is specified in the report of deliverable D2.7 [7]. Figure 48 illustrates the software packages included in our uncertainty quantification.

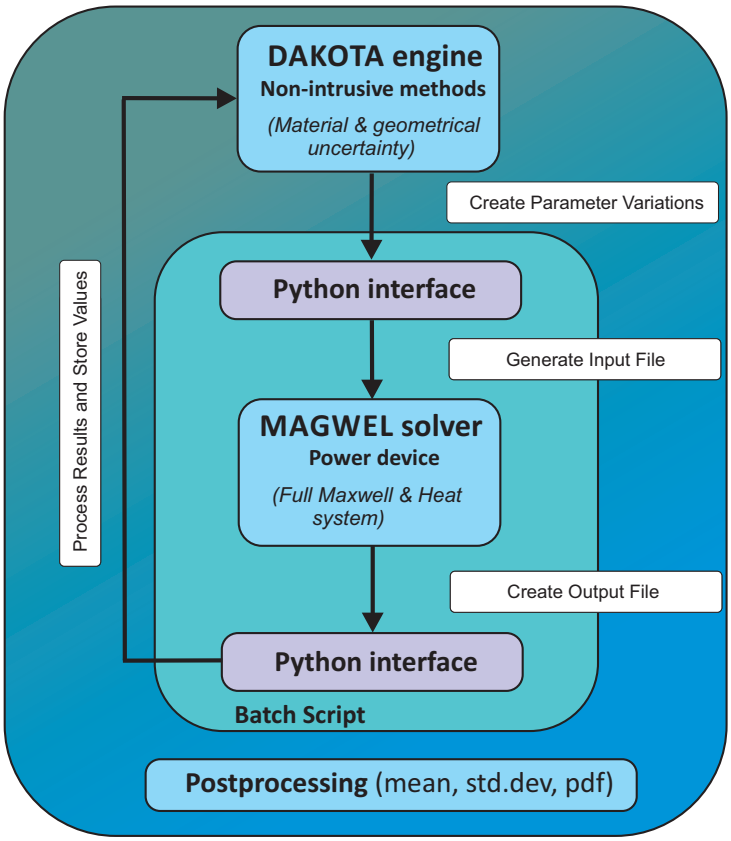

Figure 48: Software packages for implementations in Uncertainty Quantification [4, 7, 62].

As stated in deliverable D2.7 [7], one may distinguish between three different levels of implementation. Level one considers the UQ method that led to implementation of third-party software. The software development inside the nanoCOPS project aims at realizing bridges between the third party software and the in-house developed software libraries. The second level of implementation concerns the development of various software libraries at different partner's locations and the integration level of the various in house package is brought to stage that the full system is operational. 'Operational' means that the tools can be used and the data communication is in place but some manual intervention of the user is required to arrive at final results. Finally, the third level of implementation consists of a fully integrated system of libraries and the data communication is shielded away from the user. This is the highest level of implementation since it corresponds to the most user-friendly way of working with the software. It should be noted that arriving at this stage is also very labor intensive from the software development point of view and return-of-investment (ROI) of the resources is expected before it is decided to enter into a level three implementation. Whereas in deliverable D2.7 [7] we listed the various implementation levels, we will provide the reader here with some impression what it means if the third level of integration is lacking, e.g. how

much effort is required to get the desired simulation flow operational?

As a typical example we consider the UQ simulation of the power transistor model that has served as a key application of the tool developments in the nanoCOPS projects. The user needs to fight his/her way through the following recipe [61].

1. create a source folder
   in this example it is named ”src”
2. outside this folder model file for ptm-et
   In this example it is the ptmet input structure file named here ”structure.xml”
3. Also provide the table model
   here it is described in the file ”tableModelBPTM130_NMOS.csv”
4. The file ”dakota_field_mag_uq_pce__2in_20out_3mix.in” is the main script of dakota (UQ). We must make sure that paths are set properly.
   In the file ”dakota_magTimeFunctionMultiOutput.py” it is line 72.

The file ”dakota_magTimeFunctionMultiOutput.py” contains the following text [61]:

```
#!/usr/bin/python

import string
import numpy as npy
import scipy as spy
import csv
import sys
import os
import time
import re
import string
import subprocess

import fileinput
import time

import os.path
import time


def dakota_runAB():

     fileIn="../../structure.xml"
     inpfile="input.dat"
     #solverPath ="/my_path/bin/solvEM"
     indata=npy.loadtxt(inpfile)
     #print indata


     for cur in range(1):
          direct = str(cur)
```

```
          os.system("rm -rf " + direct)
          os.mkdir(direct)
          os.system("cp ../tableModelBPTM130_NMOS.csv " + direct)
          os.system("cp input.dat " + direct)
          os.chdir(direct)

          os.system("rm -rf structure.xml")

          k = 4

          basis = 900.81+1.0+0.5+1.0+1.0
          suma=0
          for nparam in range(1,len(indata)):
 # print indata[nparam]
  suma =suma + round(float(repr(indata[nparam])), k)

          suma = basis + suma


          fileIn="../../structure.xml"
          o = open("structure.xml","a") #open for append


          for line in open(fileIn):
  line = line.replace("placeholder1",str((indata[0])))
  line = line.replace("placeholder2",str((indata[1])))
  line = line.replace("placeholderB",str((suma)))
  o.write(line + "\n")

          o.close()

          popen = subprocess.Popen(['/my_path/bin/solvEM',"--mode=ettransient"])
          popen.wait()
          print "I am waiting a bit:"
          time.sleep(1)
          os.chdir("..")

def dakota_field_Myparser(**kwargs):

inpfile="input.dat"
indata=npy.loadtxt(inpfile)

file_cvs = 'results_transient.csv'
ll=0


for conductivity in range(1):
direct=str(conductivity)
#print direct
os.chdir(direct)
os.system("ls -lt")

while not os.path.exists(file_cvs):
#print "i am sleeping and waiting"
time.sleep(1)
os.system("ls -lt")
```

```
if ll==0:
tt = "cp " + 'results_transient.csv' + ' ../'
os.system(tt)
tt = "cp " + 'times_simulated.txt' + ' ../'
os.system(tt)


with open(file_cvs, 'rb') as csvfile:
spamreader = csv.reader(csvfile, delimiter=',', quotechar='|')

columns = len(next(spamreader))

if columns!=0:
ut =[]
temp =[]
for it in xrange(columns-1):
ut.append([])

for row in spamreader:
for col in range(0,columns-1):
ut[col].append(float(row[col]))
else:
columns=kwargs['cl']+1  #21
rows=kwargs['ro'] #2
for row in rows:
for col in range(0,columns-1):
ut[col].append(float(0.0))

for col in range(1,columns-1):
temp.append(ut[col])

temp=npy.array(npy.transpose([temp]))
name_file_dat = 'solution_'+str(ll)+'.dat'

ll=ll+1
npy.savetxt(name_file_dat, temp, fmt="%.18e", delimiter=" ", newline="\n")
tt = "cp " + name_file_dat + ' ../'
os.system(tt)
os.chdir("..")
```

The content of the file "dakota_field_mag_uq_pce__2in_20out_3mix.in" is

```
#  DAKOTA command: dakota -i dakota_field_mag_uq_pce__2in_20out_3mix.in
#  -o dakota_field_mag_uq_pce_2in_20out_3mix.out
#   > dakota_field_mag_uq_pce_2in_20out_3mix.stdout

environment
  #graphics
  tabular_data
    tabular_data_file = 'dakota_field_mag_uq_pce_tabular_dataMIX.dat'
  results_output
    results_output_file = 'dakota_field_mag_uq_pce_resultMIX.dat'

method
```

```
  polynomial_chaos
export_expansion_file ='dakota_field_mag_uq_pce_expansion_uq_pceMIX.dat'
    cubature_integrand = 3
    variance_based_decomp #interaction_order = 1

variables
    uniform_uncertain = 2
    lower_bounds      =  18000000 0.95
    upper_bounds      =  22000000 1.05
    descriptors       = 'h1' 'h2'

interface
  analysis_drivers = 'mag_field_bb_pp_20_mix.py'
    fork
    parameters_file = 'params.in'
    results_file    = 'results.out'
    file_tag
    file_save
# aprepro

responses
  response_functions = 20
  response_descriptors = 'Vd' 'Id' 'Td' 'TFd' 'Vs' 'Is' 'Ts' 'TFs' 'Vp' 'Ip'
                         'Tp' 'TFp' 'Vb' 'Ib' 'Tb' 'TFb' 'Vg' 'Ig' 'Tg' 'TFg'
field_responses = 20
lengths = 11 11 11 11 11 11 11 11 11 11 11 11 11 11 11 11 11 11 11 11
num_coordinates_per_field = 11
coordinate_list = 0.0 2e-04 4e-04 6e-04 8e-04 1.0e-03 1.2e-03 1.4e-03
                  1.6e-03 1.8e-03 2.0e-03
  no_gradients
  no_hessians
```

Thus with these prepared files, all that the users needs to do is to identify the proper locations of the file and program names it the python script, prepare the usual input-files for the simulator by the appropriate placeholders and run the DAKOTA executable. However with the UQ-GUI above text-based procedure is replaced by a drop-down selection menu.

9 Summary

This deliverable presents the research results on ”Uncertainty Quantification” (UQ) itemized for the seven tasks of Work Package 2. More details can be found in the previous deliverables as well as the project's publications given in the following bibliography. The aims of the work programme have been achieved. New fields of applications were made accessible by our modeling and simulations in nanoelectronics. On the one hand, we developed new numerical methods for problems with parameter variations. On the other hand, approaches, which are already known from recent academic works, were adjusted to solve UQ problems in nanoelectronics. We applied all techniques to simulate mathematical models of devices or circuits. Often multiphysics problems, which include different physical aspects, were considered, because the miniaturization of components does not allow for neglecting secondary effects any more. The feasibility of the numerical methods was verified in each task. In addition, we investigated the efficiency by simulations of test examples. Most of the test examples either originated from our industrial partners or were designed in cooperation with these companies. Some numerical methods demonstrate a significant improvement in comparison to former techniques.

References

[1] H. De Gersem, S. Schöps, U. Römer: *Intermediate Report on Models and algorithms for quantification of uncertainties in materials, geometry and boundaries of devices.* Deliverable D2.1 in nanoCOPS project, June 30, 2014.

[2] J. Schneider, U. Baur, P. Benner, L. Feng, M. Hess, R. Pulch, P. Putek, M. Günther, J. ter Maten: *Intermediate Report on Parametrized MOR techniques for subproblems and associated error bounds.* Deliverable D2.2 in nanoCOPS project, June 30, 2014.

[3] R. Pulch, P. Putek, J. ter Maten, R. Janssen, M. Stoutjesdijk, F. Deleu, A. Wieers, P. Barroul, P. Reynier: *Intermediate Report on probability distributions fitted to real data of circuits and devices.* Deliverable D2.3 in nanoCOPS project, July 11, 2014.

[4] P. Putek, R. Pulch, S. Schöps, J. ter Maten, M. Günther, H. De Gersem, P. Meuris, W. Schoenmaker: *Intermediate Report on methods and algorithms for co-simulation of coupled problems including random parameters without Polynomial Chaos or reduced-order models.* Deliverable D2.4 in nanoCOPS project (2nd version), February 19, 2015.

[5] R. Pulch, P. Putek, S. Schöps, Y. Yue, J. ter Maten: *Algorithms using Polynomial Chaos and reduced-order models in co-simulation of coupled problems with random parameters.* Deliverable D2.5 in nanoCOPS project (2nd version), April 19, 2016.

[6] U. Römer, T. Casper, R. Pulch, E.J.W. ter Maten: *Algorithm for computation of failure probabilities and ageing effects.* Deliverable D2.6 in nanoCOPS project (2nd version), April 14, 2016.

[7] W. Schoenmaker, P. Meuris, B. De Smedt, S. Schöps, U. Römer, H. De Gersem, J. Schneider, U. Baur, P. Benner, L. Feng, M. Hess, R. Pulch, P. Putek, M. Günther, J. ter Maten: *Algorithms implemented in software packages for all Tasks 2.1-2.6.* Deliverable D2.7 in nanoCOPS project, July, 2016.

[8] R. Pulch, J. ter Maten, H. De Gersem, W. Schoenmaker: *Decision on models and algorithms for uncertainties in materials, geometry and boundary conditions of devices. Verification by Report M2.1.* Milestone MS3 in nanoCOPS project, July 11, 2014.

[9] R. Pulch, J. ter Maten: *Selection on formulation of coupled problems with random parameters for Tasks T2.3, T2.4 and T2.5. Selection on methods from all Tasks T2.1-T2.6 to be implemented in software packages suitable for industry.* Milestone MS4 in nanoCOPS project, November 29, 2014.

[10] R. Pulch, J. ter Maten, R. Janssen, T. Kratochvíl, D. Duque, F. Deleu, R. Gillon, A. Wieers: *Validation of probability density functions fitted to real data of circuits and devices by Tasks T2.6 and T3.3. Selection of probability distributions for final numerical simulations. Verification by D2.3 and Report M2.3.* Milestone MS5 in nanoCOPS project, April 21, 2015.

[11] P. Benner, L. Feng, P. Meuris, W. Schoenmaker, S. Schöps, J. ter Maten: *Intermediate report on pMOR for linear and nonlinear coupled problems*. Deliverable D1.1 in nanoCOPS project, July 30 2014.

[12] W. Schoenmaker, S. Schöps, L. Feng, K. Bittner, J. ter Maten: *Software design report for the electro-thermal co-simulation tool*. Deliverable D1.2 in nanoCOPS project, July 30, 2014.

[13] E.J.W. ter Maten, M. Günther: *Periodic Progress Report Year 2 (MTR). Period covered: From 01/08/2014 (M10) to 31/03/2015 (M17)*. Deliverable 5.2 in nanoCOPS project (6th version), April 8, 2015.

[14] P. Alotto, F. Freschi, M. Repetto: *Multiphysics problems via the cell method: the role of Tonti diagrams.* IEEE Trans. Magn. 46:8 (2010), 2959-2962.

[15] A. Bartel, M. Brunk, M. Günther, S. Schöps: *Dynamic iteration for coupled problems of electric circuits and distributed devices.* SIAM J. Sci. Comput. 35:2 (2013), B315–B335.

[16] A. Bartel, M. Günther, M. Schulz: *Modeling and discretization of a thermal-electric test circuit.* In: K. Antreich (eds.): Modeling, Simulation and Optimization of Integrated Circuits. ISNM Vol. 146, Birkhäuser, 2003, pp. 187–201.

[17] T.G.J. Beelen, J.J. Dohmen, E.J.W. ter Maten, B.Tasić: *Fitting Generalized Gaussian Distributions for Process Capability Index*. Submitted to Proceedings SCEE-2016, Scientific Computing in Electrical Engineering, St. Wolfgang/Strobl, Austria, 2016.

[18] P. Benner , S. Gugercin, K. Willcox: *A survey of projection-based model reduction methods for parametric dynamical systems*. SIAM Review 57:4 (2015), 483-531.

[19] P. Benner, M.W. Hess: *Reduced basis modeling for uncertainty quantification of electromagnetic problems in stochastically varying domains.* In: A. Bartel, M. Clemens, M. Günther, E.J.W. ter Maten (eds.): Scientific Computing in Electrical Engineering SCEE 2014. Mathematics in Industry Vol. 23, Springer, Berlin 2016, pp. 215–222.

[20] P. Benner, M.W. Hess, J. Schneider: *Reduced basis methods for time-harmonic Maxwell's equations with stochastic coefficients.* ACOMEN 2014, 6th International Conference on Advanced Computational Methods in Engineering, June 24, 2014, Ghent, Belgium.

[21] P. Benner, J. Schneider: *Uncertainty quantification for Maxwell's equations using stochastic collocation and model order reduction.* Int. J. Uncertain. Quantif. 5:3 (2015), 195–208.

[22] Z. Bontinck, O. Lass, S. Schöps: *Robust optimization of a stochastic reduced order model of a permanent magnet synchronous machine.* In: ISEF 2015, XVII International Symposium on Electromagnetic Fields in Mechatronics, Electrical and Electronic Engineering, 2015.

[23] A. Di Buccianico, J. ter Maten, R. Pulch, R. Janssen, J. Niehof, M. Hanssen, S. Kapora: *Robust and efficient uncertainty quantification and validation of RFIC isolation* Radioengineering 23:1 (2014), 308–318.

[24] R.E. Caflisch: *Monte Carlo and Quasi-Monte Carlo Methods.* Acta Numerica 7 (1998), 1–49.

[25] T. Casper, H. De Gersem, R. Gillon, T. Gotthans, T. Kratochvíl, P. Meuris, S. Schöps: *Electrothermal simulation of bonding wire degradation under uncertain geometries.* Proceedings of the 2016 Design, Automation and Test in Europe Conference & Exhibition (DATE), Dresden, Germany, 2016, pp. 1297-1302.

[26] T. Casper, U. Römer, S. Schöps: *Efficient evaluation of bond wire fusing probabilities*. Presentation at SIAM Conference on Uncertainty Quantification, April 5-8, 2016, Lausanne, Switzerland.

[27] M. Clemens: *Large Systems of Equations in a Discrete Electromagnetism: Formulations and Numerical Algorithms.* IEE Proceedings - Science, Measurement and Technology, 152(2), March 2005.

[28] M. Clemens, E. Gjonaj, P. Pinder, T. Weiland: *Self-consistent simulations of transient heating effects in electrical devices using the finite integration technique*. IEEE Trans. Magn. 37:5 (2001), 3375–3379.

[29] J. Corno, C. de Falco, H. de Gersem, S. Schöps: *Isogeometric analysis simulation of TESLA cavities under uncertainty.* IEEE Proceedings of the International Conference on Electromagnetics in Advanced Applications (ICEAA), 2015, pp. 1508–1511.

[30] M.C. Delfour, J.-P. Zolésio: *Shapes and geometries: metrics, analysis, differential calculus, and optimization.* (2nd ed.) SIAM, 2011.

[31] D.J. Duque, S. Schöps, A. Wieers: *Fast and reliable simulations of the heating of bond wires.* In: G. Russo, V. Capasso, G. Nicosia, V. Romano (eds.): Progress in Industrial Mathematics at ECMI 2014. Mathematics in Industry, Vol. 22, Springer, 2016.

[32] L. Feng., A.C. Antoulas, P. Benner.: *Some a posteriori error bounds for reduced order modelling of (non-)parametrized linear systems*. Max Planck Institute Magdeburg Preprint MPIMD/15-17, MPI-Magdeburg (October 2015).

[33] L. Feng, Y. Yue, N. Banagaaya, P. Meuris, W. Schoenmaker, P. Benner: *Parametric modeling and model order reduction for (electro-)thermal analysis of nanoelectronic structures.* to appear in: J. Math. Ind.

[34] K. Gausling, A. Bartel: *First results for uncertainty quantification in co-simulation for coupled electrical circuits.* In: A. Bartel, M. Clemens, M. Günther, E.J.W. ter Maten (eds.): Scientific Computing in Electrical Engineering SCEE 2014. Mathematics in Industry Vol. 23, Springer, Berlin 2016, pp. 243–251.

[35] R.G. Ghanem, P.D. Spanos: *Stochastic finite elements: a spectral approach.* Springer, 1991.

[36] A. Grama, A. Gupta, G. Karypis, V. Kumar: *Introduction to Parallel Computing.* Addison-Wesley, 2003.

[37] M. Günther, U. Feldmann, J. ter Maten: *Modelling and discretization of circuit problems.* In: W.H.A. Schilders, E.J.W. ter Maten (eds.): Handbook of Numerical Analysis, Vol. 13, Elsevier, 2015, pp. 523–659.

[38] J.M. Hammersley, D.C. Handscomb: *Monte Carlo Methods.* Methuen, 1964.

[39] R. Hiptmair, J. Li: *Shape derivatives in differential forms i: An intrinsic perspective.* Annali di Matematica Pura ed Applicata 192:6 (2013), 1077–1098.

[40] H.H.J.M. Janssen, P. Benner, K. Bittner, H.G. Brachtendorf, L. Feng, E.J.W. ter Maten, R. Pulch, W. Schoenmaker, S. Schöps, C. Tischendorf: *The European project nanoCOPS for nanoelectronic coupled problems solutions.* In: G. Russo, P. Meuris, M. Günther (eds.): Progress in Industrial Mathematics at ECMI 2014. Mathematics in Industry Vol. 22, Springer, Berlin, 2016.

[41] R. Janssen, J. ter Maten, C. Tischendorf, H.G. Brachtendorf, K. Bittner, W. Schoenmaker, P. Benner, L. Feng, R. Pulch, F. Deleu, A. Wieers: *The nanoCOPS project on algorithms for nanoelectronic coupled problems solutions.* In B. Schreffler, E. Onate, M. Papadrakakis (Eds.): Coupled Problems in Science and Engineering VI – COUPLED PROBLEMS 2015. Proceedings of the VI International Conference on Coupled Problems in Science and Engineering, May 18-20, 2015, San Servolo Island, Venice, Italy. Publ.: CIMNE - International Center for Numerical Methods in Engineering, Barcelona, Spain, 2015, pp. 1029–1036.

[42] V.B. Kleeberger, M. Barke, C. Werner, D. Schmitt-Landsiedel, U. Schlichtmann: *A compact model for NBTI degradation and recovery under use-profile variations and its application to aging analysis of digital integrated circuits.* Microelectronics Reliability 54:6 (2014), 1083-1089.

[43] J. Li, D. Xiu: *Evaluation of failure probability via surrogate models.* J. Comput. Phys. 229:23 (2010), 8966–8980.

[44] J. Li, J. Li, D. Xiu: *An efficient surrogate-based method for computing rare failure probability.* J. Comput. Phys. 230:24 (2011), 8683–8697.

[45] MAGWEL NV: *An electro-thermal module of a power transistor modeler: PTM-ET*. `http://www.magwel.com/`, 2014.

[46] E.J.W. ter Maten, P.A. Putek, M. Günther, R. Pulch, C. Tischendorf, C. Strohm, W. Schoenmaker, P. Meuris, B. De Smedt, P. Benner, L. Feng, N. Banagaaya, Y. Yue, R. Janssen, J.J. Dohmen, B. Tasić, F. Deleu, R. Gillon, A. Wieers, H.-G. Brachtendorf, K. Bittner, T. Kratochvíl, J. Petřzela, R. Sotner, T. Götthans, J. Dřinovský, S. Schöps, D.J. Duque Guerra, T. Casper, H. De Gersem, U. Römer, P. Reynier, P. Barroul, D. Masliah, B. Rousseau: *Nanoelectronic Coupled problems solutions - nanoCOPS: modelling, multirate, model order reduction, uncertainty quantification, fast fault simulation.* J. Math. Ind. 7:2 (2016). `http://www.mathematicsinindustry.com/content/7/1/2`.

[47] E.J.W. ter Maten, M. Günther, P. Putek, P. Benner, L. Feng, J. Schneider, H.G. Brachtendorf, K. Bittner, F. Deleu, A. Wieers, R. Janssen, T. Kratochvíl, T. Götthans, R. Pulch, Q. Liu, P. Reynier, W. Schoenmaker, P. Meuris, S. Schöps, H. De Gersem, C. Tischendorf, C. Strohm: *nanoCOPS: Nanoelectronic COupled Problem Solutions.* ECMI Newsletter 56, 2014, pp. 62–67.

[48] E.J.W. ter Maten, O. Wittich, A. Di Bucchianico, T.S. Doorn, T.G.J. Beelen: *Importance sampling for determining SRAM yield and optimization with statistical constraint*. In: B. Michielsen, J.-R. Poirier (eds.): Scientific Computing in Electrical Engineering SCEE 2010. Mathematics in Industry Vol. 16, Springer, 2012, pp. 39–48.

[49] D. Meeker: *FEMM – Finite Element Method Magnetics.* User's Manual version 4.2, 2010.

[50] W.J. Morokoff, R.E. Caflisch: *Quasi-Monte Carlo integration.* J. Comput. Phys. 122 (1995), 218–230.

[51] K. Mouthaan: *Modelling of RF High Power Bipolar Transistors*. PhD thesis, TU Delft, Delft, The Netherlands, 2001.

[52] G.T. Nöbauer, H. Moser: *Analytical approach to temperature evaluation in bonding wires and calculation of allowable current.* IEEE Trans. Adv. Packag. 23:3 (2000), 426–435.

[53] R. Pulch: *Stochastic collocation and stochastic Galerkin methods for linear differential algebraic equations.* J. Comput. Appl. Math. 262 (2014), 281–291.

[54] R. Pulch: *Model order reduction for stochastic expansions of electric circuits.* In: A. Bartel, M. Clemens, M. Günther, E.J.W. ter Maten (eds.): Scientific Computing in Electrical Engineering SCEE 2014. Mathematics in Industry Vol. 23, Springer, Berlin 2016, pp. 223–232.

[55] R. Pulch, A. Bartel, S. Schöps: *Quadrature methods with adjusted grids for stochastic models of coupled problems.* In: G. Russo, V. Capasso, G. Nicosia, V. Romano (eds.): Progress in Industrial Mathematics at ECMI 2014. Mathematics in Industry, Vol. 22, Springer, 2016.

[56] R. Pulch, E.J.W. ter Maten: *Stochastic Galerkin methods and model order reduction for linear dynamical systems.* Int. J. Uncertain. Quantif. 5:3 (2015), 255–273.

[57] R. Pulch, E.J.W. ter Maten, F. Augustin: *Sensitivity analysis of linear dynamical systems in uncertainty quantification.* Proc. Appl. Math. Mech. 13 (2013), 507–508.

[58] R. Pulch, E.J.W. ter Maten, F. Augustin: *Sensitivity analysis and model order reduction for random linear dynamical systems.* Math. Comput. Simulat. 111 (2015), 80–95.

[59] R. Pulch, P. Putek, H. De Gersem, A. Wieers: *Identification of probabilistic input data for modeling uncertainties*. Presented at ECMI-2016 The 19th European Conference on Mathematics for Industry, 13-17th June 2016, Santiago de Compostela, Spain.

[60] P. Putek, K. Gausling, A. Bartel, K.M. Gawrylczyk, J. ter Maten, R. Pulch, M. Günther: *Robust topology optimization of a permanent magnet synchronous machine using multi-level set and stochastic collocation methods.* In: A. Bartel, M. Clemens, M. Günther, E.J.W. ter Maten (eds.): Scientific Computing in Electrical Engineering SCEE 2014. Mathematics in Industry Vol. 23, Springer, Berlin 2016, pp. 233–242.

[61] P. Putek, P. Meuris, J. ter Maten, R. Pulch, A. Wieers, W. Schoenmaker, M. Günther: *Uncertainty quantification in electro-thermal coupled problems based on a power transistor device.* IFAC-PapersOnLine 48:1 (2015), 938–939.

[62] P. Putek, P. Meuris, R. Pulch, E.J.W. ter Maten, M. Günther, W. Schoenmaker, F. Deleu, A. Wieers: *Shape optimization of a power MOS device under uncertainties.* Proceedings of the 2016 Design, Automation and Test in Europe Conference & Exhibition (DATE), Dresden, Germany, 2016, pp. 319-324.

[63] P. Putek, P. Meuris, R. Pulch, J. ter Maten, W. Schoenmaker, M. Günther: *Uncertainty quantification for a robust topology optimization of power transistor devices.* IEEE Trans. Magn. 52:3 (2016).

[64] R. Ramarotafika, A. Benabou, S. Clénet: *Stochastic modeling of soft magnetic properties of electrical steels, application to stators of electrical machines*. IEEE Trans. Magn. 48 (2012), 2573–2584.

[65] U. Römer, S. Schöps: *Adjoint error estimation for a pseudo-spectral approach to stochastic field-circuit coupled problems.* Proc. Appl. Math. Mech. 15 (2015), 711–714.

[66] U. Römer, S. Schöps, T. Weiland: *Approximation of moments for the nonlinear magnetoquasistatic problem with material uncertainties*. IEEE Trans. Magn. 50:2, 2014.

[67] U. Römer, S. Schöps, T. Weiland: *Stochastic modeling and regularity of the nonlinear elliptic curl-curl equation*. to appear in: SIAM/ASA J. Uncertainty Quantification.

[68] W. Schoenmaker, O. Dupuis, B. De Smedt, P. Meuris, J. Ocenasek, W. Verhaegen, D. Dumlugöl, M. Pfost: *Fully-coupled 3D electro-thermal field simulator for chip-level analysis of power devices.* In: 19th International Workshop on Thermal Investigations of ICs and Systems (THERMINIC), IEEE, Berlin, Germany, 2013, pp. 210–215.

[69] W. Schoenmaker, P. Meuris, C. Strohm, C. Tischendorf: *Holistic coupled field and circuit simulation.* Proceedings of the 2016 Design, Automation and Test in Europe Conference & Exhibition (DATE), Dresden, Germany, 2016, pp. 307-312.

[70] C. Schuster, G. Leonhardt, W. Fichtner: *Electromagnetic simulation of bonding wires and comparison with wide band measurements.* IEEE Trans. Adv. Packag. 23:1 (2000), 69–79.

[71] S. Schöps, H. De Gersem, A. Bartel: *A cosimulation framework for multirate time integration of field/circuit coupled problems.* IEEE Trans. Magn. 46 (2010), 3233–3236.

[72] C. Schwab, R.A. Todor: *Sparse finite elements for stochastic elliptic problems – higher order moments*. Computing 71:1 (2003), 43–63.

[73] Ch. Schwab, R.A. Todor: *Karhunen-Loève approximation of random fields by generalized fast multipole methods.* J. Comput. Phys. 217 (2006), 100–122.

[74] S. Selberherr: *Analysis and Simulation of Semiconductor Devices*. Springer, 1984.

[75] S.A. Smolyak: *Quadrature and interpolation formula for tensor products of certain classes of functions.* Soviet. Math. Dokl. 4 (1963), 240–243.

[76] A.H. Stroud: *Remarks on the disposition of points in numerical integration formulas.* Mathematical Tables and Other Aids to Computation 11:60 (1957), 257-261.

[77] B. Sudret: *Global sensitivity analysis using polynomial chaos expansion.* Rel. Eng. Syst. Safety 93:7 (2008), 964–979.

[78] S.M. Sze: *Physics of Semiconductor Devices.* John Wiley & Sons, 1981.

[79] B. Tasić, J.J. Dohmen, E.J.W. ter Maten, T.G.J. Beelen, W.H.A. Schilders, A. de Vries, M. van Beurden: *Robust DC and efficient time-domain fast fault simulation.* COMPEL 33:4 (2014), 1161–1174.

[80] B. Tasić, J.J. Dohmen, E.J.W. ter Maten, T.G.J. Beelen, H.H.J.M. Janssen, W.H.A. Schilders, M. Günther: *Fast fault simulation to identify subcircuits involving faulty components.* In: G. Russo, P. Meuris, M. Günther (eds.): Progress in Industrial Mathematics at ECMI 2014. Mathematics in Industry Vol. 22, Springer, Berlin, 2016.

[81] B. Tasić, J.J. Dohmen, R. Janssen, E.J.W. ter Maten, R. Pulch, T.G.J. Beelen: *Fast time-domain simulation for reliable fault detection.* Proceedings of the 2016 Design, Automation and Test in Europe Conference & Exhibition (DATE), Dresden, Germany, 2016, pp. 301-306.

[82] T. Weiland: *A discretization model for the solution of Maxwell's equations for six-component fields.* International Journal of Electronics and Communications 31 (1977), 116–120.

[83] T. Weiland: *Time domain electromagnetic field computation with finite difference methods.* International Journal of Numerical Modelling: Electronic Networks, Devices and Fields 9:4 (1996), 295–319.

[84] D. Xiu: *Numerical Methods for Stochastic Computations: a Spectral Method Approach.* Princeton University Press, 2010.

[85] Y. Yue, L. Feng, P. Meuris, W. Schoenmaker, P. Benner: *Application of Krylov-type parametric model order reduction in efficient uncertainty quantification of electro-thermal circuit.* Proceedings of the Progress in Electromagnetics Research Symposium (PIERS), July 06-09, Prague, Czech Republic, 2015, pp. 379–384.